



## SCMS SCHOOL OF ENGINEERING & TECHNOLOGY

### PUBLICATION DETAILS 2018

SI No:	Name	First Author	Second Author	Third Author	Fourth Author	INDEXING
1	Jane Theresa	PBSH1801				UGC CARE
2	SREEJA K.A	PEC1801				SCOPUS
3	Vinoj P G	PEC1802				SCI
4	Dr.Sunil Jacob		PEC1802			
5	Dr. Sheeja Janardhanan	PME1801		PME1804		SCI
6	Sajith E.			PME1802		SCI
7	Ajith Kumar R		PME1803			SCOPUS
8	Aswini J		PCE1801			SCOPUS
9	Dr.Vinod P		PCSE1801	PCSE1802		SCOPUS
10	Dr.Varun Menon			PEC1802		SCI

**Total Publication for the calender year 2018**

**9**



  
DR. PRAVEENSAL C.I.  
PRINCIPAL  
SCMS SCHOOL OF ENGINEERING & TECHNOLOGY



## IN SEARCH OF A SELF IN THE NOVELS *THE BLUEST EYE* BY TONI MORRISON AND *THE GOD OF SMALL THINGS* BY ARUNDHATI ROY

**JANE THERESA**

Assistant Professor,  
English,

SSET, SCMS Ernakulam.

(KERALA) INDIA

### ABSTRACT

*There is a quoting in the Holy bible by St Mark, stating that the stones which the builders rejected became the cornerstone of the building, that was the Lord's doing and it's amazing in our eyes .The one who is oppressed, the rejected stone, due to the policies and systems that are developed on the needs of the elite will become the corner stone of the world. All are God's creation and people should realize that even the most marginalized bear the image of God. Everybody has the right to live the life in its fullness. This paper compares the Afro American oppression in Toni Morrison's *The Bluest Eye* and Indian dalit oppression in Arundhati Roy's *The God of small things*. Both the novels use the themes of racism and oppression to underscore the effects of post-slavery. Oppression of the downtrodden is seen in every corner of the world. The literature of Afro American is similar to dalit literature as both are records of the tragedy of their respective histories .The different setting and era in each novel suggest that the oppression and inequality had changed very little even after years later. Dalit literature and African American literature makes the readers understand their respective society and gives the answers of the fundamental questions of life and dignity. The paper also focuses on the oppression of many women who consider them as marginalized. Because of their gender, women are not valued and not respected in the society all over the world. This tragedy is examined through the works of Toni Morrison's *The Bluest Eye* and Arundhati Roy's *The God of Small Things*. Given that the two societies are different in terms of place and time, it is understandable that there should be certain limitations and differences in their literatures. On the other hand, there are similarities too. This paper is the study of similarities in Toni Morrison's *The Bluest Eye* and Arundhati Roy's *The God of Small Things*.*

#### INTRODUCTION

JANE THERESA

1P a g e



Arundhati Roy born on 18th February 1931 is a Nobel Prize and Pulitzer Prize winner. Her novels are known for their epic themes, vivid dialogue and richly detailed black characters. Her novels reflect the experience of the black community. *The Bluest Eye* is a novel which focuses on the experience of black women, the existence of the black women's desperate bid for survival in a white man's world. For Toni Morrison, the black artist has a responsibility to the black community, a quality of hunger and disturbance that never ends. Her novels bear witness to the reality of the black community and the reality of the blacks who survived under different circumstances. Morrison's novel is the true voice of the blacks in its original power. Morrison leads her readers to an understanding of racism. Even after the abolition of slavery, the whites have still continued to treat black women under subjection in the matter of the concept of beauty arising self hatred among the black women. The characters of both Alice Walker and Morrison show that they don't exist and always compared them to the whites.

*The Bluest Eye* deals mainly with the predominant idea of beauty of whites upon the blacks. This novel shows the reader that the concept of beauty is socially constructed.

*"Here is the house. It is green and white. It has a red door. It is very pretty."*(Morrison 18)

Mother, Father, Dick and Jane live in a pretty green house. The green symbolises that there is life and soul in the house. The red door symbolises the mystery in the story. White symbolises innocence and virginity. In the prologue the author focuses on Jane who wishes to play. Jane sees a cat, but the cat did not play with her. Jane's mother laughs but does not play with her. Her father smiles, but does not play with her. At last a friend comes to play along with Jane. The prologue is repeated word for word, a second time without punctuation. The paragraph is repeated a third time without punctuation and spaces between the words, which transforms the narrative into a rambling and disorienting block of text. The shift from oriented text to the rambling text makes the reader feel that the situation of isolation among the black girl is getting intense and torturous.

*"Our house is old, cold and green. At night a kerosene lamp lights one large room. The others are braced in darkness peopled by roaches and mice."*(Morrison 26)

A nine year old Claudia serves Morrison as the narrator of the story who is confused but sensitive witness to Pecola's tragedy. The central story is about eleven years old Pecola who is raped by her father and bears his child. The baby dies as it was premature and Pecola sinks into madness, with a notion that she has been granted her wish to have blue eyes and believes that now she is the most beautiful in the eyes of White Americans.

JANE THERESA

2P a g e



When we compare the novels *The Bluest Eye* by Toni Morrison and *The God of Small Things* by Arundhati Roy, both blacks and dalits have remained outside their culture excommunicated and exile. Afro Americans were brought directly from Africa to America to become slaves. Forced into slavery all that was left to the black man was his African soul. The blacks were vastly different from the white races. The black Americans are very concerned about the land of his origins. As the years went by legislatures abolished slavery and thereby the black gained freedom. But the inferiority was witnessed in every field they interacted.

The dalit in India is in similar situation. They were excluded from the society. They have been stripped of their dignity and denied basic human rights. They were considered untouchables implying that anybody touching them would be polluted. They were denied access to roads, temples, schools, etc to avoid pollution of other castes. Arundhati Roy's *The God of Small Things* is one such remarkable work which shows the sufferings and sorrows of the Dalits in a unique style. Booker Prize winner and activist-author Arundhati Roy is usually praised for her efforts in trying to represent the marginalised in her writing. All over the world every society has two categories of people, the higher level and the lower level. The people belonging to the higher level are at the top and they govern and exploit the people belonging to the lower level. Even though many political and economical changes have happened all over the world, the mindset of the people has not changed across the different cultures as well as the social discrimination against them even continue today. If the Dalit is the subjective of India's boycotted society, the African American is the self of Black America. One is abandoned and degraded by the White society and the other by Savarna society. One is brought and sold from their own home land and the other was called untouchable by birth. The women who belong to these outcastes are treated as marginalized. In both Dalit and Afro American society girls have a debased self image. Marginalised women discover themselves in both race and gender discrimination. The aim of this paper is to analyze the suppressed people's state in Arundhati Roy's *The God of Small Things* and Toni Morrison's *The Bluest Eye*. In both novels, the women struggle to survive in the world they live in because of their womanhood. A cross cultural study of both dalit and the black shows the cruel enslavement of both these two groups. The cruel oppression based on caste and race is responsible for the deprivation of the lives of the blacks and dalits.

When we look into Toni Morrison's *The Bluest Eye*, the blacks have to suffer a lot for their identity.

*"We know she is offering us something precious and that our pride must be arrested by refusing to accept."* (Morrison 25)



The black characters in the novel consider themselves as inferior when they interact with whites. The story centres on the lives of two black families, the Mac Teers and the Breedloves. The story is based on the children Claudia, Freeda and Pecola, their happy and painful experiences in growing up. The girls often had a loving conversation about how cute Shirley Temple was. Shirley Temple had golden curls, pink cheeks and blue eyes. Everyone loved her. Pecola had black skin. She was so poor and ugly.

*“The Breedloves did not live in a storefront because they were having temporary difficulty adjusting to the cutbacks at the plant. They lived there because they were poor and black, and they stayed there because they believed they were ugly.”(Morrison 53)*

The blacks believed that their poverty was traditional and stultifying, it was not unique. But their ugliness they believed that was unique. No one can convince them that they were not relentlessly and aggressively ugly. In her eleven years, no one had ever noticed Pecola. Each night Pecola prayed for blue eyes.

*“Frieda brought her four graham crackers on a saucer and some milk in a blue and white Shirley Temple cup. She was long time with the milk, and gazed fondly at the Silhouette of Shirley Temple’s dimpled face.”(Morrison 35)*

The whole novel explores the psychological and sociological changes in the protagonist, Pecola. Claudia was younger than both Frieda and Pecola. She had not yet arrived at the turning point in the development of psyche which would allow loving white dolls. During Christmas all exchanged gifts of big, special, blue eyed baby dolls.

*“I was physically revolted by and secretly frightened of those round moronic eyes, the pancake face and orange worm’s hair.” (Morrison 36)*

Pecola is the character who wants herself to look like the whites and wishes for the blue eyes. She believes that the symbol of white beauty is the blue eyes. She was having a wrong notion that only blue eyes would make her beautiful and believed that only blue eyes will help her in gaining her self-respect. As her eyes can never be altered into blue eyes in reality, her quest for blue eyes ends in madness. She cannot even look at a white girl as she believes that whiteness is the only standard of beauty and satisfies her envy by destroying white dolls.

*“I fingered the face wondering at the single stroke eyebrows picked at the pearly teeth stuck like two piano keys between red bowline lips. Traced the turned –up nose, poked the glarcy blue eyeballs, and twisted the yellow hair. I*

JANE THERESA

4Page



*could not love it. But I could examine it to see what it was that all the world said was lovable.”(Morrison 37)*

*“I destroyed white baby dolls.”(Morrison 38)*

The truly horrifying thing was the transference of the same impulses to little white girls. Black females possess hatred towards white women because of the set beauty concept by the society. The staring looks of the whites towards the blacks make them feel that they are ugly and unworthy.

*“I saw a pair of fascinated eyes in a dough- white face.” (Morrison 46)*

Toni Morrison shows that not all African Americans mindset are dominated by an oppressive culture. Some are very bold enough to survive in the midst of these oppressions. For example, the characters Claudia, the nine year old who is the narrator of the story is against the notion of the white standards of beauty. An independent and strong-minded nine-year-old, Claudia is a fighter and rebels against adults’ tyranny over children and against the black community’s idealization of white beauty standards. She has not yet learned the self-hatred that plagues her peers. She consciously deconstructs the ideology of the dominant society and understands the fact that a doll is a consumer item and tries to constrict Pecola by her destruction of white dolls.

*“Younger than both Frieda and Pecola , I had not yet arrived at the turning point in the development of my psyche which would allow me to love her.”(Morrison 35)*

In the novel Toni Morrison challenges the white standards of beauty and demonstrates that the concept of beauty is socially constructed.

*“Cholly, whose ugliness (the result of despair, dissipation and violence direct toward petty things and weak people) was behaviour, the rest of the family – Mrs.Breedlove, Sammy Breedlove and Pecola Breedlove wore their ugliness, put it on, so to speak, although it did not belong to them.” (Morrison 54)*

The Breedlove family are blacks who can never be like whites. Even though human beings look different, the soul is same. This realisation can bring some changes in the beauty concept. The whites looked at the blacks and wondered why they are so ugly. They observed them carefully to find the source of this ugliness which the blacks considered as staring. The realisation was that the ugliness came from conviction. They began to believe that some mysterious all knowing master had given each one a choke of ugliness to wear and they had

JANE THERESA

5P a g e



each accepted it without question. In the novel we can see that ugliness is something which can never be altered or changed, it is inherited from a powerful master.

*“You are ugly people. And they took ugliness in their hands, threw it as a mantle over them, and went about the world with it.” (Morrison 55)*

The novel helps the readers to understand that the standard of beauty is created by oneself. If the blacks value their blackness; they can subvert the ideology put forward by the white society. The background of the novel is racism, sexism and classicism which signifies the traumatic condition under which African Americans lived in White America. The restrictions upon the blacks affected their lives especially the women. They were always marginalised. The reason for the backwardness black people is because of the self hatred persuaded by white domination. Many of them considered themselves as inferior to the white women which ended in self hatred. They trust in their own unworthiness which is interpreted into ugliness. They considered themselves as unworthy for the society.

Throughout the novel, there are many incidents which show the feeling of separation and pain faced by Pecola Breedlove because of being black.

*“If those eyes of her’s were different, that is to say, beautiful, she herself would be different. Her teeth were good and at least her nose was not big and flat like some of those was thought so cute.” (Morrison 62)*

The novel shows several incidents which depicts the kind of world into which Pecola has been born. Pecola’s mother, who works as a house keeper in a white family, loves her employer’s children, ignoring her own daughter. No one expresses pity on her. Pecola is hurt not only because of her race but also because of her gender. Each night without fail she prayed for blue eyes. She has seen the hatred in the eyes of all white people. So she believed that the distaste must be for her blackness.

*“A picture of little Mary Jane, for whom the candy is named. Smiling white face, blonde hair in gentle disarray, blue eyes looking at her out of a world of clean comfort. The eyes are petulant and mischievous”. (Morrison 66)*

For the three girls to eat the candy was to eat Mary Jane. Throughout the novel, the author describes the mentally agonizing thoughts of these girls battling with the cultural standards of beauty that have been impaired upon them.

When we read the novels *The God of Small Things* by Arundhati Roy and *The Bluest Eye* by Toni Morrison, a lot of similarities in the mental thoughts of the characters can be observed.

JANE THERESA

6P a g e



Just like racism which is a prominent factor in dividing people in Western history, the caste system, a deep-rooted factor which is a shame for Indian culture, affects the socio-economic and socio-cultural systems of Indian society. Untouchables are the most exploited and unwanted ones. Some scholars believe that the Aryans, a fair-skinned race which invaded India had controlled and subjugated the dark-skinned aborigines placing them at the lower strata of society. Both the Dalits and the African Americans are distinctive groups that occupy a similar position in their respective societies- the bottom of the socio-economic hierarchy. In the famous essay, *Can the Subaltern speak?* By Gayathri Spivak, the writer suggests that the subaltern cannot have a history of his or her own and cannot have a voice if the subaltern is a female. She cannot be heard at all because she exists in absolute silence.

*“The subaltern as female is even more deeply in shadow.” (Spivak 28)*

In *The God of Small Things*, small things referred in the title are the subaltern people who are considered as small worthless creatures by most of the upper caste people. In reality these small people are the big ones who can bring a change to the whole system created by the society. These are the voice that should be given their voice, the voice that should be heard against the unreasonable hate, revenge and violence. The characters in the novel have their unfulfilled desires and are punished and silenced by the system in various ways. The women in *The God of Small things* are mostly confronted with marital and family problems. Estha and Rahel’s mother Ammu married Babu; however Babu turns out to be an alcoholic and even urges her to sleep with his boss, Mr. Hollick. After this incident Ammu leaves him and returns with the twins Estha and Rahel. Although a divorced daughter is a disgrace to a traditional Indian society, a divorcee son is not. Chacko, Ammu’s brother, is also a divorced but he returned to take charge of the family pickle business. The patriarchal privilege disproportionately over the other in the lives of the brother and sister. Ammu then falls into a love affair with Velutha, an untouchable.

*“Ammu travelled upwards through a dream in which a cheerful man with one arm held her close by the light of an oil lamp. He had no other arm with which to fight the shadows that flickered around him on the floor.” (Roy, 215)*

Ammu defies patriarchal domination, class and caste prejudice in public and pays with her life. Roy’s protagonists suffer from lack of parental love, disturbed infancy, broken homes. They are dissatisfied with their existence. They often choose to go out of the mainstream of life. This alienation generally manifests in immoral ties and activities. Alienation from their selves leads to a frantic search for their identity in the milieu through self-discovery and self-identification. She is banished from home and society because of this secret relation and she dies in another place because of this abandonment. Her relationship with Velutha is





considered to be a sin, as it is extra-marital and a crime as it is between the members of two different classes in the caste system.

*“If he held her, he couldn’t kiss her. If he kissed her, he couldn’t see her. If he saw her, he couldn’t feel her.” (Roy, 215)*

A related inferiority complex is evident in the interactions between untouchables and touchable in Ayemenem. Vellya Paapen is an example of an Untouchable so grateful to the touchable class. He is willing to kill his son, Velutha, when he discovers that Velutha has broken the most important rule of class segregation that there be no inter-caste sexual relations. A love-affair between Ammu and Velutha results in his brutal beating by a group of policemen. The beating takes place in front of the twins. This results in his death.

*“If they hurt Velutha more than they intended to, it was only because any kinship, any connection between themselves and him, any implication that if nothing else, at least biologically he was a fellow creature had been served long ago. They had no instrument to calibrate how much punishment he could take. No means of gauging how much or how permanently they had damaged him.” (Roy, 309)*

In part, this reflects how many untouchables have internalized caste segregation. Nearly all of the relationships in the novel are somehow coloured by cultural and class tension. Roy’s women characters in the novel are exploited. They are torn between their individuality and social obligations. Ammu sacrifices her life in her quest for identity. Estha is described as occupying very little space in the world. Ammu dies alone and sad, beaten by the world. Shadows gathered like bats in the steep hollows near her collarbone. Rahel never quite fits in, especially in such rigid confines as boarding schools. Velutha is the smallest of the small, as Ammu points out, calling her Ammukutty, ‘Little Ammu’, though she was so much less little than he was.

*“If he touched her, he couldn’t talk to her, if he loved her he couldn’t leave, if he spoke he couldn’t listen, if he fought he couldn’t win.” (Roy ,330)*

Ammu, on the other hand, defies the notion of the male-oriented society. She emerges as a rebel, voicing her suppressed voice. The capitalist society always treated women figures as commodity. They have no right over their body. Before marriage, they are under parental guidance and after marriage, under husband’s care. That’s why; we see that Ammu is denied of her college education whereas Chacko goes to Oxford. Even Ammu has no right in her father’s property. Mammachi, Baby Kochamma all accepted the female role-model imposed on them by the society – docile, submissive, ungrudging, stoic resignation. In the novel,

JANE THERESA

8P a g e



Velutha becomes the central and essential character and a sort of divinity in the eyes of the twins. Velutha is the children's only father figure and a true friend. Mammachi, Baby Kochamma, the policemen, in their realms of power, see to it that Ammu, Velutha, Rahel and Estha who hold no power in the social hierarchies remain vulnerable and overruled. Ammu, Velutha and the Twins, who get together for mutual love and warmth and not for any material gains are crudely acted upon and destroyed. The children who are the small things in the novel go against the rule and make Velutha their God, The God of Small Things.

The caste and gender hierarchies in India are equally relevant to the race and class as seen in *The Bluest Eye*. In both the novels, the children become victims of the communal response of the oppressed. By employing child narrators, both Morrison and Arundhati Roy explore how children negotiate different binaries between the beauty concepts, between male and female privileges, between higher and lower economic classes' and between upper and lower caste. The painful stories of Ammu and Pecola shows the authors concern for the silences that illustrates self destruction.

## WORKS CITED

1. Morrison, Toni. "The Bluest Eye", New York: Rinehart and Winston, 1970. Print
2. Roy, Arundhati. "The God of Small Things". London: Penguin Books, 1997. Print.
3. Spivak, Gayatri. "Can the Subaltern Speak?" Marxism and the Interpretation of Culture. Eds. Cary Nelson and Lawrence Grossberg. London: Macmillan, 1988. Print

(c) Insertion, (d) Drug injection, (e) Ablation. After removing the handle part, we only measured precision of operating mechanism. The test results, the error for the resulting target position is measured to within 2 mm.

**Conclusions:** Automatic injection and puncture device joining ultrasound probe is a device that is possible with just one hand ultrasonic imaging diagnosis and drug injection treatment to combine an automatic injection and puncture device to probe for ultrasound diagnosis. This device has a function that puncture guide service coupled with ultrasound image transmitted via a probe, automatic puncture to the target point in ultrasound image and drug injection and blood inhalation after needle insertion to the target point. In use benefits of this device are shorter operation time that the operation can be alone without assistance person and that puncture can be in the exact point, regardless of the skill of the surgeon.

**Acknowledgements:** This work was supported by the National Research Foundation of Korea (NRF) grant funded by the Korea government. (NRF-2016R1C1B2008460).

### 009 | Non-contact autonomic nervous system response measurement for psychiatric trauma treatment

Kun Ha Suh; Kyoung Lee; Dongkeun Kim; Eui Chul Lee  
*Intelligent Engineering Informatics for Human, Sangmyung University, Seoul, South Korea*

**Objectives:** To psychiatric treat trauma, a method to grasp the condition of a patient through a physiological reaction during psychiatric treatment and induce a therapeutic effect through feedback on the condition is widely used. Autonomic nervous system responses such as heart rate, respiration, and skin temperature are used as important objective indicators of the patient's emotional and psychological state. Traditionally, it is a method of attaching a sensor to the surface of a patient's skin and measuring the signal, but it can cause a sense of discomfort and unpleasantness

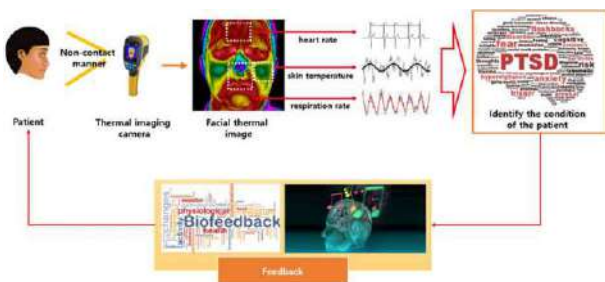


Figure 1 Overall flow of proposed method for measuring autonomic nervous system response using single thermal imaging camera.

due to the attachment of the sensor. These disadvantages can be more lethal for psychiatric patients.

**Methods:** In order to solve the problems, remote sensing methods without attaching sensors have been actively studied. In previous studies, there have been studies to measure heart rate and respiration without attaching sensors [1], but there has been no way to simultaneously analyze heart rate, respiration, and body temperature with a single sensor. In this study, we proposed a method which estimate the heart rate by observing the minute temperature change of the carotid artery, respiration rate by analyzing the temperature change due to the nostril inspiratory/exhalation, and skin temperature by analyzing facial thermal image as shown in Figure 1.

**Results:** The measurement accuracy of the skin temperature depends on the sensitivity of the thermal imaging camera, but the temperature of the surface of the skin can be continuously measured. The accuracy of the heart rate measurement method using the carotid artery blood vessel detection was about 98% of that of the ground-truth sensor. Respiration measurement by observing changes in the inspiratory/expiratory temperature of the nostrils was about 99%.

**Conclusions:** Our method will be used to identify the condition of trauma patients and can be used as a means of self-healing and tele-healthcare. Future studies will improve to be a robust measure of facial pose variation. In addition, we will develop a comprehensive emotion measurement system that considers the facial expression and voice analysis results together.

**Acknowledgement:** This study was funded by the Basic Science Research Program through the National Research Foundation of Korea (NRF) funded by the Ministry of Science, ICT and Future Planning (grant number NRF-2016R1C1B2014345). Also, this work was supported by the Industrial Strategic Technology Development Program (10073159, Developing mirroring expression based interactive robot technique by non-contact sensing and recognizing human intrinsic parameter for emotion healing through heart-body feedback) funded By the Ministry of Trade, industry & Energy (MI, Korea).

### 010 | Hybrid brainactuated muscle interface for the physically disabled

P.G. Vinoj<sup>1</sup>; Sunil Jacob<sup>2</sup>; Varun G. Menon<sup>3</sup>

<sup>1</sup>Electronics and Communication Engineering Department, APJ Abdul Kalam Technological University, India; <sup>2</sup>Centre for Robotics, SCMS School of Engineering and Technology, India; <sup>3</sup>Computer Science Engineering Department, SCMS School of Engineering and Technology, India

**Objectives:** According to Reeve Foundation 29% of paralysis is due to stroke followed by injury in the spinal cord.

Sometimes it may be difficult for a person to move the paralyzed person's body part as it may be too stiff. Our research focuses on actuating the paralyzed person's body part through his own thought process using Brain-Muscle Interface. The system uses Novel Technique which avoids the use of Exo-Skeleton.

**Methods:** In our current work, we propose a Hybrid Brain-Muscle Interface (HBMI) for the paralyzed person. The HBMI interface should have the provision for pre-processing, classifying, recording and training multidimensional EEG signals. The classifier module and the pre-processor module were implemented separately for easy testing and modification of different phases. The electrical signal from brain is captured using EEG and must be recorded during voluntary movement. When the brain does real time activities it must be detected and categorized into two dimensional movements. The non-invasive technique of recording EEG from the scalp is used for analyzing brain activity. This technique reduces the human mental workload and cost compared to invasive Technique. The excitation of the neurons is done using External audio and video feedback. The accuracy of the system is improved by combining Steady State Visually Evoked Potential (SSVEP) and Event Related Desynchronization (ERD) signals.

**Results:** The person suffering with Amyotrophic Lateral Sclerosis (ALS) is interfaced with HBMI. The HBMI generate electrical stimulation based on the subject's thought processing and in response to the stimulus the subject under test perform the desired movements of his/her body part. During the operation, the HBMI record the EEG signals, process it and classify it to different desired movements. The recorded operation is compared with the actual operations. The performance accuracy is measured. The performance accuracy is the number of correct classification divided by number of physical operations. A pair of EMG Electrodes must be placed on the identified body part. If the result is not satisfactory a Bio-feedback is given and the process is repeated till the performance accuracy is achieved.

**Conclusions:** The Hybrid brain muscle Interface (HBMI) will bypass the brain clotting and help the paralyzed person to move their paralyzed parts using brain stimulation without any Exo-skeleton. It is non-invasive and it does not require any exoskeleton for the motion. In it there is wireless connection between the brain and the controlled parts. Hybridization helps to classify the brain signals more accurately. Our findings will assist paralyzed person, and provide a better interface for the families, friends, and caretaker of the paralyzed person.

**Acknowledgements:** The part of the research was funded by EPICS in IEEE (Grant No. 2016-12).

## 011 | Seismocardiography system based on micromechanical sensors

Alexander Levkovich<sup>1</sup>; Vladimir Achildiev<sup>1</sup>; Viktor Soldatenkov<sup>1</sup>; Mikhael Basarab<sup>2</sup>; Nicolay Bedro<sup>1</sup>; Yury Gruzevich<sup>1,2</sup>; Yuliya Evseeva<sup>1</sup>; Natalya Konnova<sup>2</sup>; Mariya Komarova<sup>1</sup>

<sup>1</sup>Scientific Production Unity "GEOPHIZIKA-NV", St. Company, Moscow, Russia; <sup>2</sup>Bauman Moscow State Technical University, Moscow, Russia

**Objectives:** The purpose is to develop new equipment and algorithm for non-invasive diagnostics based on the seismocardiography (SCG) method.

**Methods:** SCG method is based on the recording of mechanical vibrations of the chest that are associated with the activity of the heart and is used to investigate the *strength* of the heartbeat and perform the analysis of the cardiac cycle.

**Results:** The SCG signal is significantly different in its view from the electrocardiogram and carries much more information. As supposed, SCG will significantly increase the number of diagnosed diseases with higher accuracy. The basis of the *SCG system* is a micro-vibration sensor based on microelectromechanical (MEMS) accelerometers. To eliminate the effect of angular vibrations on the data samples from accelerometers a new design of SCG system is proposed that include MEMS gyroscopes for the angular rate measurement in addition to MEMS accelerometers. The design of the *SCG system* includes a three-axis MEMS accelerometer unit and a three-axis MEMS angular velocity unit, a microcontroller and other necessary chips and elements. To provide high performance and small processing time, a microcontroller with high clock frequency is selected, and commands and data are received and transmitted via the built-in RS-422/485 interface or bluetooth interface if wireless communication is required.

The result of data processing is the modulus of the acceleration vector of the heartbeat and the attitude angles in the wander frame. The SCG system algorithm uses three frames and initial data about relationships between them: the body frame related to the body of the SCG system, the anatomical frame related to the heart and human body and the wander frame.

During the signal processing, pulse waves are extracted by digital filtering of *discrete in time* and quantized in *amplitude* signals, amplitude selection of pulse signals, their temporal analysis and calculation of the pulse vector module from its three projections on the axis of the body frame and the angles of the direction of the vector. Digital signal processing includes the implementation of fast wave approximation algorithms with subsequent analysis of approximating functions key parameters. As functional bases, both global (polynomials) and local (splines, wavelets, etc.) systems are tested. The error of the

# Parametric Study of Heat Transfer and Pressure Drop Characteristics of a Rectangular Offset Strip Fin Compact Heat Exchanger

 Rahul VR<sup>a</sup>, Ajith Kumar R<sup>b,\*</sup>
<sup>a</sup> Vidya Academy of Science and Technology, Thrissur

<sup>b</sup> SCMS School of Engineering and Technology, Ernakulam  
 ajithscms@gmail.com

Compact heat exchangers are of great topics of interest while we are dealing with the enhancement of heat transfer rate. In this study, a rectangular offset strip fin compact heat exchanger is taken into consideration. The purpose of this study is to develop a numerical model to study the heat transfer characteristics as well as the pressure drop characteristics. The parametric study was done in FLUENT with a three dimensional computational domain in which air is selected as working fluid. The analysis was confined to the flow in laminar region and so the Reynolds number was limited to 1000. The variation of friction factor and Colburn factor with Reynolds number is also analysed. The results obtained were analysed and were also compared with an existing correlation. The findings of this study may serve as a helping tool to develop a correlation for fluid flow in offset strip fin geometry.

## 1. Introduction

The compact heat exchangers are defined as those heat exchangers having ratio of the heat transfer surface area to its volume,  $\beta$  (area density) greater than or equal to  $700 \text{ m}^2/\text{m}^3$ . Compact heat exchangers are commonly used in gas-to-gas and gas-to-liquid (or liquid-to-gas) heat exchangers to counteract with the low heat transfer coefficient associated with gas flow with increased surface area. They found applications in many engineering sectors such as refrigeration, power, automotive, process, cryogenics etc. Various types of plate fin compact heat exchanger surfaces such as plain rectangular, plain trapezoidal, offset strip fin, wavy, louvered and perforated configurations are available. Here a rectangular offset strip fin heat exchanger is considered. They cause high heat transfer enhancement when compared to other surface configurations. This is due to the breaking or interruption of boundary layers formed on the uninterrupted fin surface and their dissipation in the fin wakes.

The monograph on the experimental investigations on offset strip fin geometry by (Kays et al., 1984) is still being used as a sourcebook. (Joshi et al., 1987) presented analytical models to predict the heat transfer coefficient and friction factor of offset strip fin geometry in both laminar and turbulent regimes. (Wieting 1975) developed empirical correlations for heat transfer and flow friction characteristics of offset strip fin geometry for Reynolds numbers in both laminar and turbulent ranges excluding the intermediate transition region. (Manglik et al., 1995) too developed single heat transfer and pressure drop correlations for all flow regimes after reanalysing previous experimental studies. (Saidi et al., 2001) conducted a numerical investigation of heat transfer enhancement in offset strip fin surface in self- sustained oscillatory flows. (Bhowmik et al., 2009) used a three-dimensional model to study the heat transfer and pressure drop characteristics of offset strip fin geometry with water as working medium. (Asadi et al., 2013) conducted case studies on the functions of friction and colburn factors in compact heat exchangers. (Muzychka et al., 2009) presented a model for thermal – hydraulic characteristics for offset strip fin geometry for large Prandtl number liquids. This study mainly focuses on analysing the heat transfer and pressure drop characteristics of offset strip fin geometry. The basic offset strip fin geometry is shown in figure 1. As per the experiments conducted and correlations developed by (Wieting 1975), the flow with Reynolds number  $\leq 1000$  is primarily laminar and flow having

Reynolds number range  $\geq 2000$  is primarily turbulent. In this study we are only dealing with laminar flow. The heat transfer enhancement in offset strip fin is due to the periodic starting and formation of boundary layers over the fin length and their dissipation in fin wakes.

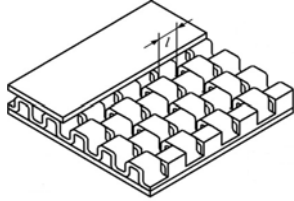


Figure 1: Offset strip fin geometry

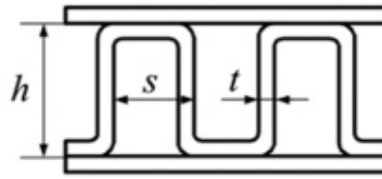


Figure 2: Nomenclature of offset strip fin

## 2. Problem description

The initial dimensions chosen were from the geometry designated as  $\frac{1}{4}$  (s) – 11.1 used by (Kays et al., 1984). A three-dimensional computation domain was created using Solidworks as shown in figure 3. This simplification is based on the assumption that the flow is fully developed and it shows a periodic pattern (fully developed periodic flow). ANSYS FLUENT was used for studying heat transfer and pressure drop characteristics.

As the flow in the offset strip fin geometry shows a fully developed periodic pattern, the inlet and outlet sections were given periodic boundary condition. The fins and the parting sheets were specified to be in isothermal condition (350 K). No slip condition was given for wall boundaries. The material for fin was specified as aluminium and the working fluid as air. The air is modelled as an ideal incompressible gas. The air enters the offset strip fin geometry at a low temperature (249 K) and as it flows through the geometry, the temperature of air increases.

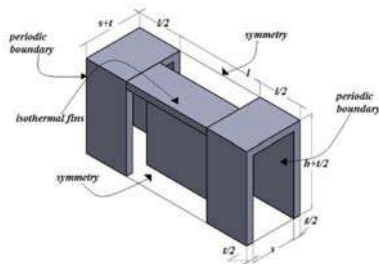


Figure 3: Computational domain

In this study a pressure-based solver was used. The semi implicit method for pressure – linked equation (SIMPLE) was used to solve the continuity, momentum and energy equations. The fluid flow was considered to be steady and incompressible. A convergence criterion of  $10^{-4}$  was selected for the continuity and momentum equations and a convergence criterion of  $10^{-6}$  was selected for the energy equation.

The continuity equation is given by:

$$\frac{\partial(\rho u)}{\partial x} + \frac{\partial(\rho v)}{\partial y} + \frac{\partial(\rho w)}{\partial z} = 0 \quad (1)$$

The momentum equation in x-direction is given by:

$$\rho \left( u \frac{\partial u}{\partial x} + v \frac{\partial v}{\partial y} + w \frac{\partial w}{\partial z} \right) = -\frac{\partial P}{\partial x} + \mu \left( \frac{\partial^2 u}{\partial x^2} + \frac{\partial^2 u}{\partial y^2} + \frac{\partial^2 u}{\partial z^2} \right) \quad (2)$$

The Reynolds number for the flow is given by:

$$Re = \frac{U_c D_h}{\nu} \quad (3)$$

Now the free flow area denoted as  $A_{ff}$  for the computational domain can be written as,  $A_{ff} = sh$ . The hydraulic diameter  $D_h$  is given by:

$$D_h = \frac{4 A_{ff}}{A/l} = \frac{4shl}{2(sl+hl+th)+ts} \quad (4)$$

The friction factor  $f$  is given by:

$$f = \frac{2\Delta P}{\rho U_c} \left( \frac{D_h}{4 L_m} \right) \quad (5)$$

The Colburn j factor is given by:

$$j = \frac{\bar{h} Pr^{2/3}}{\rho C_p U_m} \quad (6)$$

### 3. Results and discussions

The computational domain was analysed in FLUENT and the obtained results were compared with an existing correlation made by Manglik & Bergles (1995). They had given the correlations for the friction factor as well as for the Colburn factor. The correlations were:

$$f = \frac{9.6243 Re^{-0.7422} \alpha^{-0.1856} \delta^{0.3053} \gamma^{-0.2659}}{1 + (7.669 \times 10^{-8} Re^{4.429} \alpha^{0.920} \delta^{3.767} \gamma^{0.236})} \quad (7)$$

$$j = \frac{0.6522 Re^{-0.5403} \alpha^{-0.1541} \delta^{0.1499} \gamma^{-0.0678}}{1 + (5.269 \times 10^{-5} Re^{1.340} \alpha^{0.504} \delta^{30.456} \gamma^{-1.055})} \quad (8)$$

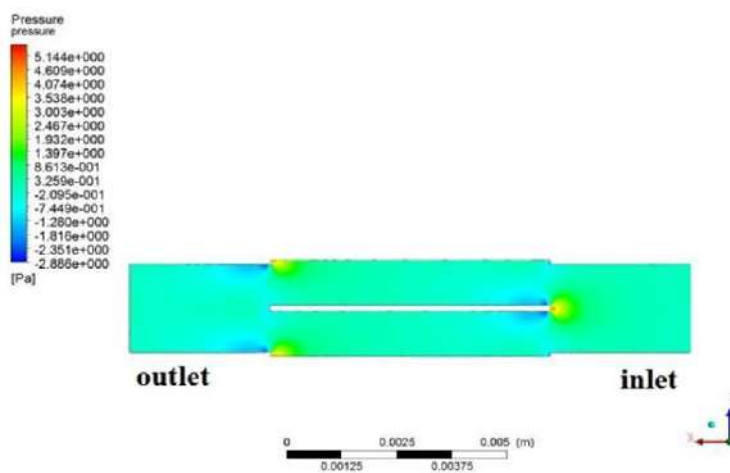


Figure 4: Pressure contour

The pressure, temperature and velocity contours for a flow through an offset strip fin geometry ( $Re = 500$ ) are shown in figures 4, 5 and 6 respectively. It was observed that there occurs a pressure drop as the fluid flows through the offset strip fin geometry. Also, the periodic behaviour of the flow can clearly be observed from the velocity contour.

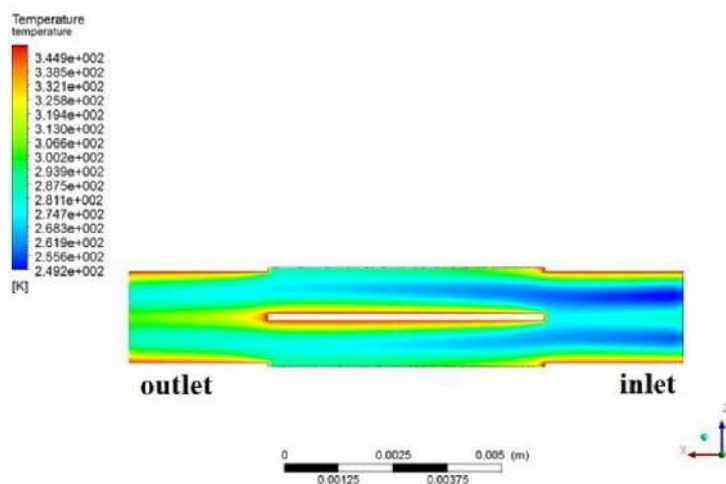


Figure 5: Temperature contour

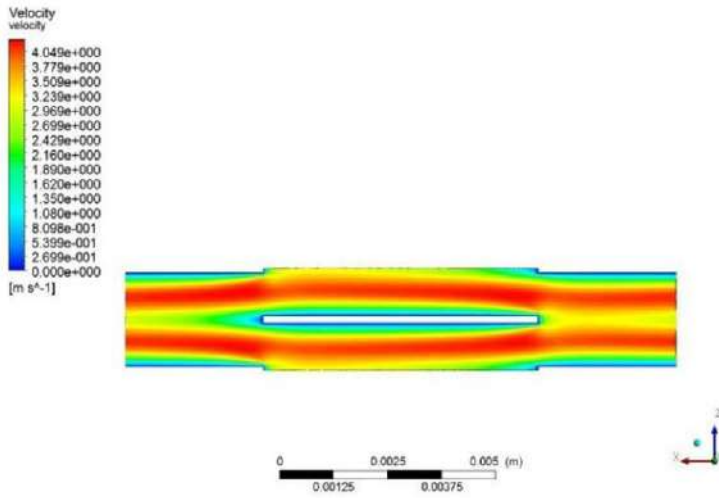


Figure 6: Velocity contour

### 3.1 Variation of $f$ and $j$ factors with Reynolds number

Initially, the variation of  $f$  and  $j$  factors with respect to Reynolds number was analysed. From the figure 7 below it is clear that the functions of  $f$  and  $j$  factors decrease with increasing Reynolds number. At lower flow velocities the air spends more time around the fins and thus it helps in enhancing the heat transfer rate. As the flow velocity increases the time spend by air around the fins decreases resulting in less heat transfer. The computed results of  $f$  factor obtained were very close to the values predicted by the Manglik & Bergles correlation, and the  $j$  factors deviated by about 12%. And also, the values of friction factors were about 10 times the values of  $j$  factors at the same Reynolds number.

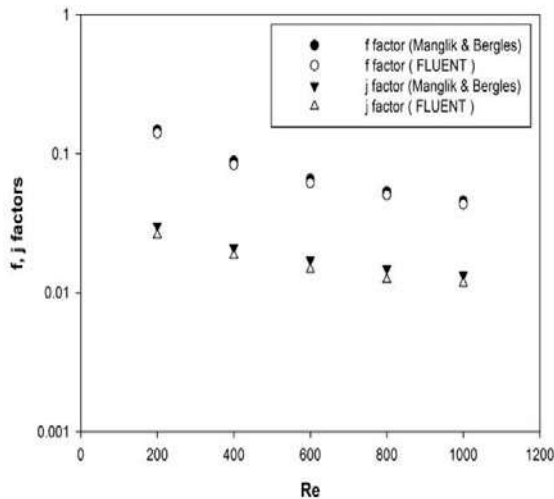


Figure 7: Variation of  $f$  and  $j$  factors with Reynolds number

### 3.2 Variation of $f$ and $j$ factors with dimensionless parameter $\alpha$

Now the heat transfer and pressure drop characteristics of the offset strip fin geometry was analysed by varying the dimensionless parameter  $\alpha = s/h$ . The dimensionless parameter  $\alpha$  was varied by changing the fin height  $h$ . The variation of  $f$  &  $j$  factors with variation of  $\alpha$  is shown in figure 8. At low values of  $\alpha$ , the functions of  $f$  and  $j$  factors are high and the trend shows that the  $f$  and  $j$  factors decrease with increasing values of  $\alpha$ .



The  $f$  and  $j$  factor variation obtained by FLUENT with respect to  $\alpha$ , deviated from the predicted  $f$  factor by about 5% and the from the predicted  $j$  factor by about 12%.

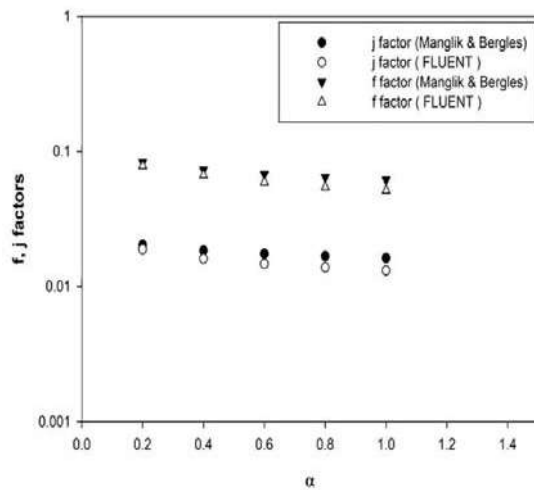


Figure 8: Variation of  $f$  and  $j$  factors with dimensionless parameter  $\alpha$

### 3.3 Variation of $f$ and $j$ factors with dimensionless parameter $\delta$

The  $f$  &  $j$  factor variations with respect to the dimensionless parameter  $\delta = t/l$  was also obtained. Both the offset fin length and fin thickness will have an influence on the flow field. When the fins are thicker, they offer large form drag. Also, in an offset strip fin geometry having smaller offset fin length, the breaking of boundary layers formed on the uninterrupted fin length and their dissipation in fin wakes will be more often when compared to a geometry having larger offset fin length. As a result, the pressure drops and colburn  $j$  factor tends to increase. As indicated in the figure 9, the functions of  $f$  and  $j$  factor increases with increase in  $\delta$ . In this study, the  $\delta$  was varied by changing the fin uninterrupted length  $l$ . So, for large values of  $\delta$ , the offset fin length was small resulting in higher values of  $f$  and  $j$  factors. The deviation of friction factor data obtained from FLUENT deviated from the existing values by about 8% and the deviation in case of colburn factor was found to be 10%.

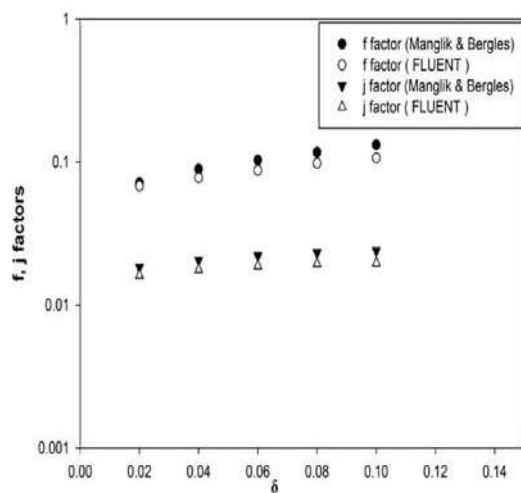


Figure 9: Variation of  $f$  and  $j$  factors with dimensionless parameter  $\delta$

## 4. Conclusions

In this study, a three dimensional parametric analysis of a rectangular offset strip fin heat exchanger using ANSYS FLUENT 14.0 was carried out. The analysis was carried out for Reynolds number  $\leq 1000$ . A three-dimensional computational domain was created and suitable boundary conditions were defined. The heat

transfer characteristics and pressure drop characteristics were analysed by varying dimensionless parameters such as Reynolds number,  $\alpha = s/h$ ,  $\delta = t/l$ . The results show that  $f$  &  $j$  factors decrease with respect to increase in Reynolds number and  $\alpha = s/h$ . On the other hand,  $f$  &  $j$  factors increase with respect to increase in  $\delta = t/l$ . It was also found that the main factors influencing the design of a compact heat exchanger are Colburn  $j$  factor and Fanning friction factor.

### Nomenclature


$A_{ff}$	free flow area
$D_h$	hydraulic diameter
$f$	friction factor
$h$	fin height
$\bar{h}$	mean heat transfer coefficient
$j$	colburn factor
$l$	offset fin length
$L_m$	length of computational module
$Pr$	Prandtl number
$Re$	Reynolds number
$s$	fin spacing
$t$	fin thickness
$U_m$	mean velocity
$U_c$	velocity at minimum free flow area
$\mu$	dynamic viscosity
$\nu$	kinematic viscosity
$\rho$	density
$P$	pressure
$u$	velocity component in x direction
$v$	velocity component in y direction
$w$	velocity component in z direction

### References

- Asadi M., Nadali A., 2013, Study on the functions of friction and colburn factors in compact heat exchanger, *Wyno Academic Journal of Engineering & Technology Research*, 4, 37-48.
- Bhowmik H., Kwan-Soo Lee, 2009, Analysis of heat transfer and pressure drop characteristics in an offset strip fin heat exchanger, *International Communications in Heat and Mass Transfer*, 36, 259 – 263.
- Dong J.Q., Chen J.P., Chen Z.J., Zhou Y.M., 2007, Air-side thermal hydraulic performance of offset strip fin aluminum heat exchangers, *Applied Thermal Engineering*, 27, 306–313. DOI: 10.1016/j.applthermaleng.2006.08.005
- Joshi H.M., Webb R.L., 1987, Heat transfer and friction in the offset strip fin heat exchangers, *International Journal of Heat and Mass Transfer*, 30, 69 – 84.
- Kays W.M., London A.L., 1984, *Compact Heat Exchangers*, 3rd ed. McGraw-Hill, New York.
- Manglik. R.M., Bergles A.E., 1995, Heat transfer and pressure drop correlations for the rectangular offset strip fin compact heat exchanger, *Experimental Thermal Fluid Science*, 10, 171–180. DOI: 10.1016/0894-1777(94)00096-Q
- Muzychka Y.S., Kenway G., 2009, A model for thermal-hydraulic characteristics of offset strip fin arrays for large Prandtl number liquids, *Journal of Enhanced Heat Transfer*, 16, 73–92.
- Saad S.B., Clément P., Fourmigué J.F., Gentric C., Leclerc J.P., 2012, Single phase pressure drop and two-phase distribution in an offset strip fin compact heat exchanger, *Applied Thermal Engineering*, 49, 99–105. DOI: 10.1016/j.applthermaleng.2011.09.022
- Saidi A., Sunden B., 2001, A numerical investigation of heat transfer enhancement in offset strip fin heat exchangers in self-sustained oscillatory flows, *International Journal of Numerical Methods for Heat & Fluid Flow*, 11, 699-716. DOI: 10.1108/eum000000005984
- Wieting A.R., 1975, Empirical correlations for heat transfer and flow friction characteristics of rectangular offset-fin plate – fin heat exchangers, *International Journal of Heat and Mass Transfer*, 97, 488–490.

Article

# Numerical Study on the Influence of Mass and Stiffness Ratios on the Vortex Induced Motion of an Elastically Mounted Cylinder for Harnessing Power

Vidya Chandran <sup>1</sup>, Sekar M. <sup>2</sup>, Sheeja Janardhanan <sup>3,\*</sup> and Varun Menon <sup>4</sup> 

<sup>1</sup> Department of Mechanical Engineering, Karunya Institute of Technology and Sciences, Coimbatore, Tamil Nadu 600018, India; vidya.rudn@gmail.com

<sup>2</sup> Department of Mechanical Engineering, AAA College of Engineering and Technology, Sivakasi, Tamil Nadu 600018, India; mailtosekar@gmail.com

<sup>3</sup> Department of Mechanical Engineering, SCMS School of Engineering and Technology, Ernakulam, Kerala 673307, India

<sup>4</sup> Department of Computer Science and Engineering, SCMS School of Engineering and Technology, Ernakulam, Kerala 673307, India; varungmenon46@gmail.com

\* Correspondence: sheejajanardhanan@scmsgroup.org; Tel.: +91-828-194-3531

Received: 10 September 2018; Accepted: 25 September 2018; Published: 27 September 2018



**Abstract:** Harnessing the power of vortices shed in the wake of bluff bodies is indeed a boon to society in the face of fuel crisis. This fact serves as an impetus to develop a device called a hydro vortex power generator (HVPG), comprised of an elastically mounted cylinder that is free to oscillate in the cross-flow (CF) direction even in a low velocity flow field. The oscillatory motions in turn can be converted to useful power. This paper addresses the influence of system characteristics viz. stiffness ratio ( $k^*$ ) and mass ratio ( $m^*$ ) on the maximum response amplitude of the elastically mounted cylinder. Computational fluid dynamics (CFD) simulations have been used here to solve a two way fluid–structure interaction (FSI) problem for predicting the trend of variation of the non-dimensional amplitude  $Y/D$  with reduced velocity  $U_r$  through a series of simulations. Maximum amplitude motions have been attributed to the lowest value of  $m^*$  with  $U_r = 8$ . However, the maximum lift forces correspond to  $U_r = 4$ , providing strong design inputs as well as indicating the best operating conditions. The numerical results have been compared with those of field tests in an irrigation canal and have shown reasonable agreement.

**Keywords:** computational fluid dynamics (CFD); flow around cylinder; fluid structure interaction (FSI); hydrodynamic response; numerical methods; simulation and modeling; vortex induced vibration (VIV) ratio

## 1. Introduction

As the sources of fossil fuels are depleting at a faster pace, energy scientists all over the world are keen on the search for new technologies that can provide renewable and clean energy. Hydroelectric power generation is of course a clean source of energy, but considering the capital investment and the effects of dams on natural ecosystems, the need for a much cleaner energy source becomes more important. This paper discusses the design and manufacture of the hydro vortex power generator (HVPG) model, which when scaled up can be viewed as one such cleaner source of electricity. Also, the paper discusses a numerical method to optimize the design parameters of HVPG model. The principle behind the working of HVPG is vortex shedding in the wake of bluff bodies in fluid flow. The phenomenon of vortex shedding behind bluff bodies has been an extensively researched topic [1,2]. The presence of such vortex shedding has been considered undesirable and researchers had been in

search of methods to suppress vortex shedding [3]. Vortex power was proved useful to mankind by the researchers at Michigan University, who first converted vortex power into electricity [4,5]. HVPG works on the principle of vortex induced vibration of bluff bodies subjected to fluid current. The power of vortices shed in the wake of these bluff bodies are converted into vibration energy and then into electricity. HVPG can be made useful as a single standing power unit that can provide electricity to remote locations; and also as a multiunit module which can supply power to the grid [6]. The paper discusses the design optimization of a single, power-generating, scaled-down module, harnessing power from vortices. In this paper, an attempt has been made to optimize the design based on the major influencing parameters, oscillating mass ratio ( $m^*$ ) and stiffness ratio ( $k^*$ ). Griffin consolidated experimental results and plotted them to show the dependence of maximum amplitude on system characteristics [7]. However, the drawback of Griffin's plot was its considerable scatter which could be attributed to the inclusion of mode shapes also as an influencing parameter. Later researchers could successfully reduce the scatter in Griffin's plot and establish a simple relationship between maximum amplitude and mass damping parameter by eliminating mode shapes from the list of variables [7,8]. The simplified mass damping parameter as in [8] was applicable for cylinders of high and low mass ratios equally. Many researchers have formulated empirical formulae to express the parametric relationship and experimentally verified the correlations [9,10]. Later in the experiments, however, it has been observed that with variation in the damping ratio,  $U_r$  and the Strouhal number ( $St$ ) varies [11]. Also, these experiments revealed relatively larger response amplitude compared to other studies. Recently researchers have also succeeded in theoretically proving the effectiveness of harnessing VIV energy for powering underwater mooring platforms [12].

The present work studies the influence of  $k^*$  and  $m^*$  on maximum response amplitude of an elastically mounted cylinder with a single DOF. It also provides a detailed insight into the vortex shedding pattern at various  $U_r$ . The simulations are carried out at  $Re$  of the order  $10^4$  which corresponds to the realistic flow regime encountered by power generating vortices [13]. The numerical results have been verified using field tests conducted at Palissery irrigation canal (Palissery irrigational canal is one of the irrigation projects by Government of Kerala located in Thrissur district, Kerala, India).

Previous studies in the same domain had only considered the effect of complex and coupled parameters such as the Skop Griffin parameter [14]. The novelty in the present work is the effort made to represent the influence of tangible parameters viz the stiffness coefficient and mass of the cylinder. These parameters are easily controllable from a designer's point of view. A non-dimensional approach has been used here to generalize the results for the design of power harnessing devices of any scale.

## 2. The Concept of HVPG

HVPG works on the principle of vortex induced vibration (VIV). If a bluff body is not completely secured with at least one degree of freedom motion, and the frequency of vortex shedding matches the natural frequency of the structure, the structure begins to resonate, vibrating with harmonic oscillations of large amplitude. This phenomenon is known as 'lock-in'. During lock-in, vortex shedding frequency shifts to the natural frequency of the structure, leading to large amplitude vibrations. Vortex shedding in the wake of a cylinder is shown in Figure 1.

The vortex shedding occurs at a discrete frequency and is a function of the Reynolds number ( $Re$ ), defined by Equation (1)

$$Re = \frac{\rho V D}{\mu} \quad (1)$$

The dimensionless frequency of the vortex shedding,  $St = f_v D/V$ , is approximately equal to 0.2 when the Reynolds number is greater than 1000 [15]. When vortices are shed from the cylinder, uneven pressure distribution develops around the upper and lower surfaces of the cylinder, generating an

oscillating hydrodynamic lift force on the cylinder. This unsteady force given by Equation (2) can induce significant cross flow vibrations on a structure, especially if the resonance condition is met.

$$F_L = C_L \frac{1}{2} \rho A V^2. \quad (2)$$

where  $F_L$  is the lift force and  $C_L$  is the coefficient of lift.  $\rho$  is the density of water,  $A$  the projected area in the direction of flow, and  $V$  is the velocity of flowing water. The cylinder also experiences a net force along the flow direction and is called the drag force and is given by the Equation (3).

$$F_D = C_D \frac{1}{2} \rho A V^2 \quad (3)$$

where  $F_D$  is the drag force and  $C_D$  is the drag coefficient.

The oscillating lift force acting on the cylinder makes the cylinder oscillate in the cross flow (CF) direction at the frequency of vortex shedding. For the making of HVPG, the cylinder has been mounted elastically, which enables the entire module to be considered as a spring-mass system with the cylinder considered as the mass and the elastic supports as springs. When the natural frequency of spring-mass system matches the vortex shedding frequency, the cylinder oscillates with large amplitudes. The linear motion of the mass can then be converted to rotary motions through a slider-crank mechanism and the crank rotations can be used to drive a generator unit.

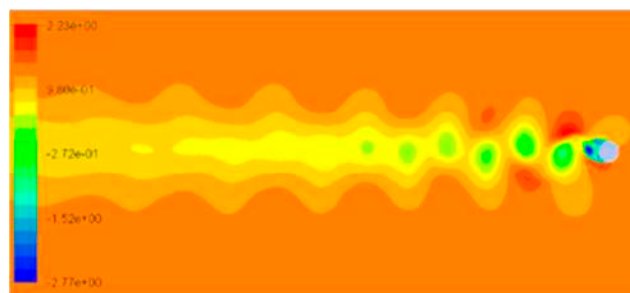


**Figure 1.** Shedding of alternate vortices behind a cylinder represented as pressure (N/m<sup>2</sup>) contours. (Von Kármán Vortex Street).

### 3. Mathematical Model

A single power module of HVPG has been modeled as a spring mass system undergoing instability induced vibration. The instability is caused by the shedding of vortices in the wake of the cylinder when the flow encounters a bluff body. Alternate vortex shedding causes oscillatory forces that induce structural vibrations, where the rigid cylinder is now similar to a spring-mass system with a harmonic forcing term. This phenomenon is referred to as heave motion [14]. Equation of motion [16] for this system can be written as

$$m\ddot{Y} + c\dot{Y} + kY = F(t) \quad (4)$$

where  $Y$  is the displacement of the cylinder under VIV in the cross-flow direction;  $m$  is the sum of mass of the oscillating system or body mass,  $m_b$  and added mass of the system,  $m_a$ .  $m_a$  is defined as  $m_a = C_A m_b$ , where  $C_A$  is the added mass coefficient.  $c$  is the damping coefficient and  $k$  is the coefficient of stiffness of the spring mass system.  $F(t)$  is the time varying force acting on the cylinder due the flow instability. Relatively small oscillation amplitudes are approximated by

$$F(t) = F_L \sin(\omega_v t + \varphi) \quad (5)$$

where  $\omega_v$  is the circular frequency of vortex shedding and  $\varphi$  the phase difference between the force and cylinder displacement.  $F_L$  is the maximum value of oscillating hydrodynamic lift force acting on the cylinder and is given by Equation (2).

The amplitude of oscillation of the system depends on the mass ( $m^*$ ) ratio of the oscillating cylinder given by

$$m^* = \frac{m}{m_{fd}} \quad (6)$$

where  $m_{fd}$  is the mass of fluid displaced by the oscillating mass. The maximum possible response amplitude at any  $Re$ ,  $Y_{max}$  can be calculated from the empirical relation between non-dimensional amplitude ( $A_y = \frac{Y_{max}}{D}$ ) and  $Re$  [10] as given by Equation (7).

$$A_Y = -0.4435 \left[ \log \frac{\alpha}{Re} \right] - 1.5 \quad (7)$$

where  $\alpha$  is defined as

$$\alpha = (m^* + C_A)\zeta \quad (8)$$

where  $C_A$  is the added mass coefficient and  $\zeta$  is the damping ratio.

Maximum amplitude of oscillation occurs when shedding frequency locks on to the natural frequency of the oscillating system ( $f_n$ ). This condition is known as lock-in. Amplitude of oscillation of a spring mass system can also be obtained from Equation (9)

$$Y = \frac{F_L}{k} \left[ \frac{1}{\sqrt{(1 - \eta^2)^2 + (2\zeta\eta)^2}} \right] \quad (9)$$

where  $\eta$  is the frequency ratio represented by Equation (10)

$$\eta = \frac{f_n}{f_v} \quad (10)$$

where  $f_v$  is the vortex shedding frequency. During lock-in  $\eta = 1$  and Equation (9) simplifies as shown by Equation (11).

$$Y = \frac{F_L}{2k\zeta} \quad (11)$$

The paper discusses effect of mass and stiffness ratios of the oscillating cylinder on the maximum response amplitude. The structural damping variations are not considered as it is observed to be less significant compared to its inertia and elastic counterparts. Also, mass and stiffness of the system are more tangible parameters from design point of view compared to damping. Moreover, the study focuses on non-dimensionalizing the influencing parameters so that results hold applicable for prototypes and models equally. Many researchers have considered the combined effect of mass and damping through mass damping parameter  $m^*\zeta$ . In such analysis also  $\zeta$  is kept constant and  $m^*$  is varied independently [17].

#### 4. Numerical Determination of Hydrodynamic Lift Forces and Motions

Vortex induced vibration, a two-way fluid structure interaction phenomenon, is complex in nature due to the fact that the cylinder displacement is capable of changing the vortex shedding pattern behind it leading to a variation in the hydrodynamic load acting on the cylinder. Parameters  $k^*$ ,  $m^*$ , and  $c$  have significant influence on the oscillation amplitude. A significant amount of research has been carried out to bring clarity on the influence of these parameters on the maximum cylinder response amplitude. Experiments conducted by [18] could capture lock-in phenomenon for a cylinder with a single degree of freedom. It was observed that cylinder oscillation frequency matches with vortex shedding frequency for cylinders having low mass ratios [19]. For mass ratios below critical mass ratio,  $m^*_{cr}$ , the range of  $U_r$  over which resonance occurs tend to extend towards infinity. The following section of the paper is an effort to understand the effect of mass and stiffness coefficient on the response

of cylinder numerically in a simpler and economic way, and the results of the numerical study is verified using a field test.

#### 4.1. Modeling the Flow

Numerically this problem has been treated as a case of two-way fluid structure interactions (two-way FSI). Modeling and meshing has been performed in ANSYS ICEM CFD (version 12) [20] and solving using ANSYS FLUENT (version 12) [21]. Flow around the cylinder is modeled using the transient, incompressible Navier–Stokes equation based RANS solver with  $k-\omega$  SST as the turbulence model. The RANS solver does the virtual averaging of velocities over an interval of time and hence for a specific interval the velocity vector appears to be constant in a RANS solver. In the present work, an optimized fine grid is used to compensate for this drawback of the solver enabling it to capture the physics of von Kármán street eddies. RANS solver for transient two-dimensional analysis can be explained as follows [21]

$$\frac{\partial \rho}{\partial t} + \frac{\partial}{\partial x_i}(\rho u_i) = 0 \quad (12)$$

$$\frac{\partial}{\partial t}(\rho u_i) + \frac{\partial}{\partial x_i}(\rho u_i u_j) = -\frac{\partial p}{\partial x_i} + \frac{\partial}{\partial x_j} \left[ \mu \left( \frac{\partial u_i}{\partial x_j} + \frac{\partial u_j}{\partial x_i} - \frac{2}{3} \delta_{ij} \frac{\partial u_l}{\partial x_l} \right) \right] + \frac{\partial}{\partial x_j}(-\rho \overline{u'_i u'_j}) \quad (13)$$

where  $u_i$  and  $u'_i$  are mean and fluctuating velocity components for  $i = 1, 2$ , and 3.

The velocities and other solution variables in the above equation represent the time averaged values. Equation (12) is solved by modeling Reynolds stresses  $\overline{\rho u'_i u'_j}$ , effectively using  $k-\omega$  SST as turbulence model [22].  $k-\omega$  SST is capable of accurately predicting the commencement and the intensity of flow separation at fixed boundaries while the standard  $k-\epsilon$  model has proved its efficacy in predicting the wake characteristics accurately. This fact has been established after extensive studies conducted by the authors.  $k-\omega$  SST turbulence model demands a very high near wall grid resolution and hence the maximum element size is fixed to be less than  $1 \times 10^{-4}$ , which satisfies CFL criterion and near wall  $y^+$  values.

The above governing equations are discretized using finite difference method. Non iterative time advancement (NITA) scheme with fractional time stepping method (FSM) has been chosen for pressure-velocity coupling of the grid. A Least Squares Cell Based scheme is used for gradient in spatial discretization and a second order upwind scheme as convective scheme.

#### NITA

For capturing the physics of the flow with accuracy in the boundary as well as in the wake of the cylinder, the computational grid needs to be extremely fine. Solving a dynamic mesh case with such extreme grid fineness using iterative time advancement scheme demands a considerable number of iterations to be performed using a very small time step size to satisfy the dynamic mesh criteria. This in turn leads to huge computational cost and effort. As an alternative and computationally economic method, in the present work, NITA with FSM has been implemented. NITA scheme assures the same time accuracy by reducing the splitting error, which occurs while solving the discretized Navier–Stokes equation to the same order as the truncation error. Splitting error need not be reduced to zero in NITA scheme, saving a lot of computational effort.

#### 4.2. Structural Modeling

An elastically mounted cylinder can be mathematically represented by Equation (4). This equation of motion is solved using six degrees of freedom solver (6DOF), an integral part of the main solver by defining the cylinder as an object with one degree of freedom (1DOF) in transverse direction. A user defined function (UDF) compiled in C programming language has been hooked to the cylinder dynamic boundary conditions. The governing equation for the motion of the center of gravity of

the cylinder in the transverse direction is solved in the inertial coordinate system. Velocity in the transverse direction is obtained by performing integration on Equation (14).

$$\ddot{Y} = \frac{1}{m} \sum F \quad (14)$$

where  $\ddot{Y}$ , is the translational acceleration in the transverse direction,  $m$  is the mass of the cylinder and  $F$ , resultant fluid force acting on the cylinder. Position of the center of gravity of the cylinder (CG) is updated after solving the equation of motion of a spring mass system.

$$m\ddot{Y} + c\dot{Y} + kY = F(t) \quad (15)$$

The inertial force term on the left-hand side of Equation (15) is computed by the 6DOF solver for each time step from Equation (14) and the UDF hooked to the moving cylinder inputs the restoring force term as 6DOF load acting on the cylinder. Mass of the cylinder is given in the UDF as

$$m = m_b + m_a \quad (16)$$

$$m_a = (1 + C_A)m_b \quad (17)$$

Added mass coefficient  $C_A$  for the aspect ratio of the present model is found to be equal to 0.7 [13].

#### 4.3. Mesh Deformation

Mesh motion to adapt to the movement of the cylinder is achieved by using displacement based smoothing algorithm. The governing equation for mesh motion is represented by Equation (18).

$$\nabla \cdot (\gamma \nabla \vec{u}) = 0 \quad (18)$$

where  $\vec{u}$  is the velocity of mesh displacement. The boundary conditions for Equation (18) are computed by the 6DOF solver and the boundary mesh motion diffuses into the interior of the deforming mesh according to the Laplace equation, Equation (18). Diffusion coefficient,  $\gamma$  is calculated using boundary distance formulation given by Equation (19).

$$\gamma = \frac{1}{d^\tau} \quad (19)$$

where  $\tau$  is the diffusion parameter and  $d$  is the normalized boundary distance. Diffusion parameter is set as unity to avoid excessive deformation of the near cylinder elements.

#### 4.4. Fluid Structure Interaction

In this paper, a two-way implicit approach is used to study the effect of  $m^*$  and  $k^*$  on the response of cylinder under VIV. Flow equations and structural equations are solved simultaneously in iterations with a time step. A flow chart for the solution procedure is shown in Figure 2.

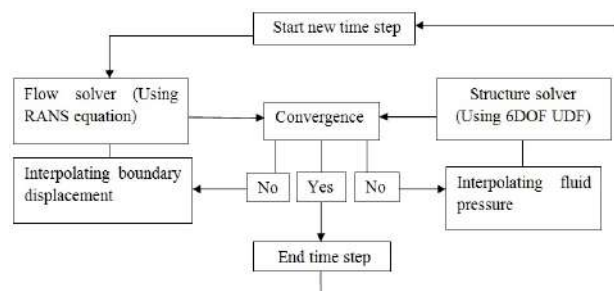


Figure 2. Flow chart of two-way implicit FSI solution procedure.



## 5. Problem Description

### 5.1. Simulation Parameters

In the present study, geometrically identical cylinders of different masses are considered for VIV of an elastically mounted horizontal cylinder. Based on the present study, a basic model of HVPG as in [5] was fabricated and a field study was carried out on it for verifying the numerical results. The main parameters of the model are summarized in Table 1. The model has an aspect ratio of 13.12 and an outer diameter of 0.0762 m. The structural damping is considered to be zero in the present study. The computational domain for the study is shown in Figure 3a. The representation of the present problem as a spring-mass system is depicted in Figure 3b. The mesh fineness is indicated in Figure 3c and the grid used for the present computation is represented by Figure 3d.

**Table 1.** Properties of the elastically mounted cylinder model.

Properties	Values	Units
Diameter of the cylinder ( $D$ )	0.0762	m
Aspect ratio of the cylinder ( $L/D$ )	13.12	-
Flow velocity ( $V$ )	0.5	m/s
Reynolds Number of flow ( $Re$ )	$3.8 \times 10^4$	-
Mass ratio ( $m^*$ )	0.66	-

A simple representation of the two-dimensional computational domain for the cylinder is displayed in Figure 3a. The flow direction is parallel to the global  $x$ -axis and the flow velocity is set to be 0.5 m/s. Domain size is fixed based on previously published analysis and allowance is given to accommodate the vertical motion of cylinder boundary [23]. Simulations are performed for three different values of mass ratio,  $m^* = 0.66, 1.32,$  and  $1.98$  which correspond to moderate mass ratios above  $m^*_{cr}$ , for which maximum response is confined to the range of  $U_r = 4-12$ . For fixed mass, influence of stiffness ratio  $k^*$  is studied by varying the reduced velocity value which is defined as

$$U_r = \frac{V}{f_n D} \quad (20)$$

$$f_n = \frac{1}{2\pi} \sqrt{\frac{k}{m}} \quad (21)$$

Each case has been analyzed over a range of reduced velocity,  $U_r = 4-12$ , over which the cylinder is predicted to have maximum amplitude of oscillation [24].  $U_r = 5$  has also been analyzed since the case corresponds to  $\eta = 1$  where one might expect resonance. The incoming flow velocity is fixed as 0.5 m/s to maintain the flow regime uniform at  $Re = 3.8 \times 10^4$ . The mass ratio, stiffness ratio, and other parameters for each case are summarized in Table 2. Stiffness coefficient of the cylinder has been non-dimensionalized to generalize the applicability of the analysis. Stiffness ratio is defined as

$$k^* = \frac{k}{mg/L} \quad (22)$$

**Table 2.** Reduced velocity, stiffness ratio, and frequency ratio at  $Re = 3.8 \times 10^4$ , for  $m^* = 0.66, 1.32,$  and  $1.98$ .

$U_r$	$k^*$	$\eta$
4	11.17	1.3
5	6.9	1.0
6	4.81	0.84
8	2.7	0.63
10	1.73	0.51
12	1.21	0.42

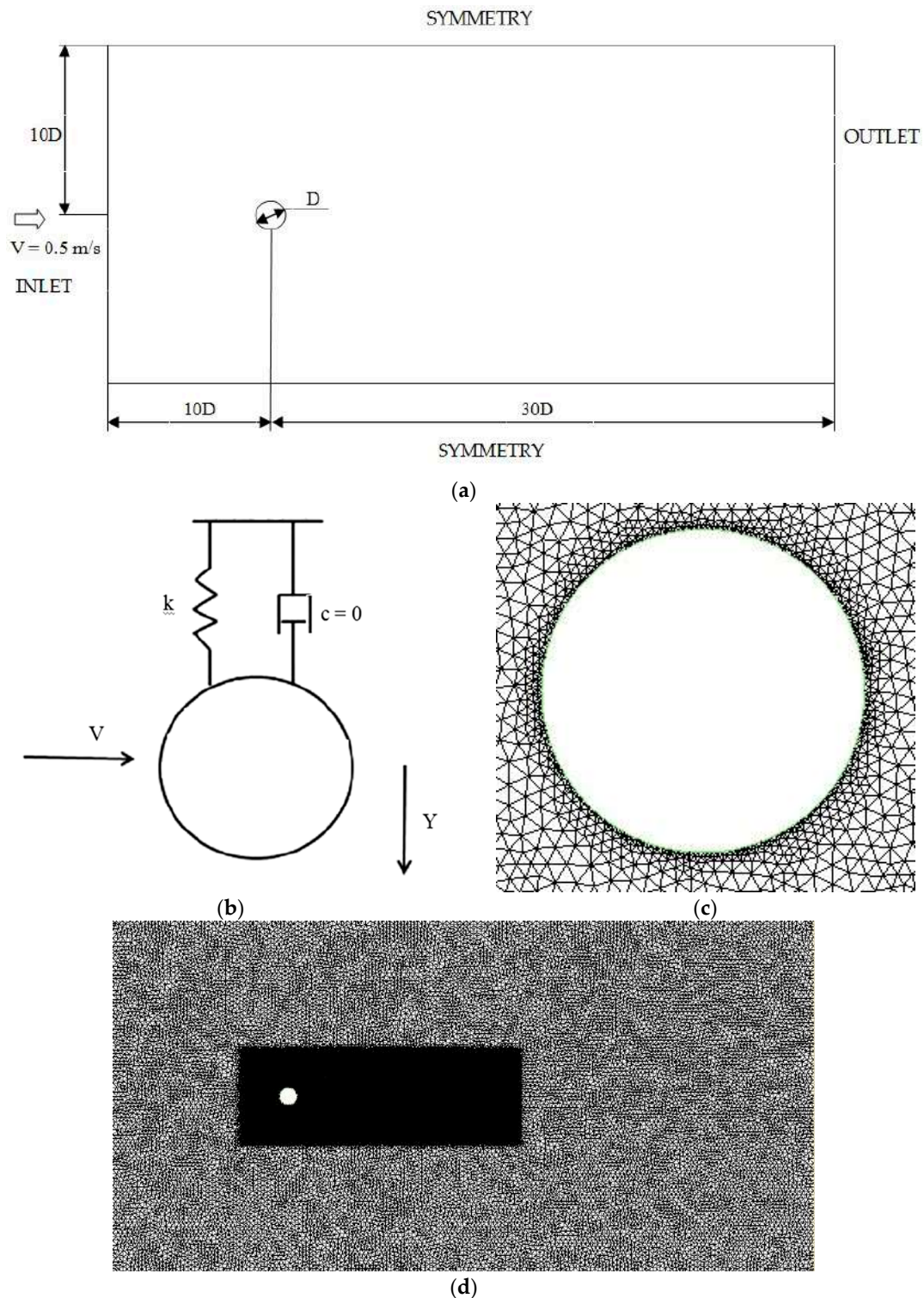


**Figure 3.** (a) Computational domain; (b) representation of elastically mounted cylinder model; (c) mesh around the cylinder; (d) computational mesh.

### 5.2. Fluid Domain and Boundary Conditions

Figure 3a shows the computational domain for the CFD simulation of VIV of an elastically mounted horizontal cylinder. The origin of the Cartesian coordinate system is located at the center of the cylinder. The length of the domain is  $40D$  with the cylinder located at  $10D$  away from the inlet boundary. The cross-flow width of the domain is  $20D$  with the center of the cylinder at the

middle. Detailed views of the mesh around the cylinder along with the computational domain after meshing have been shown in Figure 3c,d respectively. There are 307 nodes around the circumference of the cylinder and the minimum element size near the rigid wall boundary has been computed from boundary layer theory to be  $0.0001D$ . The non-dimensional element size represented as  $y^+$ , next to the cylinder surface is found to be less than unity. For the cylinder wall, a no slip boundary condition has been applied assuming the surface to be smooth. Inlet boundary has been treated as velocity-inlet with inflow velocity,  $V = 0.5$  m/s. Outlet boundary has been treated as pressure outlet, the gradients of fluid velocity are set to zero and the pressure with zero reference pressure. On the two transverse boundaries a symmetry boundary condition has been applied.

### 5.3. Mesh Independence Study

An unstructured 2D mesh has been used in the present CFD simulation to facilitate computationally economic platform for dynamic mesh simulation. The three dimensionality of the wake reduces as a result of the motion of the cylinder [16]. Hence it is possible to get a reasonably accurate result from a 2D analysis saving much computational cost and effort. The meshing strategy is that finer mesh is used in the vicinity of the moving cylinder with extra fine meshing in the boundary layer. Boundary layer thickness and the near wall element size have been calculated from boundary layer theory. The thickness of laminar sub-layer is obtained from Equation (23) [25]

$$\delta' = \frac{11.6\vartheta}{V^*} \quad (23)$$

where  $V^*$  is the frictional velocity given by

$$V^* = \sqrt{\frac{\tau_0}{\rho}} \quad (24)$$

and  $\tau_0$ , the wall shear stress is obtained as

$$\tau_0 = \frac{0.664}{\sqrt{Re_D}} \cdot \frac{\rho V^2}{2} \quad (25)$$

Increased mesh density has been adopted in the near cylinder and its wake in order to capture the physics of vortex shedding accurately. For ensuring that the results are independent of the grid size, a mesh independence study has been carried out. Three different grids have been used to simulate a specific case  $m^* = 2.45$  and  $U_r = 8$  and has been verified using results of experiments conducted at a towing tank facility in the Department of Ocean Engineering, Indian Institute of Technology Madras, India [10]. The details of the mesh independency study are given in Table 3. The last three grids give almost similar results and experiments, and [10] shows a 4.9% deviation from the present results. This can be assumed to be due to not accounting for damping in the present study. It can be concluded that the variation in the numerical results given by Meshes II, III, and IV are in the acceptable range and considering the computational economy Grid II with 49,995 nodes has been chosen for further analysis.

**Table 3.** Mesh independency study results

	$Re$	$m^*$	$U_r$	Nodes	$Y_{max}/D$
Grid I				35,487	1.241
Grid II	$3.8 \times 10^4$	2.45	8	49,995	1.220
Grid III				70,857	1.219
Grid IV				98,475	1.219
Narendran et al. (2015)				0.3–2.4 $\times 10^5$	2.45

While due steps like mesh independence studies have been carried out in this investigation, we acknowledge that the use of eddy-viscosity based turbulence models introduces a small amount of discrepancy in the final results. The errors of the  $k-\omega$ SST model in flow separation and wakes has been documented comprehensively in prior studies [26,27].

## 6. Results and Discussion

Numerical simulations have been carried out for three different mass ratios over reduced velocities ranging from 4 to 12. The cylinder is modeled to be having only single degree of freedom (SDOF) in the transverse or CF direction. Influence of  $m^*$  and  $k^*$  on both hydrodynamic force coefficient in the CF direction and the response of the cylinder have been studied in detail. The CF response results can be verified with experimental [17,28]. Time history of coefficient of lift,  $C_L$  and non-dimensional CF response  $Y/D$  over the range of  $U_r$  for  $m^* = 0.66, 1.32,$  and  $1.98$  are displayed in Figures 4–6 respectively.

### 6.1. Case I

Under Case I, the response of cylinder is studied for  $m^* = 0.66$ . The mass of the cylinder is taken as 3 kg and added mass coefficient  $C_A = 0.7$ .  $U_r$  is varied in the analysis by varying the coefficient of stiffness  $k$  and in turn the natural frequency  $f_n$  of the oscillating system. Details of the simulation parameters have been given in Table 2. For a stationary cylinder, it was observed from numerous experimental and numerical works [29–31] that  $C_L$  oscillates in a symmetrical fashion about zero due to vortex shedding [13]. In the present study for lower values of  $U_r$ ,  $C_L$  is not oscillating about zero symmetrically. However, the response of the cylinder is observed to be symmetrical for all values of  $U_r$  at  $m^* = 0.66$ . At  $U_r = 8$ ,  $C_L$  becomes almost symmetrical with an effective lift coefficient 0.18. Beat phenomenon is captured in the response of the cylinder at  $U_r = 8$ . Results for different cases are presented in Table 4. Maximum lift force is observed at  $U_r = 4$  with  $C_L = 1.12$  and maximum response at  $U_r = 8$  with  $Y/D = 1.26$ . With increase in  $U_r$  response amplitude of the cylinder decreases beyond  $U_r = 8$ . Time histories of  $C_L$  and  $Y/D$  for  $m^* = 0.66$  is presented in Figure 4.

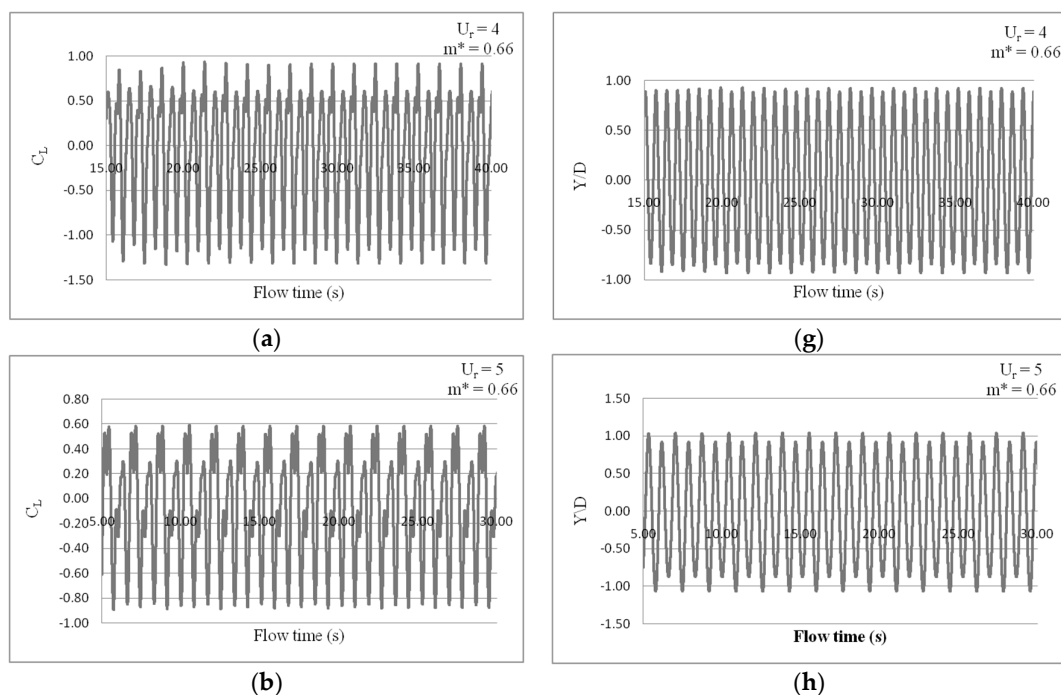
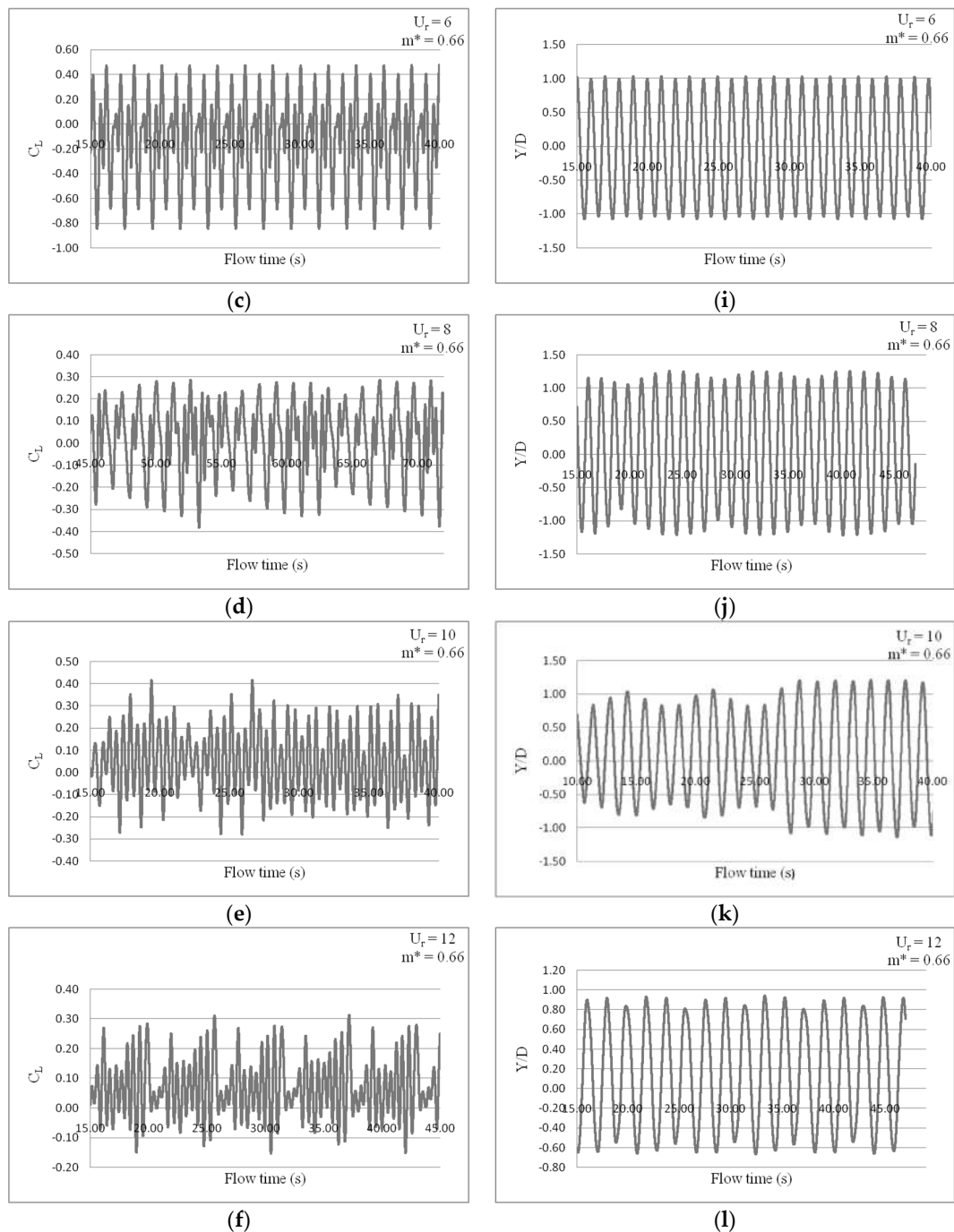


Figure 4. Cont.



**Figure 4.** Time histories of hydrodynamic and structural response parameters at  $m^* = 0.66$ : (a)  $C_L$  for  $U_r = 4$ ; (b)  $C_L$  for  $U_r = 5$ ; (c)  $C_L$  for  $U_r = 6$ ; (d)  $C_L$  for  $U_r = 8$ ; (e)  $C_L$  for  $U_r = 10$ ; (f)  $C_L$  for  $U_r = 12$ ; (g)  $Y/D$  for  $U_r = 4$ ; (h)  $Y/D$  for  $U_r = 5$ ; (i)  $Y/D$  for  $U_r = 6$ ; (j)  $Y/D$  for  $U_r = 8$ ; (k)  $Y/D$  for  $U_r = 10$ ; (l)  $Y/D$  for  $U_r = 12$ .

## 6.2. Case II

Under Case II, the response of cylinder is studied for  $m^* = 1.32$ . Mass of the cylinder is taken as 6 kg and added mass coefficient  $C_A = 0.7$ . Time histories of  $C_L$  and  $Y/D$  for  $m^* = 1.32$  is presented in Figure 5. At  $m^* = 1.32$ , the cylinder exhibits similar response characteristics as in the previous case with maximum response at  $U_r = 8$  with  $Y/D = 1.17$ . As the mass ratio increases, a slight decrease in the cross flow response amplitude is observed. Unlike the previous case, beat phenomenon is observed at  $U_r = 10$ .

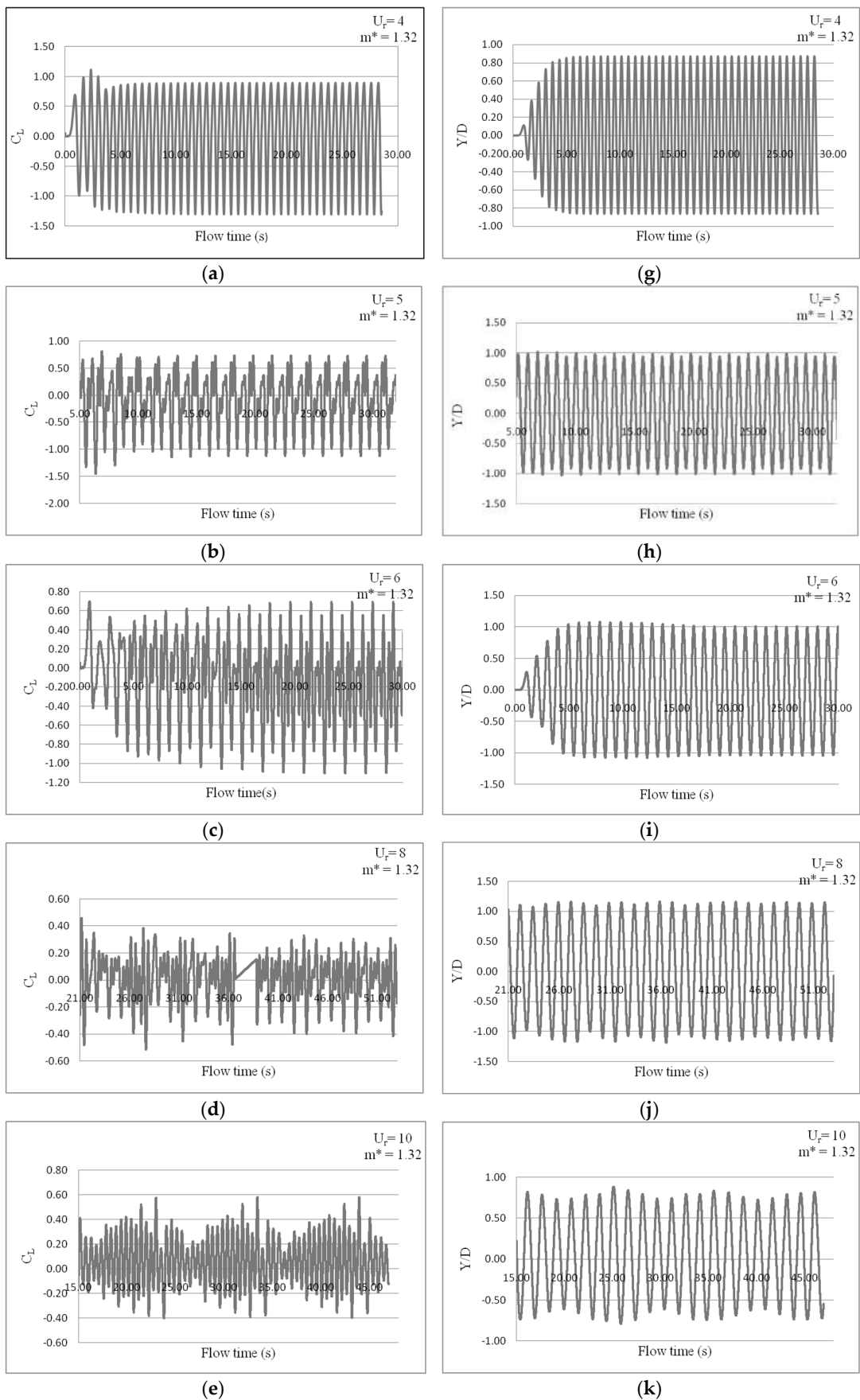
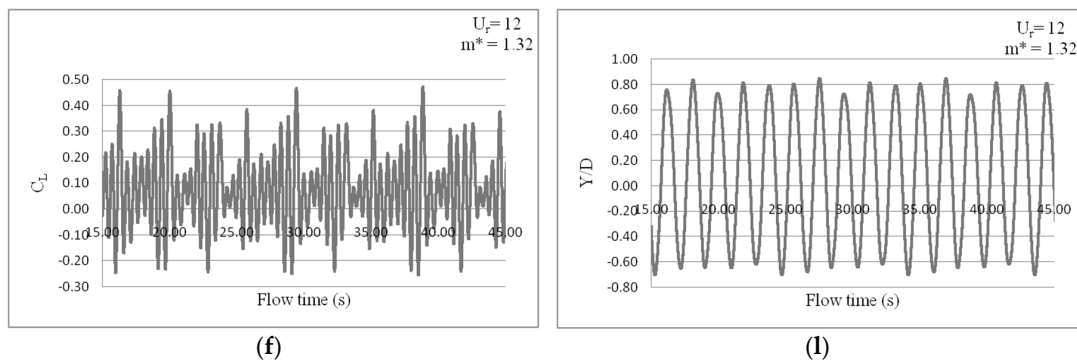


Figure 5. Cont.



**Figure 5.** Time histories of hydrodynamic and structural response parameters at  $m^* = 1.32$ : (a)  $C_L$  for  $U_r = 4$ ; (b)  $C_L$  for  $U_r = 5$ ; (c)  $C_L$  for  $U_r = 6$ ; (d)  $C_L$  for  $U_r = 8$ ; (e)  $C_L$  for  $U_r = 10$ ; (f)  $C_L$  for  $U_r = 12$ ; (g)  $Y/D$  for  $U_r = 4$ ; (h)  $Y/D$  for  $U_r = 5$ ; (i)  $Y/D$  for  $U_r = 6$ ; (j)  $Y/D$  for  $U_r = 8$ ; (k)  $Y/D$  for  $U_r = 10$ ; (l)  $Y/D$  for  $U_r = 12$ .

### 6.3. Case III

Under Case III, the response of cylinder is studied for  $m^* = 1.98$ . The mass of the cylinder is taken as 9 kg and added mass coefficient  $C_A = 0.7$ . Time histories of  $C_L$  and  $Y/D$  for  $m^* = 1.98$  is presented in Figure 6. Maximum amplitude is observed at  $U_r = 8$  with  $Y/D = 1.13$  which is slightly less than the previous two cases. Here also prominent beat is observed at  $U_r = 10$ .

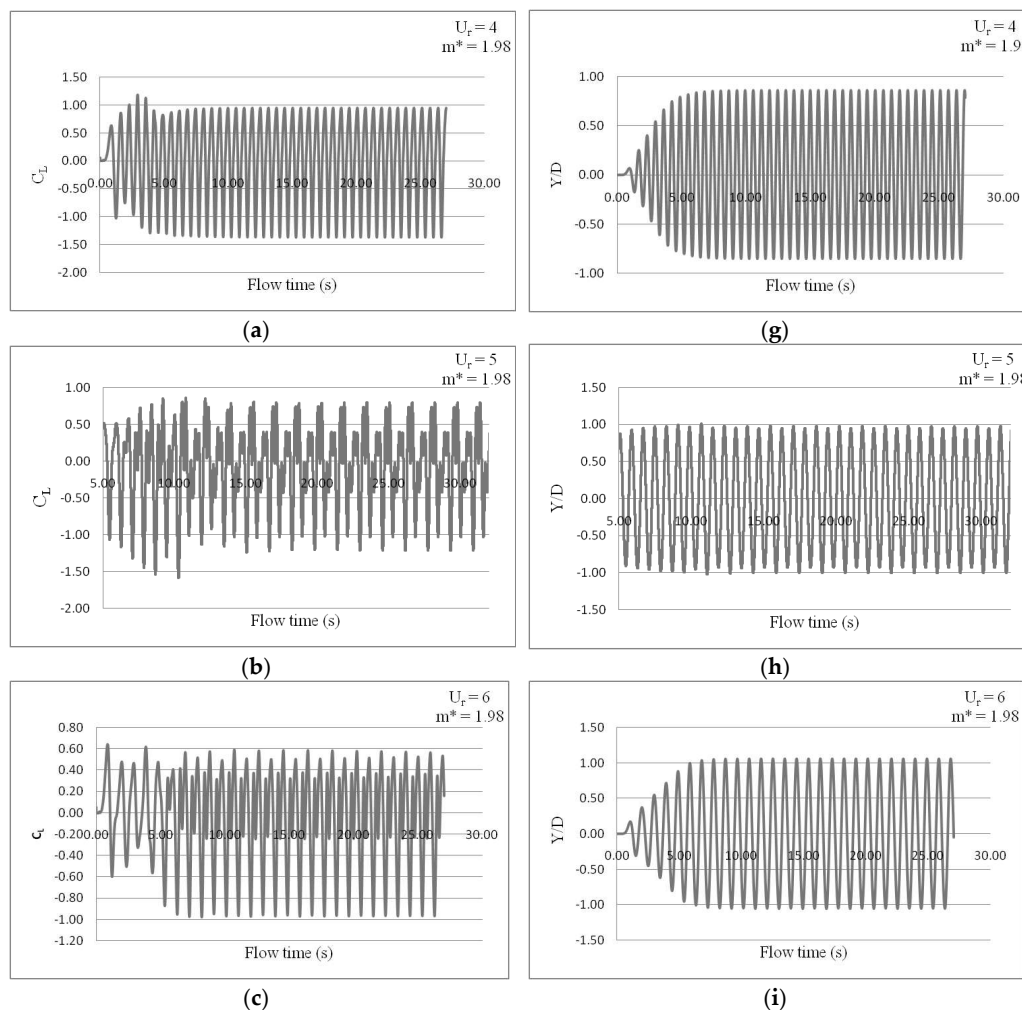


**Figure 6.** Cont.

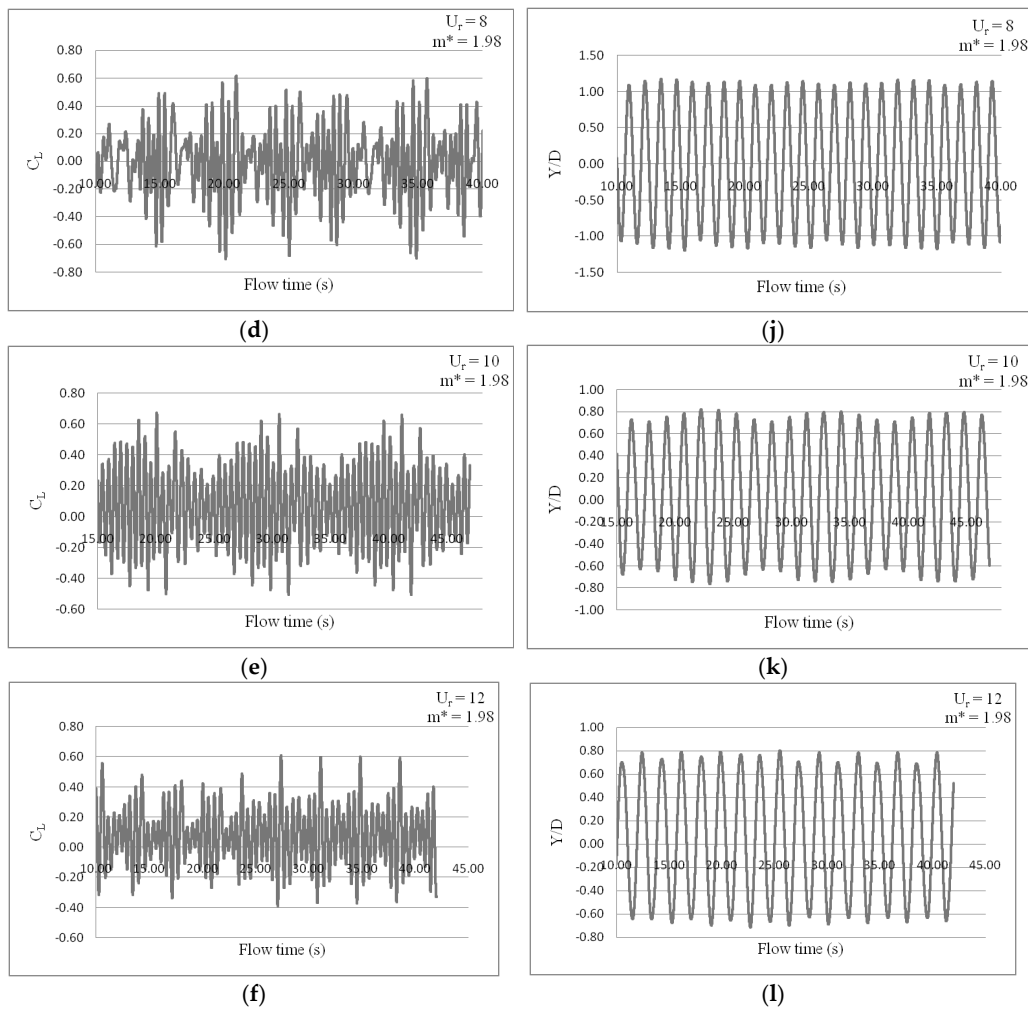


**Figure 6.** Time histories of hydrodynamic and structural response parameters at  $m^* = 1.98$ : (a)  $C_L$  for  $U_r = 4$ ; (b)  $C_L$  for  $U_r = 5$ ; (c)  $C_L$  for  $U_r = 6$ ; (d)  $C_L$  for  $U_r = 8$ ; (e)  $C_L$  for  $U_r = 10$ ; (f)  $C_L$  for  $U_r = 12$ ; (g)  $Y/D$  for  $U_r = 4$ ; (h)  $Y/D$  for  $U_r = 5$ ; (i)  $Y/D$  for  $U_r = 6$ ; (j)  $Y/D$  for  $U_r = 8$ ; (k)  $Y/D$  for  $U_r = 10$ ; (l)  $Y/D$  for  $U_r = 12$ .

6.4. Shedding Characteristics

Numerical simulations for each case show that the shedding pattern and the characteristic variation of  $C_L$  strongly depend on the natural frequency of the oscillating mass. A more detailed history of  $C_L$  and  $Y/D$  for  $m^* = 0.66, 1.32,$  and  $1.98$  are presented in Figures 7–9 respectively.

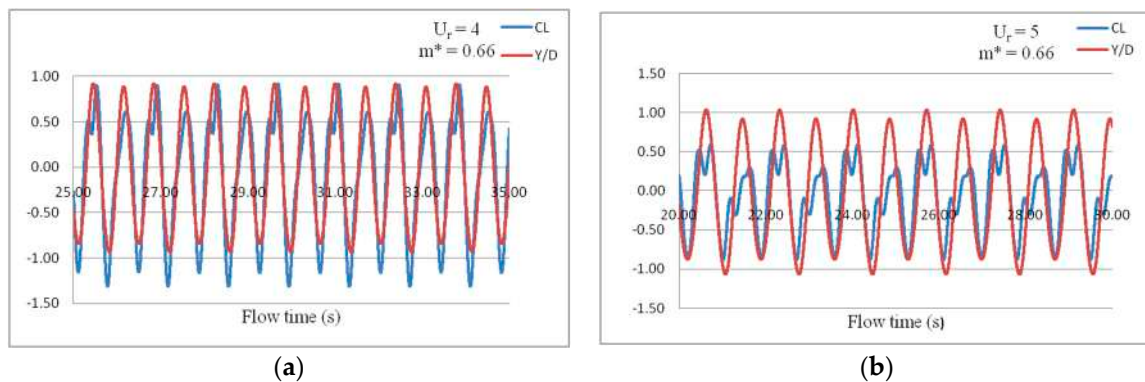


**Figure 7.** Cont.



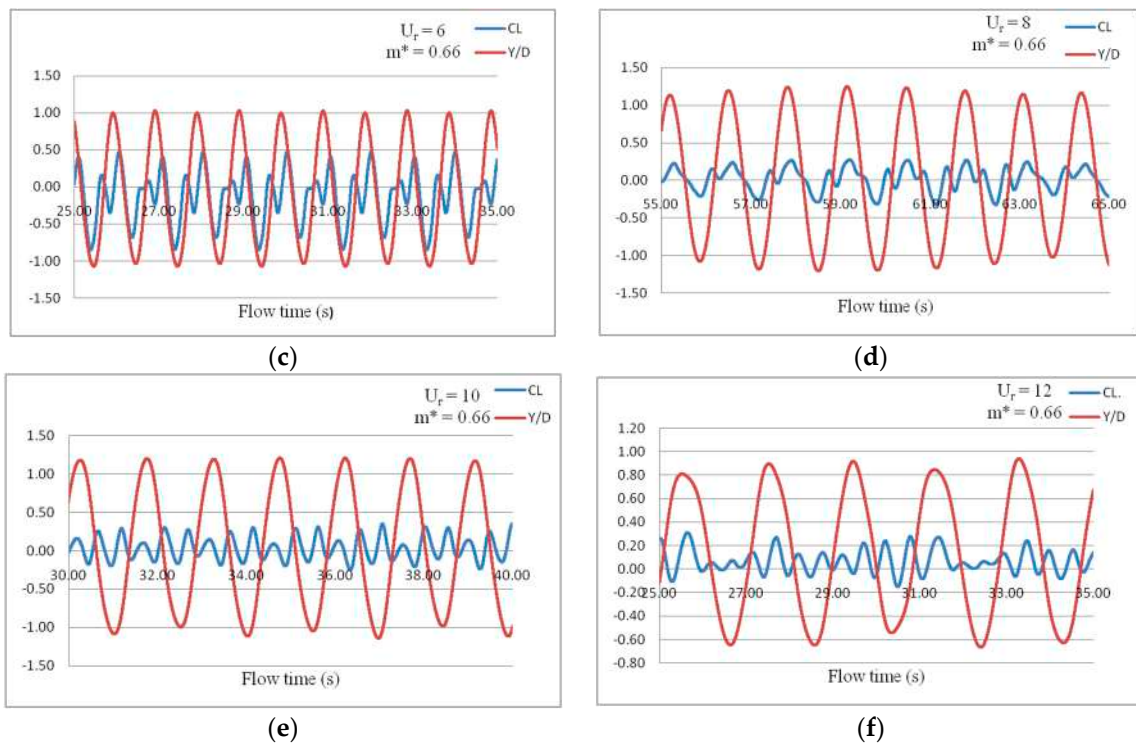


**Figure 7.** Variation of  $C_L$  with  $Y/D$  for  $m^* = 0.66$  (a)  $U_r = 4$ ; (b)  $U_r = 5$ ; (c)  $U_r = 6$ ; (d)  $U_r = 8$ ; (e)  $U_r = 10$ ; (f)  $U_r = 12$ .

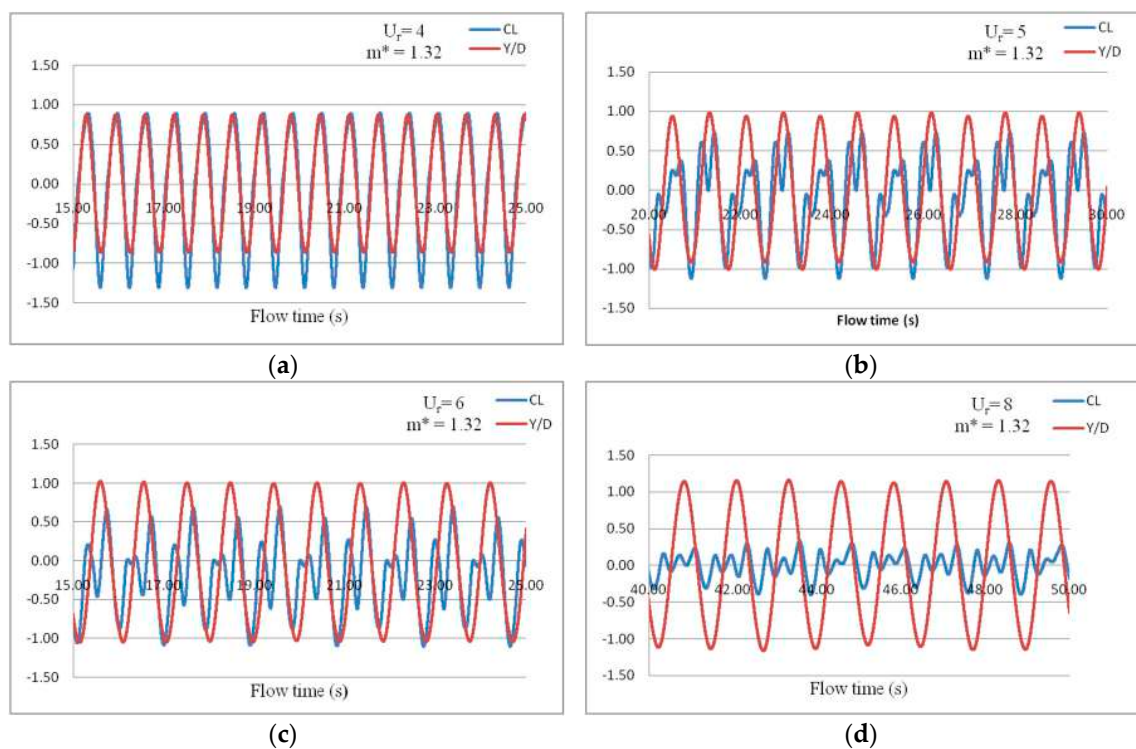


**Figure 8.** Cont.

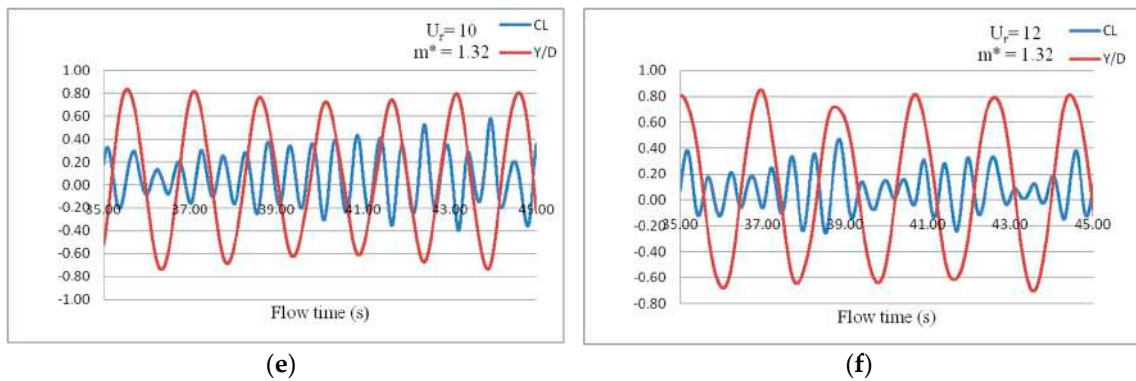


**Figure 8.** Variation of  $C_L$  with  $Y/D$  for  $m^* = 1.32$ : (a)  $U_r = 4$ ; (b)  $U_r = 5$ ; (c)  $U_r = 6$ ; (d)  $U_r = 8$ ; (e)  $U_r = 10$ ; (f)  $U_r = 12$ .

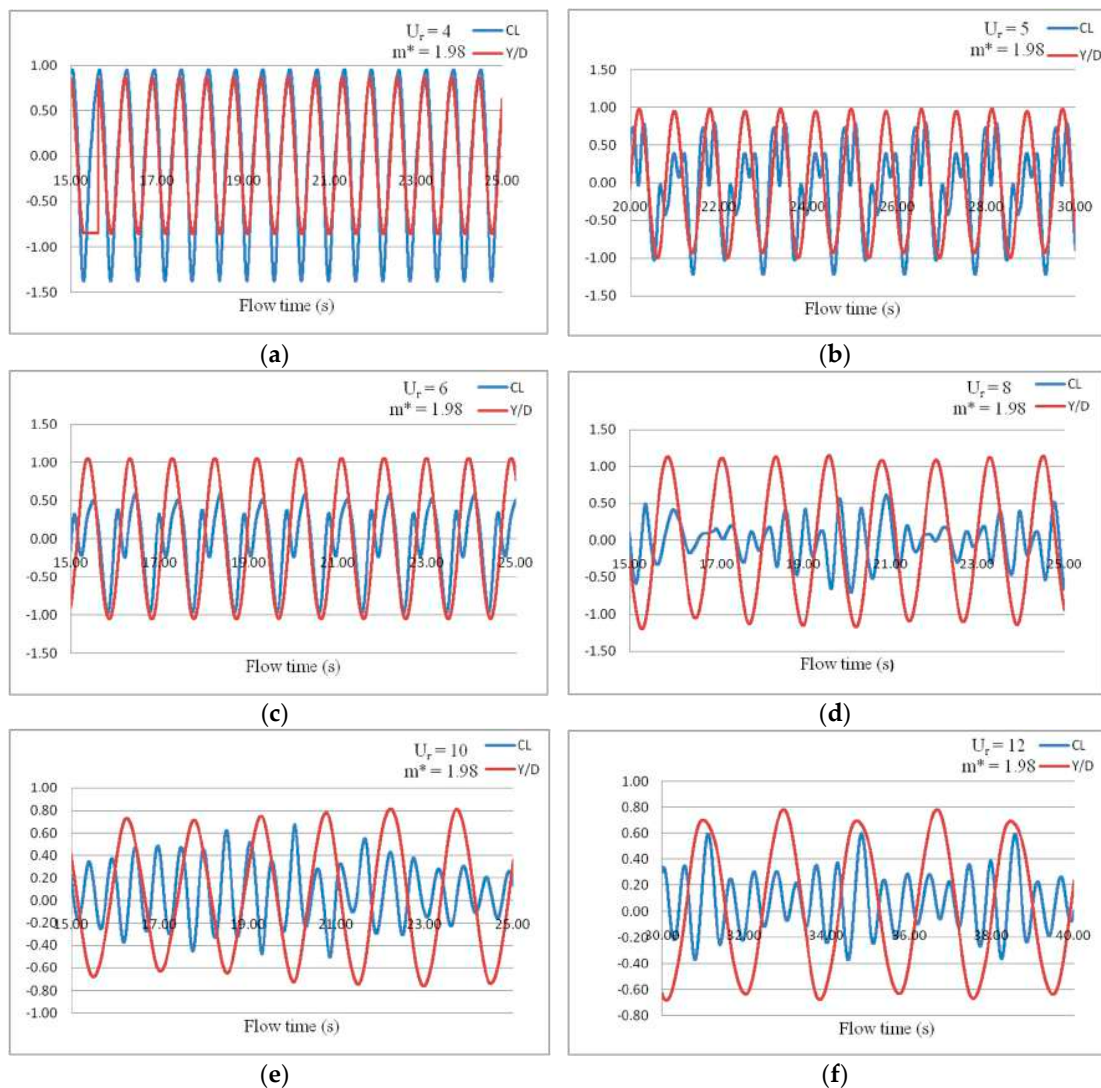


**Figure 9.** Variation of  $C_L$  with  $Y/D$  for  $m^* = 1.98$ : (a)  $U_r = 4$ ; (b)  $U_r = 5$ ; (c)  $U_r = 6$ ; (d)  $U_r = 8$ ; (e)  $U_r = 10$ ; (f)  $U_r = 12$ .

From a detailed analysis of amplitude of variation of lift coefficient, it is observed that the characteristics of hydrodynamic load causing the cylinder to oscillate varies with  $U_r$  and in turn with frequency ratio,  $\eta$ . For all the three cases, a similarity can be observed in the shedding characteristics which are reflected in the pattern of lift coefficient variation. In each case, a single oscillation of the

cylinder is actuated by a single oscillation of lift force when  $U_r = 4$ . For  $U_r = 6$ , double oscillation of lift coefficient is observed for each oscillation of  $Y/D$ . The first oscillation is of relatively low amplitude and the second one of larger amplitude.  $U_r = 8$  and 10 which is more prone to beating phenomenon displays three separate  $C_L$  oscillations for each oscillation of the cylinder.  $U_r = 12$  is observed to have an additional half oscillation. For all mass ratios, a 2P mode of vortex shedding is observed in the range of  $U_r = 4$ –12 which corresponds to synchronization.

A single beat sustains for a time period of 10.53 and 10.42 seconds for  $m^* = 1.98$  and 1.32, respectively. Differently for  $m^* = 0.66$ , single beat sustains at  $U_r = 8$  for 7.84 s which is significantly lesser than the other two cases, showing the highest value of cross flow response amplitude. Also, at the lowest mass ratio,  $m^* = 0.66$ , it is observed from the response amplitude history that the cylinder initially shows a tendency to beat at  $U_r = 10$  with a significantly larger response amplitude with  $Y/D = 1.08$  compared to 0.82 and 0.80 for  $m^* = 1.32$  and 1.98 respectively at same  $U_r$ . Further study on the influencing parameters led to a trend showing a relationship between  $m^*$  and  $U_r$ , through which they have proved that the range of reduced velocity over which cylinder under VIV shows maximum cross flow response widens as  $m^*$  decreases [10]. The relationship put forward by [14] is shown in Figure 11. Results of the present study also show that  $Y/D$  increases with decreasing mass ratio and the range of  $U_r$  over which the maximum amplitude of response to be expected widens.

The effect of  $U_r$  on various simulation parameters is illustrated in Figure 10. A comparison of various hydrodynamic and structural parameters at different  $k^*$  values for each case is given in Figure 11a,b. Present simulation results matches well with the values represented in Figure 11b. In all cases maximum response occurs at  $U_r = 8$ . Even though the response amplitude is high in the range  $U_r = 4$ –12, as it deviates away from  $U_r = 8$ , amplitude decreases. A similar result was reported by [19] is represented in the modified Griffin's plot.

The numerical simulation could successfully reproduce the response behavior depicted by the lower branch of response. Figure 11b shows the response of a cylinder of mass ratio  $m^* = 2.4$  which is comparable with the present study.

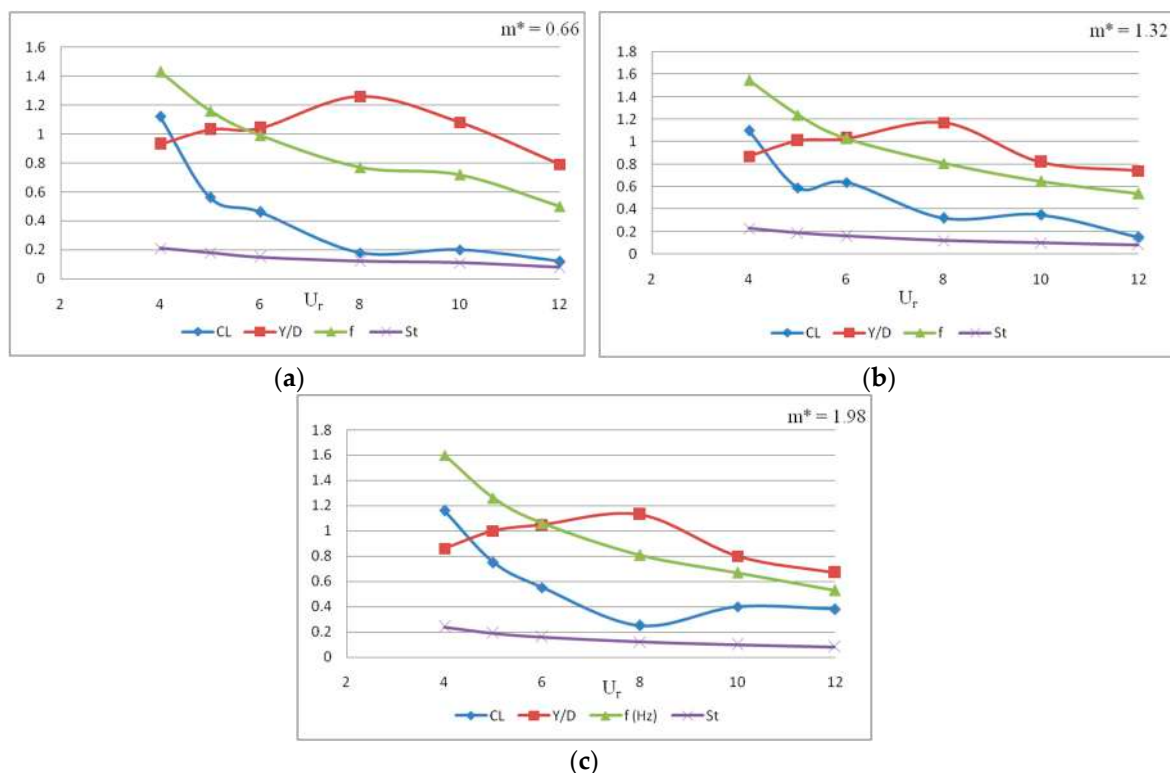


**Figure 10.** Effect of  $U_r$  on various hydrodynamic and structural parameters for VIV of a cylinder (a)  $m^* = 0.66$ ; (b)  $m^* = 1.32$ ; (c)  $m^* = 1.98$ .

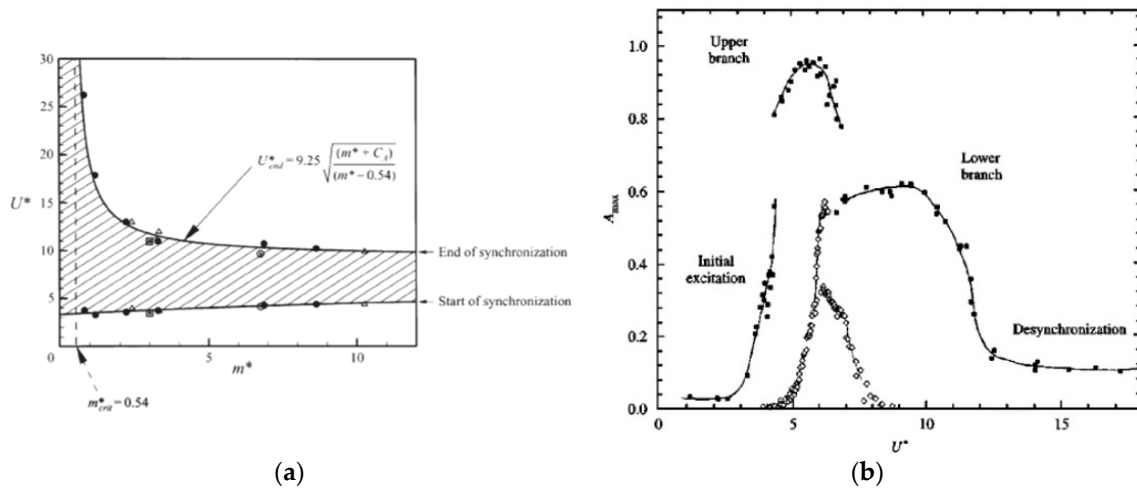


**Figure 11.** (a) Relationship between  $U_r$  and  $m^*$  presented by Williamson and Govardhan [23]; (b) maximum response amplitudes  $A_{max}$  as functions of the reduced velocity  $U_r$  for  $m^* = 2.4$  and  $m^* = 248$  [19].

It was previously observed that 2P mode shedding is the reason for synchronized response [20]. Since detailed analysis of physics of the flow is not in the scope of this paper, shedding pattern is not further discussed. A representation of 2P mode of vortex shedding in the synchronization range of  $U_r$  is shown in Figure 12. A detailed study to analyze this phenomenon is pending. Shedding characteristics at different  $m^*$  and  $k$  are listed in Table 4.

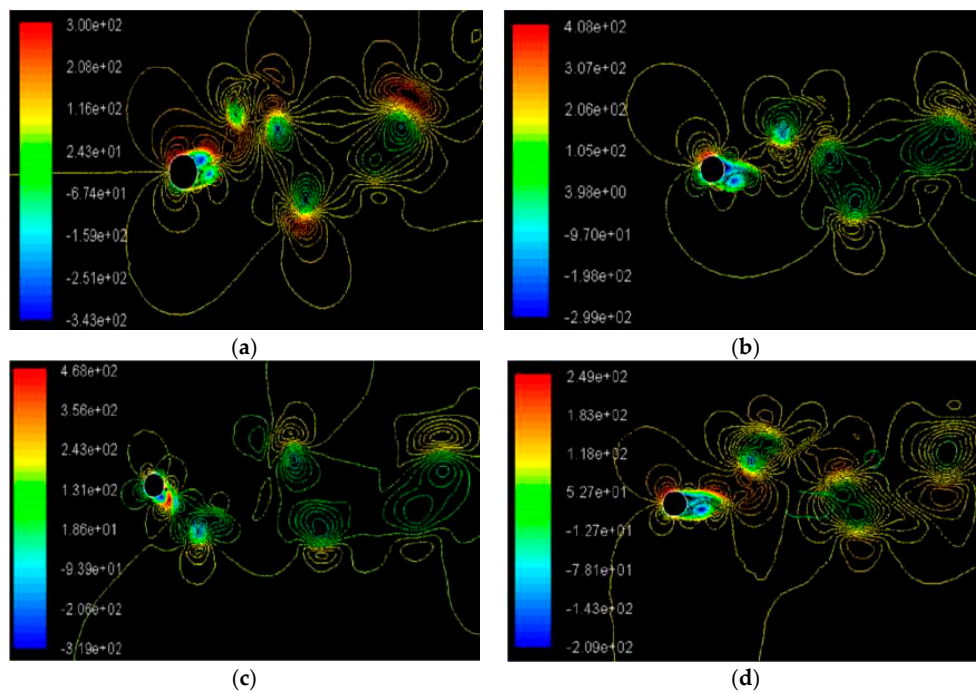


**Figure 12.** Cont.

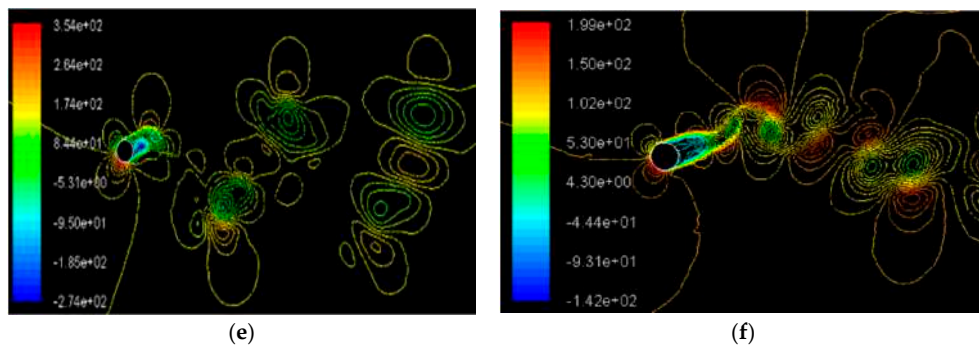


**Figure 12.** Representation of pressure (N/m<sup>2</sup>) contours in 2P mode of vortex shedding for  $m^* = 0.66$  (a)  $U_r = 4$ ; (b)  $U_r = 5$ ; (c)  $U_r = 6$ ; (d)  $U_r = 8$ ; (e)  $U_r = 10$ ; (f)  $U_r = 12$ .

**Table 4.** Hydrodynamic and structural response characteristics for  $m^* = 0.66, 1.32,$  and  $1.98$ .

Mass Ratio, $m^*$	$U_r$	$C_L$	$Y/D$	$f_v$ (Hz)	$\eta$	$St$	Shedding Characteristics
$m^* = 1.98$	4	1.16	0.86	1.6	1.04	0.24	2P Lift force oscillates about zero value once during one time period of oscillation of the cylinder.
	5	0.75	1.0	1.26	1.04	0.19	2P Lift force oscillates twice during one time period of oscillation of the cylinder.
	6	0.55	1.05	1.06	1.03	0.16	2P Lift force oscillates twice during one time period of oscillation of the cylinder.
	8	0.25	1.13	0.81	1.01	0.12	2P Lift force oscillates thrice during one time period of oscillation of the cylinder.
	10	0.4	0.8	0.67	0.98	0.1	2P Lift force oscillates thrice during one time period of oscillation of the cylinder. Beat phenomenon is observed with time period 10.53 s.
	12	0.38	0.67	0.53	1.04	0.08	2P Lift force oscillates 3.5 times during one time period of oscillation of the cylinder.
$m^* = 1.32$	4	1.1	0.87	1.55	1.07	0.23	2P Lift force oscillates about zero value once during one time period of oscillation of the cylinder.
	5	0.59	1.01	1.24	1.06	0.19	2P Lift force oscillates twice during one time period of oscillation of the cylinder.
	6	0.64	1.03	1.03	1.06	0.16	2P Lift force oscillates twice during one time period of oscillation of the cylinder.
	8	0.32	1.17	0.81	1.01	0.12	2P Lift force oscillates thrice during one time period of oscillation of the cylinder.
	10	0.35	0.82	0.65	1.02	0.1	2P Lift force oscillates thrice during one time period of oscillation of the cylinder. Beat phenomenon is observed with time period 10.42 s.
	12	0.15	0.74	0.54	1.01	0.082	2P Lift force oscillates 3.5 times during one time period of oscillation of the cylinder.
$m^* = 0.66$	4	1.12	0.93	1.43	1.14	0.21	2P Lift force oscillates about zero value once during one time period of oscillation of the cylinder.
	5	0.56	1.03	1.16	1.13	0.18	2P Lift force oscillates twice during one time period of oscillation of the cylinder.
	6	0.46	1.04	0.99	1.10	0.15	2P Lift force oscillates twice during one time period of oscillation of the cylinder.
	8	0.18	1.26	0.77	1.06	0.12	2P Lift force oscillates thrice during one time period of oscillation of the cylinder. Beat phenomenon is observed with time period 7.84 s.
	10	0.2	1.08	0.72	1.1	0.11	2P Lift force oscillates thrice during one time period of oscillation of the cylinder. No beat is observed.
	12	0.12	0.79	0.5	1.1	0.08	2P Lift force oscillates 3.5 times during one time period of oscillation of the cylinder.

Energy possessed by a spring mass system undergoing oscillation can be represented as the sum of its kinetic and potential energies as given by Equation (26).

$$E = \frac{1}{2}m\dot{Y}^2 + \frac{1}{2}kY^2 \quad (26)$$

When the position of the mass corresponds to maximum amplitude, the entire kinetic energy of the system will be converted into potential energy and Equation (26) reduces to

$$E = \frac{1}{2}kY^2 \quad (27)$$

At zero amplitude position of the mass, the entire potential energy is converted into kinetic energy. Since the total energy of the system is conserved energy balance can be written as Equation (28).

$$E = \frac{1}{2}kY^2 = \frac{1}{2}m\dot{Y}^2 \quad (28)$$

Hence the maximum possible velocity with which the system oscillates can be expressed as

$$\dot{Y} = \sqrt{\frac{k}{m}}Y \quad (29)$$

Which may be also represented in non-dimensional form represented by Equation (30)

$$\dot{Y} = \sqrt{\frac{Dk^*g}{L/D}} \frac{Y}{D} \quad (30)$$

For the optimum condition proven numerically,  $V_{max}$  is obtained as 0.5 m/s. Power associated with the oscillatory motion can be expressed by Equation (31)

Maximum velocity has been calculated using the above expression and a comparison of average power output estimated is represented in Table 5. Even though the maximum amplitude of oscillation is obtained for each  $m^*$  at  $U_r = 8$ , power output is maximum at  $U_r = 4$ , suggesting the best operating conditions.

$$P_{avg} = F_L \dot{Y} = C_L \frac{1}{2} \rho AV^2 \dot{Y} \quad (31)$$

**Table 5.** Cylinder velocity and calculated average power for different configurations.

$Re$	$m^*$	$U_r$	$k^*$	$C_L$	$Y/D$	$\dot{Y}$	$P_{avg}$ (W)
$3.8 \times 10^4$	0.66	4	11.17	1.12	0.93	0.74	7.90
		5	6.9	0.56	1.03	0.65	3.44
		6	4.81	0.46	1.04	0.54	2.38
		8	2.7	0.18	1.26	0.49	0.85
		10	1.73	0.2	1.08	0.34	0.64
		12	1.21	0.12	0.79	0.21	0.24
	1.32	4	11.17	1.1	0.87	0.69	7.26
		5	6.9	0.59	1.01	0.63	3.55
		6	4.81	0.64	1.03	0.54	3.28
		8	2.7	0.32	1.17	0.46	1.40
		10	1.73	0.35	0.82	0.26	0.86
		12	1.21	0.15	0.74	0.19	0.28
	1.98	4	11.17	1.16	0.86	0.69	7.57
		5	6.9	0.75	1	0.63	4.47
		6	4.81	0.55	1.05	0.55	2.87
		8	2.7	0.25	1.13	0.44	1.05
		10	1.73	0.4	0.8	0.25	0.95
		12	1.21	0.38	0.67	0.18	0.64

## 7. Field Test Validation of Numerical Results

The HVPG module with specifications as given in Table 1 has been used for a field test in the Palissery irrigation canal. The flow velocity in the canal was measured to be 0.5 m/s. The model has been tested for different  $k^*$  values. Cylinder displacement was measured by attaching a pantograph to the side vanes. As the cylinder oscillates, the marking pencil attached to the spring side of the module marks its impression on the paper attached on the vane side. The results are tabulated in Table 6.  $U_r = 4, 8,$  and  $12,$  but the effect of  $k^*$  is observed to follow the same trend as predicted numerically. An average deviation of 30% is observed between numerical method and field tests. Over prediction of the response amplitude by the numerical method may be attributed to not accounting for structural damping. Also, friction in the sliding parts of the guide vane contributes to lowering the response. Components of the HVPG and field test set up are shown in Figure 13.

**Table 6.** Results of field test conducted at Palissery irrigation canal.

$Re$	$m^*$	$U_r$	$k^*$	$Y_{field}$ (cm)	$Y/D_{field}$	$Y/D_{numerical}$
$3.8 \times 10^4$	0.66	4	11.17	5.5	0.72	0.93
		8	2.7	7.5	0.98	1.26
		12	1.21	4.5	0.59	0.79



**Figure 13.** (a) Model of HVPG; (b) field test at Palissery irrigation canal for  $m^* = 0.66$  and  $U_r = 4, 8,$  and  $12.$

## 8. Conclusions

Extensive research carried out to understand and interpret the intrinsic vortex shedding phenomenon has brought out several correlations to estimate response amplitude  $Y/D$  [32], but most of these expressions define the non-dimensional oscillation amplitude  $Y/D$  as a function of complex parameters like the Skop–Griffin parameter [14]. The present study is an effort to understand the hydrodynamic response of the cylinder from a designers' perspective by considering the effect of tangible system parameters only. Optimum response is obtained at  $m^* = 0.66$  and  $U_r = 8,$  but optimum estimated power output for the same mass ratio is obtained at  $U_r = 4.$  It is observed that maximum power output can be derived from an HVPG operating at low mass ratio and in the lowest regime of reduced velocity in the synchronization range irrespective of amplitude of cylinder response. The reduced power output at  $U_r = 8$  is due to the lower value of  $C_L$  which in turn is due to several oscillations of lift force within one time period of oscillation of the cylinder. The true values of frequency ratio,  $\eta$  obtained from the simulations are indicative of synchronized response for the range of  $U_r$  considered. Hence it is observed that the developed numerical method could successfully simulate the flow around an oscillating cylinder. The numerical method developed is capable of predicting the trend of variation of  $Y/D$  which is verified using the results of field test. At  $m^* = 0.66$  where maximum response is observed,  $\eta$  significantly exceeds over unity compared to the higher mass ratio cases. It can

be concluded that maximum amplitude of response is observed at mass ratios corresponding to  $\eta$  values greater than unity rather than at unity  $\eta$  values. Even though hydrodynamic lift force acting on the cylinder is proportional to the incoming flow velocity,  $C_L$  strongly depends on the natural frequency of the oscillating system and the shedding pattern. Response amplitude of the cylinder also depends on stiffness ratio  $k^*$  and in turn on natural frequency of the oscillating system  $f_n$ . Response amplitude increases with decreasing mass ratio and the range of  $U_r$  over which the response is high (resonance) widens. Occurrence of beat phenomenon also depends on  $m^*$  and  $k^*$  and the relationship is more pronounced at lower values of  $m^*$ . The mode of vortex shedding depends only on  $U_r$  at a constant flow velocity and is independent of  $m^*$ . On the whole, the work provides strong design inputs to the construction of the envisaged HVPG model.

## 9. Scope for Future Research

The discussions and conclusions from Sections 7 and 8 respectively indicate an immense scope for future research. Authors are in the process of improving the present design by incorporating structural damping in the studies. Inclusion of a greater number of rollers in the guide vanes is also being aimed at for eliminating the friction between sliding parts. The influence of these additional parameters in the equation of motion can reduce the errors in the subsequent numerical prediction, leading the design parameters closer to those of practical values. Improvised designs are also being devised for minimizing the transmission losses during power generation.

**Author Contributions:** Conceptualization, V.C., S.M., and S.J.; Data curation, V.C. and S.J.; Formal analysis, V.C. and S.J.; Funding acquisition, S.J. and V.M.; Investigation, V.C.; Methodology, S.M. and S.J.; Project administration, S.M. and S.J.; Resources, S.J. and V.M.; Software, V.M.; Supervision, S.M. and S.J.; Validation, V.C. and S.J.; Visualization, V.C. and S.J.; Writing—original draft, V.C. and S.J.; Writing—review & editing, V.C., S.J., and V.M.

**Funding:** This research was partially funded by Energy Management Center, Government of Kerala, India specifically for the development of Hydro Vortex Power Generator module with grant no. EMC/ET&R/18/R&D/SCMS/01.

**Acknowledgments:** The authors would like to thank the management and principal of SCMS School of Engineering and Technology for all the support offered for the research and development. The authors would also like to thank Energy Management Center, Government of Kerala for all the support.

**Conflicts of Interest:** The authors declare no conflict of interest.

## References

- Gerrard, J.H. The mechanics of the formation region of vortices behind bluff bodies. *J. Fluid Mech.* **1966**, *25*, 401–413. [[CrossRef](#)]
- Gao, Y.; Fu, S.; Xiong, Y.; Zhao, Y.; Liu, L. Experimental study on response performance of vortex-induced vibration on a flexible cylinder. *Ships Offshore Struct.* **2016**, *12*, 116–134. [[CrossRef](#)]
- Bimbato, A.M.; Pereira, L.A.; Hirata, M.H. Suppression of vortex shedding on a bluff body. *J. Wind Eng. Ind. Aerodyn.* **2013**, *122*, 16–18. [[CrossRef](#)]
- Bernitsas, M.; Raghavan, K.; Ben-Simon, Y.; Garcia, E. VIVACE (Vortex Induced Vibration Aquatic Clean Energy): A New Concept in Generation of Clean and Renewable Energy from Fluid Flow. *J. Offshore Mech. Arct. Eng.* **2006**, *130*, 041101. [[CrossRef](#)]
- An, X.; Song, B.; Tian, W.; Ma, C. Design and CFD Simulations of a Vortex-Induced Piezoelectric Energy Converter (VIPEC) for Underwater Environment. *Energies* **2018**, *11*, 330. [[CrossRef](#)]
- Janardhanan, S.; Chandran, V.; Varghese, C.; Achuth, D.; Devassy, D.; Mathews, D.C. Hydro vortex power generator design and construction. In Proceedings of the Kerala Technological CONGRESS, KETCON 2018—Human Computer Interface, Thrissur, India, 24 February 2018.
- Griffin, O.M. Vortex-Excited Cross-Flow Vibrations of a Single Cylindrical Tube. *ASME J. Press. Vessel Technol.* **1980**, *102*, 158–166. [[CrossRef](#)]
- Khalak, A.; Williamson, C.H.K. Dynamics of a hydroelastic cylinder with very low mass and damping. *J. Fluids Struct.* **1996**, *10*, 455–472. [[CrossRef](#)]



9. Narendran, K.; Murali, K.; Sundar, V. Vortex-induced vibrations of elastically mounted circular cylinder at Re of the O(105). *J. Fluids Struct.* **2015**, *54*, 503–521. [[CrossRef](#)]
10. Govardhan, R.; Williamson, C.H.K. Defining the ‘modified Griffin plot’ in vortex-induced vibration: Revealing the effect of Reynolds number using controlled damping. *J. Fluid Mech.* **2006**, *561*, 147–180. [[CrossRef](#)]
11. Bernitsas, M. Out of the Vortex. *Mech. Eng.* **2010**, *132*, 22–27. [[CrossRef](#)]
12. Tian, W.; Mao, Z.; Zhao, F. Design and Numerical Simulations of a Flow Induced Vibration Energy Converter for Underwater Mooring Platforms. *Energies* **2017**, *10*, 1427. [[CrossRef](#)]
13. Khan, N.B.; Ibrahim, Z.; Tuan, L.; Javed, M.F.; Jameel, M. Numerical investigation of the vortex-induced vibration of an elastically mounted circular cylinder at high Reynolds number ( $Re = 104$ ) and low mass ratio using the RANS code. *PLoS ONE* **2017**, *12*, e0185832. [[CrossRef](#)] [[PubMed](#)]
14. Williamson, C.H.K.; Govardhan, R. Vortex induced vibrations. *Annu. Rev. Fluid Mech.* **2004**, *36*, 413–455. [[CrossRef](#)]
15. Achenbach, E.; Heinecke, E. On Vortex Shedding from Smooth and Rough Cylinders in the Range of Reynolds Numbers  $6 \times 10^3$  to  $5 \times 10^6$ . *J. Fluid Mech.* **1981**, *109*, 239–251. [[CrossRef](#)]
16. Blevins, R.D. *Flow-Induced Vibration*, 2nd ed.; Van Nostrand Reinhold: New York, NY, USA, 1990; pp. 163–164, ISBN 1-57524-183-8.
17. Gabbai, R.D.; Benaroya, H. An overview of modeling and experiments of vortex-induced vibration of circular cylinders. *J. Sound Vib.* **2005**, *282*, 575–616. [[CrossRef](#)]
18. Anagnostopoulos, P.W.; Bearman, P.W. Response characteristics of a vortex excited cylinder at low Reynolds number. *J. Fluids Struct.* **1992**, *6*, 39–50. [[CrossRef](#)]
19. Khalak, A.; Williamson, C.H.K. Investigation of the relative effects of mass and damping in vortex induced vibration of a circular cylinder. *J. Wind Eng. Ind. Aerodyn.* **1997**, *69–71*, 341–350. [[CrossRef](#)]
20. IcemCfd, A. *12.0 User’s Ma*; Ansys Inc.: Canonsburg, PA, USA, 2009; Volume 5.
21. Fluent, A. *12.0 Theory Guide*; Ansys Inc.: Canonsburg, PA, USA, 2009; Volume 5.
22. Menter, F.R. Two-equation eddy-viscosity turbulence models for engineering applications. *AIAA J.* **1994**, *32*, 1598–1605. [[CrossRef](#)]
23. Anton, G. Analysis of Vortex-Induced Vibration of Risers. Master’s Thesis, Applied Mechanics, Chalmers University of Technology, Gothenburg, Sweden, 2012.
24. Vandiver, J.K. Damping parameters for flow-induced vibration. *J. Fluids Struct.* **2012**, *35*, 105–119. [[CrossRef](#)]
25. Schlichting, H. *Boundary Layer Theory*, 8th ed.; McGraw-Hill Book Company: New York, NY, USA, 1979; ISBN 13 978-3540662709.
26. Iaccarino, G.; Mishra, A.A.; Ghili, S. Eigenspace perturbations for uncertainty estimation of single-point turbulence closures. *Phys. Rev. Fluids* **2017**, *2*, 024605. [[CrossRef](#)]
27. Mishra, A.A.; Gianluca, I. Uncertainty Estimation for Reynolds-Averaged Navier Stokes Predictions of High-Speed Aircraft Nozzle Jets. *AIAA J.* **2017**, *55*, 3999–4004. [[CrossRef](#)]
28. Govardhan, R.; Williamson, C.H.K. Modes of vortex formation and frequency response for a freely-vibrating cylinder. *J. Fluid Mech.* **2000**, *420*, 85–130. [[CrossRef](#)]
29. Chen, W.; Zhang, Q.; Li, H.; Hu, H. An experimental investigation on vortex induced vibration of a flexible inclined cable under a shear flow. *J. Fluids Struct.* **2015**, *54*, 297–311. [[CrossRef](#)]
30. Feng, C.C. The Measurements of Vortex Induced Effects in Flow Past a Stationary and Oscillating Circular and D-Section Cylinders. Master’s Thesis, The University of British Columbia, Vancouver, BC, Canada, 1968.
31. Naudascher, E.; Rockwell, D. *Flow Induced Vibration—An Engineering Guide*; Dover Publications Inc.: Mineola, NY, USA, 2005; pp. 37–38, ISBN 13 978-0-486-44282-2.
32. Domal, V.; Sharma, R. An experimental study on vortex-induced vibration response of marine riser with and without semi-submersible. *J. Eng. Marit. Environ.* **2017**, *232*, 176–198. [[CrossRef](#)]



ACCEPTED MANUSCRIPT

# An Experimental Investigation on Wear and Corrosion Characteristics of Mg-Co nanocomposites

To cite this article before publication: Raghav G R *et al* 2018 *Mater. Res. Express* in press <https://doi.org/10.1088/2053-1591/aac862>

## Manuscript version: Accepted Manuscript

Accepted Manuscript is “the version of the article accepted for publication including all changes made as a result of the peer review process, and which may also include the addition to the article by IOP Publishing of a header, an article ID, a cover sheet and/or an ‘Accepted Manuscript’ watermark, but excluding any other editing, typesetting or other changes made by IOP Publishing and/or its licensors”

This Accepted Manuscript is © 2018 IOP Publishing Ltd.

During the embargo period (the 12 month period from the publication of the Version of Record of this article), the Accepted Manuscript is fully protected by copyright and cannot be reused or reposted elsewhere.

As the Version of Record of this article is going to be / has been published on a subscription basis, this Accepted Manuscript is available for reuse under a CC BY-NC-ND 3.0 licence after the 12 month embargo period.

After the embargo period, everyone is permitted to use copy and redistribute this article for non-commercial purposes only, provided that they adhere to all the terms of the licence <https://creativecommons.org/licenses/by-nc-nd/3.0>

Although reasonable endeavours have been taken to obtain all necessary permissions from third parties to include their copyrighted content within this article, their full citation and copyright line may not be present in this Accepted Manuscript version. Before using any content from this article, please refer to the Version of Record on IOPscience once published for full citation and copyright details, as permissions will likely be required. All third party content is fully copyright protected, unless specifically stated otherwise in the figure caption in the Version of Record.

View the [article online](#) for updates and enhancements.

# An Experimental Investigation on Wear and Corrosion Characteristics of Mg-Co nanocomposites

**G.R.Raghav<sup>1</sup>, A.N.Balaji<sup>2\*</sup>, D.Muthukrishnan<sup>3</sup>, V.Sruthi<sup>4</sup>, E.Sajith<sup>5</sup>**

<sup>1,2,3</sup>Department of Mechanical Engineering, KLN College of Engineering, Pottapalayam, Sivagangai Dt. Tamilnadu, India630612

<sup>4</sup>Department of Basic Science and Humanities, SCMS School of Engineering & Technology, Cochin, Kerala, India 683582

<sup>5</sup>Department of Mechanical Engineering, SCMS School of Engineering & Technology, Cochin, Kerala, India 683582

\* Corresponding author: A.N.Balaji, E-mail: [balajime@yahoo.com](mailto:balajime@yahoo.com)

## Abstract:

In this research, Mg-Co nanocomposites were synthesized using powder metallurgy process. The impact of Co nanoparticle reinforcements on the hardness, wear and corrosion characteristics of Mg-Co nanocomposites were investigated. The dry sliding wear of the Mg-Co nanocomposites was examined using pin-on-disc apparatus under various loading conditions. The results substantiate that the hardness (70 HV) and wear resistance of Mg-25Co were higher than pure Mg (25 HV). The morphological analysis of Mg-based nanocomposites has been carried out using Scanning Electron Microscope and Atomic Force Microscope. The electrochemical corrosion analysis reveals that the increase in Co content in Mg matrix decreases the corrosion rate. The Mg-25Co nanocomposites shows better corrosion resistance ( $I_{corr} = 0.397 \times 10^{-3} \mu A/cm^2$ ) than that of Pure Mg ( $I_{corr} = 0.544 \times 10^{-3} \mu A/cm^2$ ). An increase in Polarization resistance ( $R_p$ ) also authenticates the increase in corrosion resistance of Mg-25Co nanocomposites. The EIS spectroscopy results reveal that the charge transfer resistance ( $R_{ct}$ ) has enhanced from  $14.44 \Omega cm^2$  for the pure Mg to  $42.50 \Omega cm^2$  for the Mg-25Co nanocomposites.

Keywords: Wear, Corrosion, Dental implants, SEM, EDAX

## 1. Introduction

Generally, the orthopaedic implants are made up of metals because of their substantial mechanical properties such as ductility and formability. The potential biodegradable material which is attracting more potential research is Mg and its alloys because of its biocompatibility, physical and mechanical properties[1–5]. The Mg with a density of about  $1.74 \text{ g/cm}^3$  makes it much lighter than of other biodegradable metals and is appropriate for dental and orthopaedic implants. Besides the Mg has poor corrosion resistance which limits the application of Mg alloys in dental and orthopaedic implants[6–8].

Another such kind of metal is cobalt and cobalt-based alloys which are most potent and widely suited for dental and orthopaedic implants owing to its high corrosion and wear resistance along with its high strength[9–15]. The most common alloying element of Mg-based composites is Cr, Mo, Ni, etc. so as to improve the wear and corrosion resistance properties. The major concerns of Cr, Mo, and Ni reinforcements are the development of Carbides which in turn reduces the ductile property of the composite. The other major entanglement is the release of dangerous ions and particles which can result in adverse effects such as allergy, toxicity and carcinogenic issues[13,14,16–19].

AjithKumar.K. K et al [3]studied the dry sliding behaviour of Mg-Si alloys prepared using gravity casting method. The results show that the wear rate decreases with the increase in Si Content in Mg matrix. Renqi Ma et al investigated the effect of Co reinforcement in WC using spark plasma sintering the results shows that the fracture toughness increases with increase in Co content[10].

So by considering the important properties of Mg andCo, it is proposed to study the effect of reinforcement of Cobalt in the Mg-based composite. The studies on Mg-Co alloys have been rather limited especially on tribological and corrosion behaviours[20,21]. In this work,Mg-Co nanocomposites for potential dental implants were prepared using powder metallurgy process. The various wear mechanisms were studied using pin-on-disc apparatus under different loading and sliding conditions. The corrosion characteristics of the composites were analyzed using electrochemical methods.

## 2. Materials and Methods

### 2.1 Materials:

The magnesium (600  $\mu\text{m}$ ) and cobalt (100  $\mu\text{m}$ ) powders (research grade) of purity levels 99.5% and 99% respectively were used as matrix and reinforcements in this work. The particle size, microstructures and presence of Mg and Co are analyzed using SEM and EDAX.

### 2.2 Preparation of Composite materials:

Table.1 shows the different proportions of composites that were prepared in this work. The various proportions of Mg and Co were milled under the presence of Toluene in high energy ball mill [Fritsch pulverisette, Germany] at 300 rpm for 5h with Tungsten Carbide balls so as to obtain a homogeneous composite mixture. The Toluene was used in order to provide uniform, perfect mixing and also to avoid unwanted reactions. The powder to ball ratio was maintained at about 1:20. The Blended composite mixtures are then fed into a cylindrical die of 10 mm diameter and compacted using the hydraulic press at a load of 500 Mpa. The green compacts are then sintered at the temperature of about 550<sup>o</sup> C for 1h in a muffle furnace under argon atmosphere in Contemplation of obtaining a composite pellet.

### 2.3 Micro hardness:

The contact surfaces of the sintered composites were polished using abrasive papers of grades 600, 800 and 1000 in order to remove any impurities present at the contact surfaces. The microhardness of the composite pellets was studied using Vickers hardness tester at a uniform load of 5 kg. The dwell time was maintained at about 20 sec.

### 2.4 Characterization

The surface topographies of Mg–Co nanocomposites were studied using Atomic Force Microscopy (XE70, Park System, South Korea). The morphological characterization of the Mg-Co nanocomposite was done using SEM (Hitachi SU1510, Secondary Electron Mode, 10 KV, the emission current of 96 $\mu\text{A}$ ). The compositional analysis of specimens was analyzed using EDX (QUANTAX - Bruker).

### 2.5 Wear analysis:

The Mg-Co composite pellets of 10 mm diameter and 30 mm in height were used as the test specimen. The dry sliding wear analysis was performed according to ASTM: G99 standards

1  
2  
3 using pin-on-disc apparatus (DUCOM, Bangalore). The tribological studies of the composite  
4 pellets were analyzed considering the criteria's such as applied load, sliding distance and sliding  
5 speed for five respective trials (n=5) and the mean values were considered. The composite pellets  
6 were measured before and after the wear analysis using an electronic weighing scale to  
7 determine the weight loss due to wear mechanism.  
8  
9

## 10 11 12 **2.6 Potentiometric Polarization test:**

13  
14 The potentiometric polarization analysis was used to explore the electrochemical  
15 corrosion behaviour of Mg-Co nanocomposites. The potentiometric tests were premeditated  
16 using Biologic SP-150 potentiostat. The investigations were performed using three electrode cell  
17 consists of platinum wire counter electrode Ag/AgCl reference electrode and the Magnesium-  
18 Cobalt nano composite pellet as a working electrode. The polarization tests were carried out at  
19 room temperature with the 5 wt. % NaCl solution. The composite pellets were polished with  
20 emery paper which was rinsed with acetone and double distilled water prior to the  
21 electrochemical tests. The Mg-Co nanocomposite working electrodes were immersed in the  
22 electrolytic solution of 5 wt. % NaCl for 1 h in order to reach steady state open circuit potential  
23 and the OCP was measured. The scan rate was maintained at 5 mV/s. The corrosion potential  
24  $E_{corr}$  and current density  $I_{corr}$  were calculated using EC lab software through Tafel fit  
25 extrapolation.  
26  
27  
28  
29  
30  
31  
32  
33

## 34 35 **2.7 Electro Chemical Impedance Spectroscopy:**

36  
37 The electrochemical impedance spectroscopy (EIS) for the composite specimens was  
38 executed at the range of 100 kHz to 100 MHz and 10 mV initial sinusoidal voltage. The Biologic  
39 SP-150 electrochemical workstation was used to carry out experiments with open circuit  
40 potential. The EC-lab software was then utilized for fitting and analyzing the raw EIS  
41 data.[22,23]  
42  
43  
44  
45

## 46 47 **3 Results and Discussion:**

### 48 49 **3.1 Microhardness:**

50 The Fig. 1 shows the mean hardness values of Mg-Co composite samples for a sample  
51 size of n = 10. From the figure, it is evident that the hardness of the composites increase hugely  
52 with an increase in Co content owing to its inherent hard nature. The Mg-25Co composite has a  
53 hardness of about 70 HV compared to that of pure Mg which has a hardness of 25 HV.  
54  
55  
56  
57  
58  
59  
60

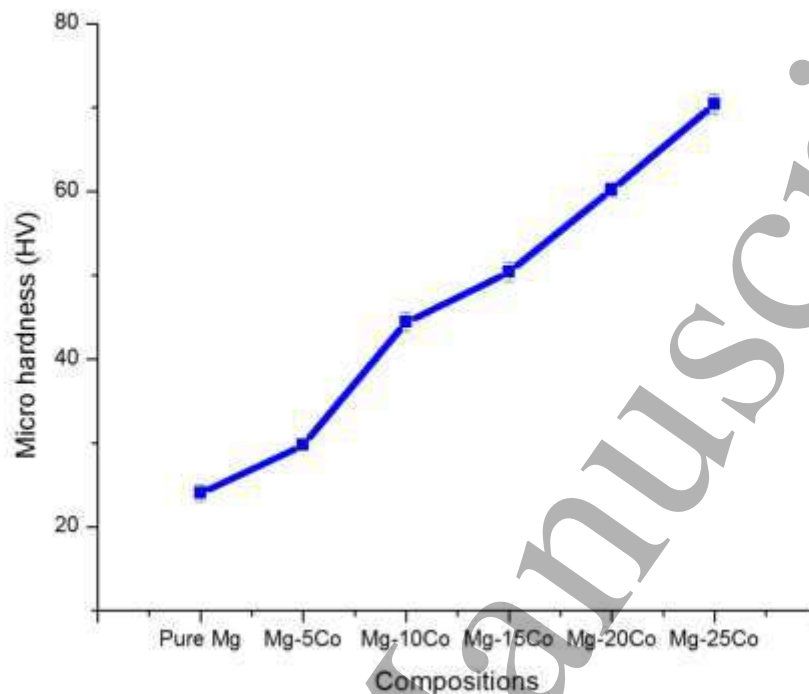
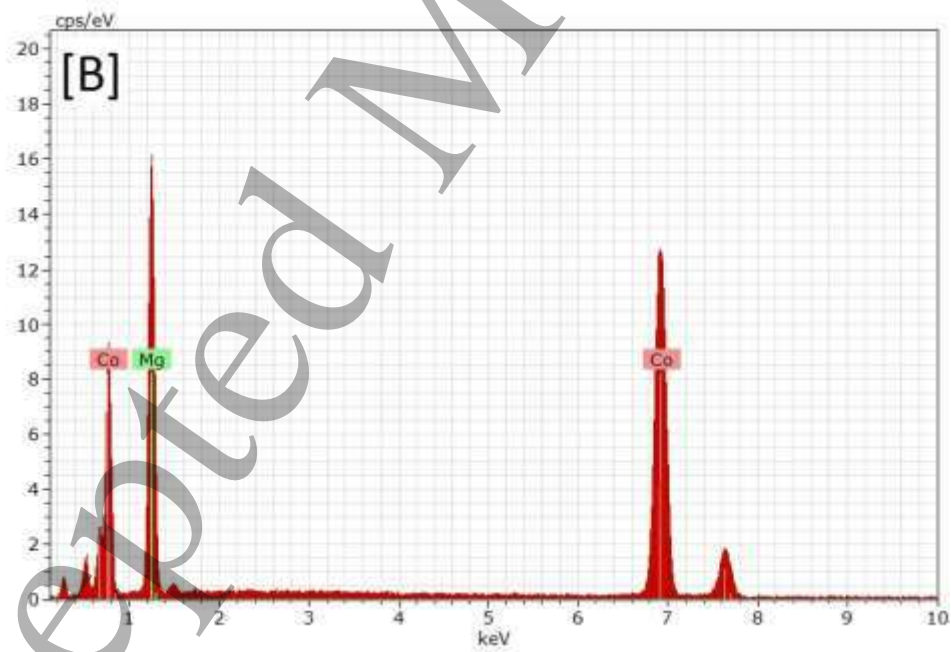
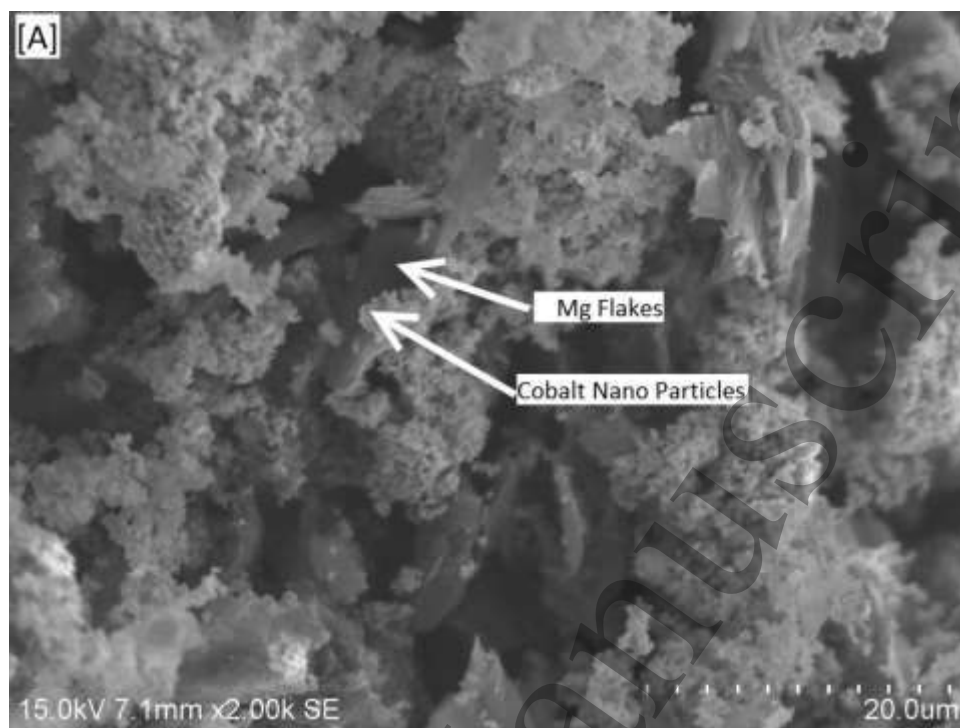


Fig.1 Graphical representation of micro hardness values of different composition of Mg-Co nanocomposites (Standard deviation  $\sigma$ ).

### 3.2 SEM Analysis:

Fig 2.A& 2B shows the morphological structure and EDAX spectrum of Magnesium-Cobalt nanocomposites. The SEM image noticeably reveals the unvarying mixture of Mg-Co composites. The EDAX spectrum substantiates the presence of magnesium, cobalt and oxides in the composite material. The particle size of Mg and Cobalt were found to be in the range of 500 microns and 80-150 nm respectively. The Co nanoparticles were seen to be agglomerated.



52 *Fig.2 SEM image [A] and EDAX Spectrum [B] of Mg-Co nanocomposite*

53  
54  
55  
56  
57  
58  
59  
60



### 3.3 AFM Analysis

Atomic force microscopy is one of the important tools in studying the topography of materials, with demonstrated resolution in the order of a nanometer. Fig 3, illustrate the 3D AFM Image which shows the stature and breadth of the Cobalt nanoparticles which is recognized to be around 10 – 20 nm and 300 nm respectively.

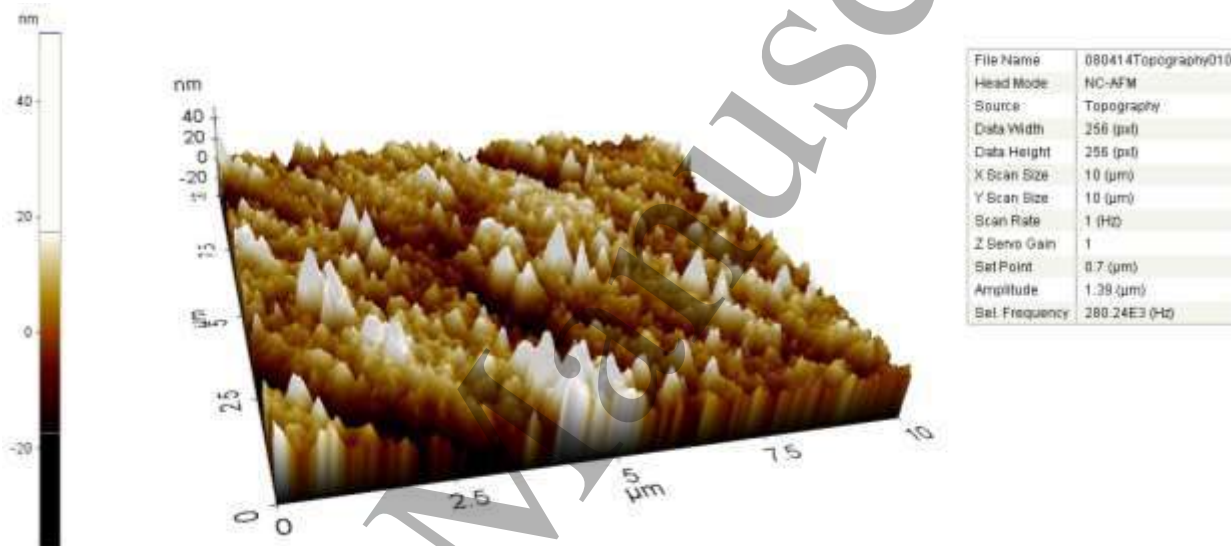
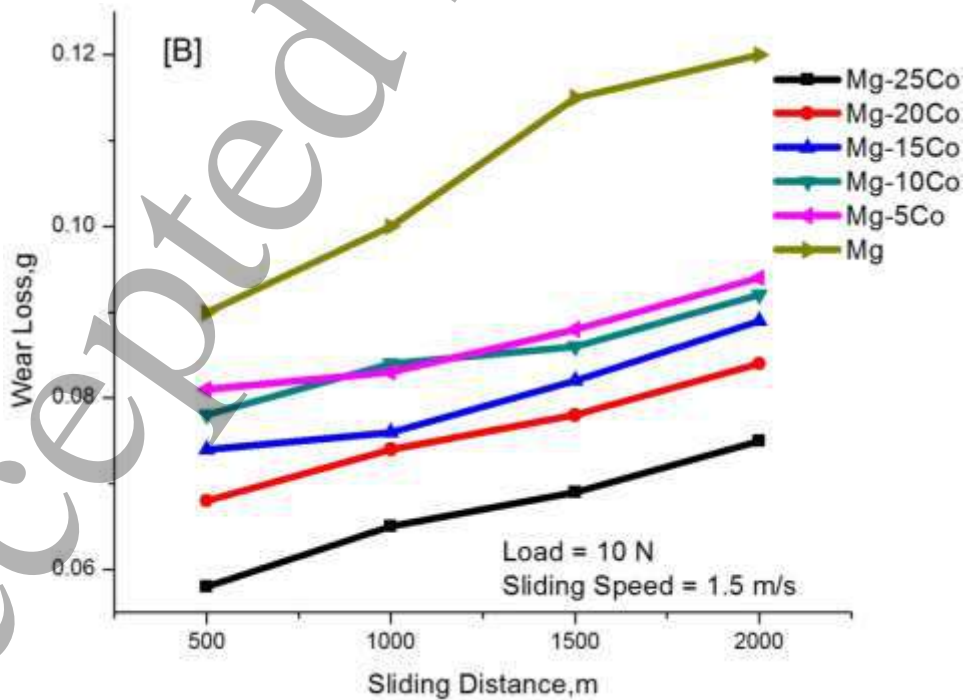
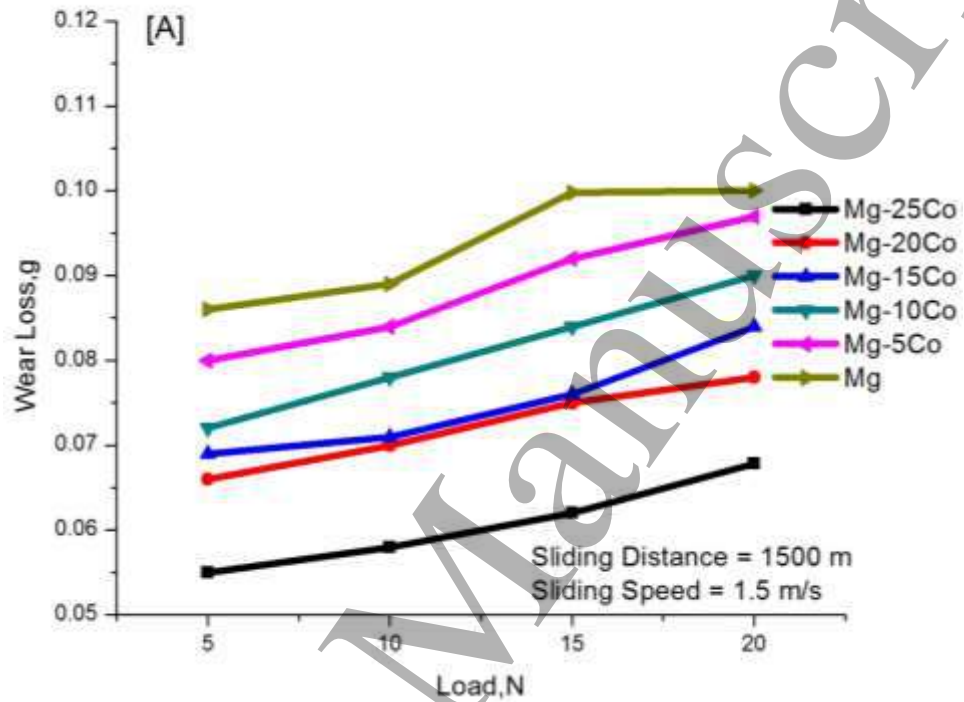


Fig.3 3D AFM Image of cobalt nanoparticles

### 3.4 Sliding Wear Analysis:

The investigation on wear is done using Pin-on-disc apparatus for the study of the Tribological behaviour of Mg-Co nanocomposites. From the Fig.4 we can add fact that the addition of Co decreases the wear loss of the composites as compared to that of pure Mg pellets. The outcome discloses that increase in the percentage of Cobalt in Mg matrix has further improved the wear resistance. The Mg-25Co nanocomposites have less wear loss than Mg-5Co. Fig.4 (A) shows the wear loss sustained by specimens at various loads ranging from 5 N to 20 N. From the graphs, it is perceptible that the Mg-Co composites show an increase in wear resistance at different loads and also with an increase in the percentage of Co. This may be due to hardening of composites due to the presence of Co in the composite pellets. The wear loss experience ranging from 500 m to 2000 m is shown in the Fig. 4(B). It can be noted that increase of Co content in nanocomposites decreases the wear loss which may be due to the hard nature of

Co reinforcements. The Fig.4(C) characterizes the trend of wear loss of composite materials at various sliding speed. From the figure, it is evident that the wear loss decreases with increase in sliding speed.



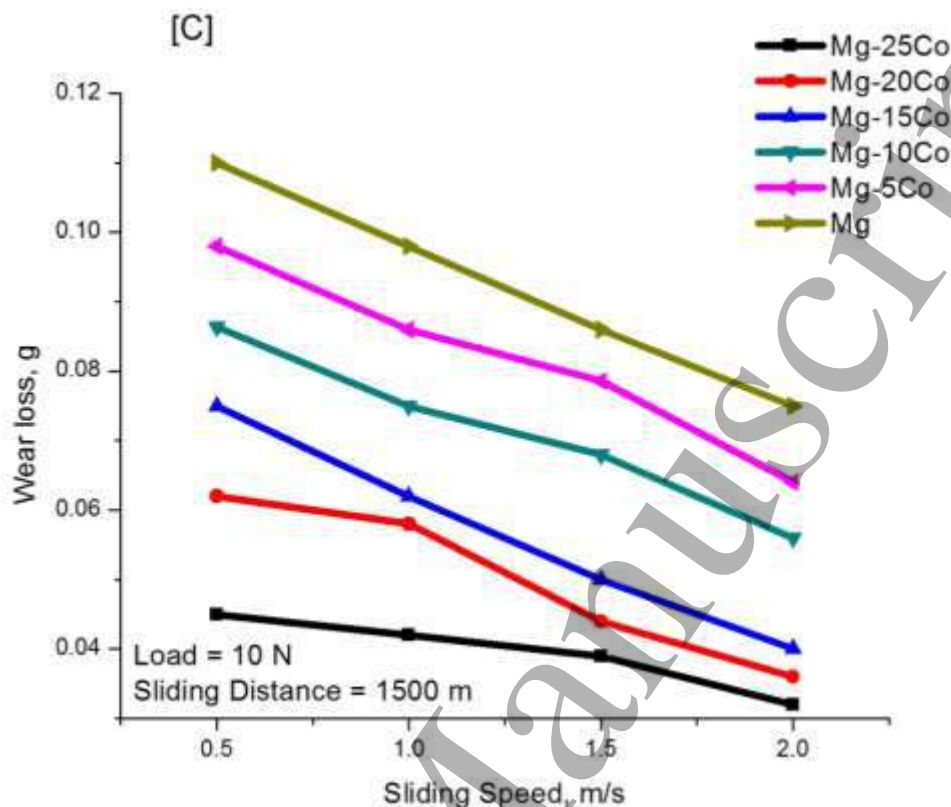
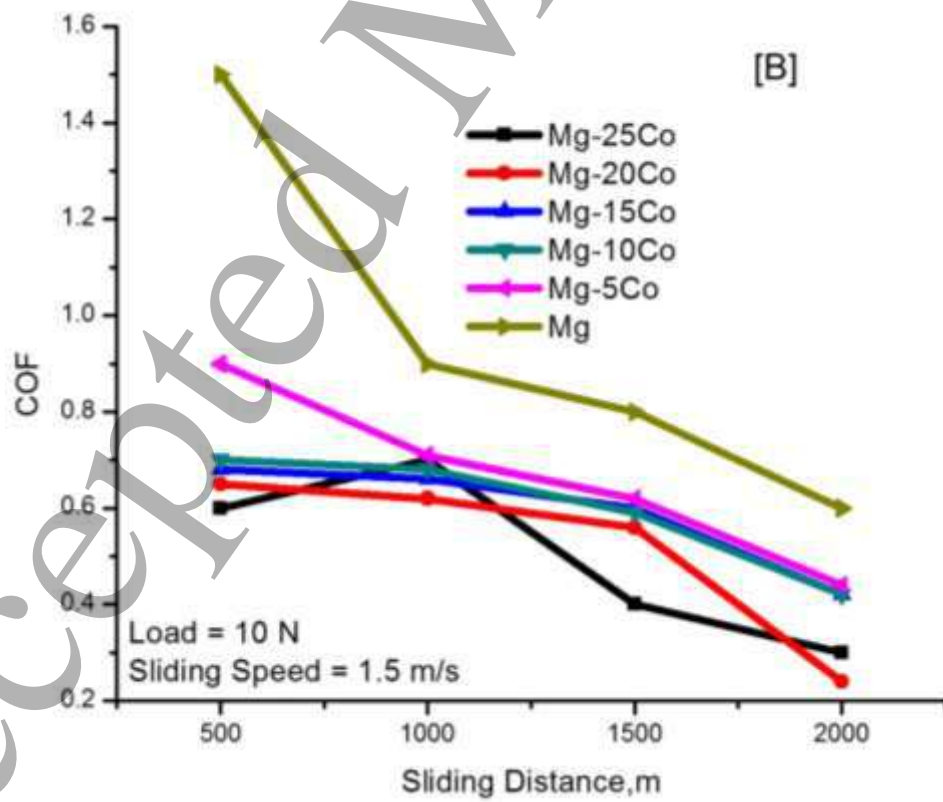
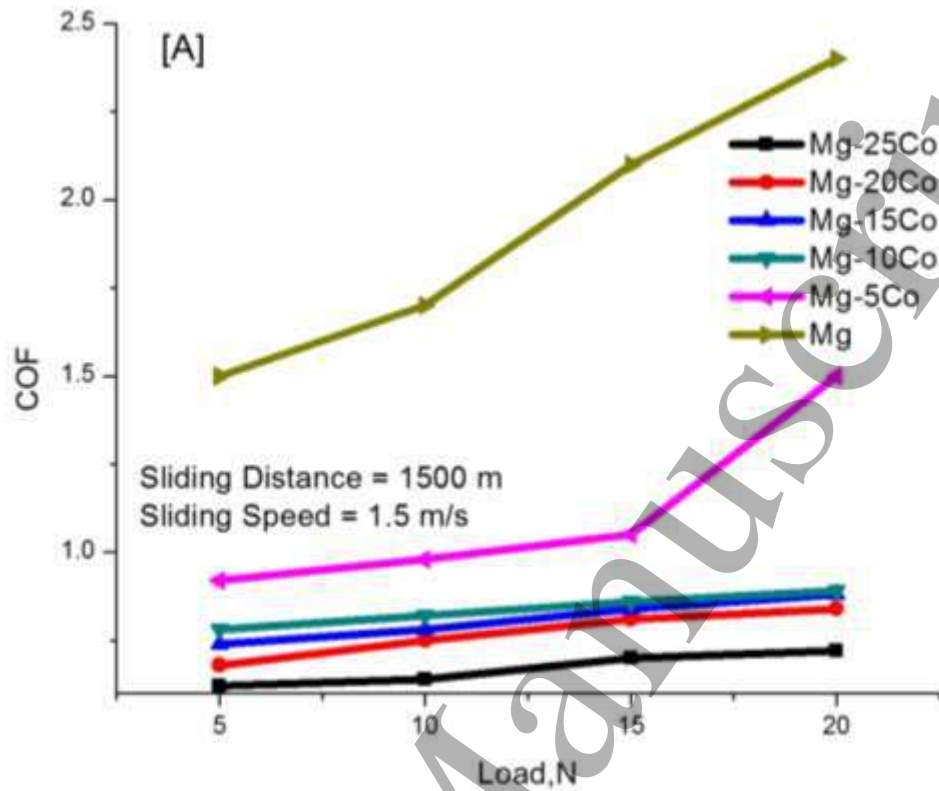


Fig.4 Wear Loss ( $n = 5$ ) of Mg and Mg-Co nanocomposites (A) Applied Load, (B) Sliding Distance, (C) Sliding Speed

### 3.5 Coefficient of Friction Analysis (COF):

The Fig. 5 gives you an idea about the various trends of Coefficient of friction of Mg-Co composites. The COF decreases with increase in Co reinforcements; this is because of the inherent hard nature Co particles. The results uncover that the COF of Mg-25Co is lesser compared to that of pure Mg pellet. The Coefficient of friction of composite specimens is revealed in the Fig.5 (A) which discloses that the pure Mg has the higher COF with an increase in load but the COF of the composites remains more or less unwavering at various loading conditions. From the fig. 5(B) it is unmistakable that the COF values of Mg-Co composites show a considerable decline with the rise in sliding distance whereas the Mg has higher COF values. The evaluation of Fig.5(C) states that there is a linear decrement in COF values with a boost in sliding speed.



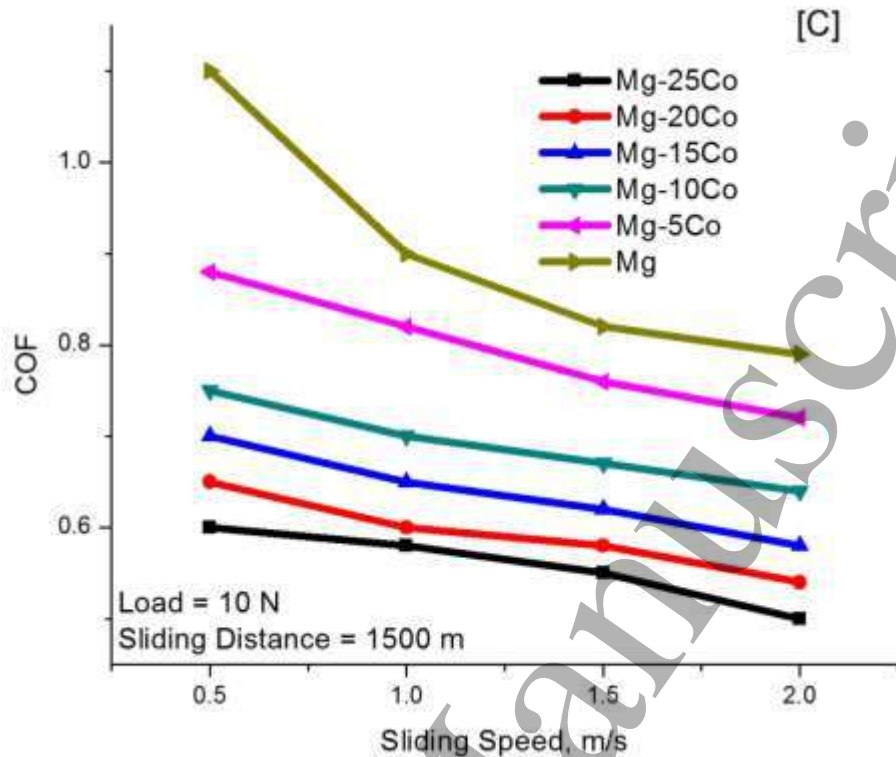
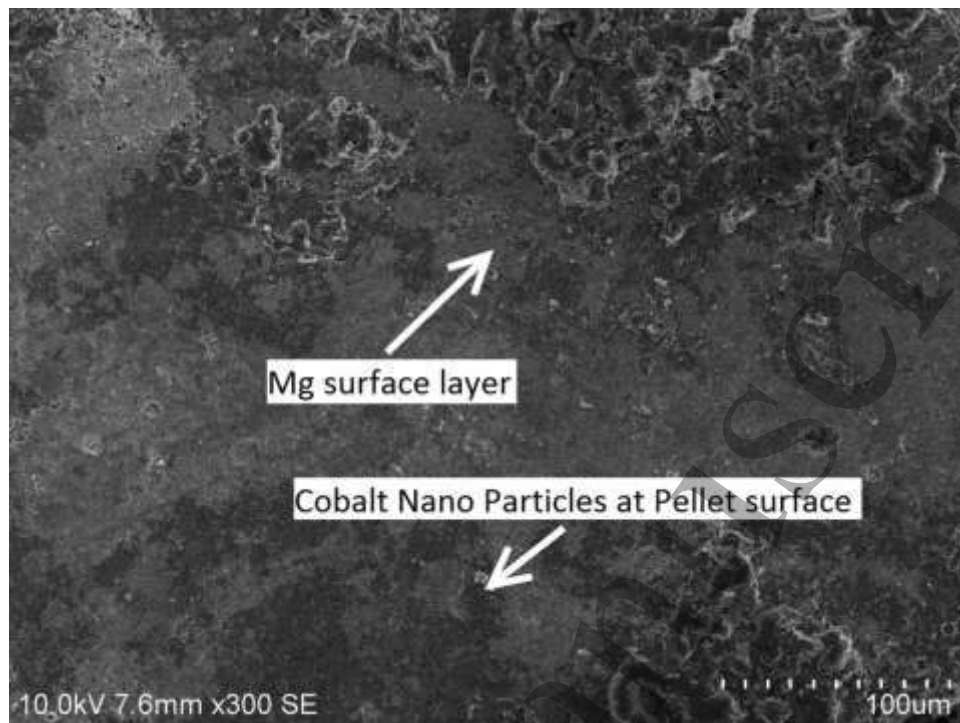


Fig.5 COF ( $n = 5$ ) of Mg and Mg-Co nanocomposites (A) Applied Load, (B) Sliding Distance, (C) Sliding Speed

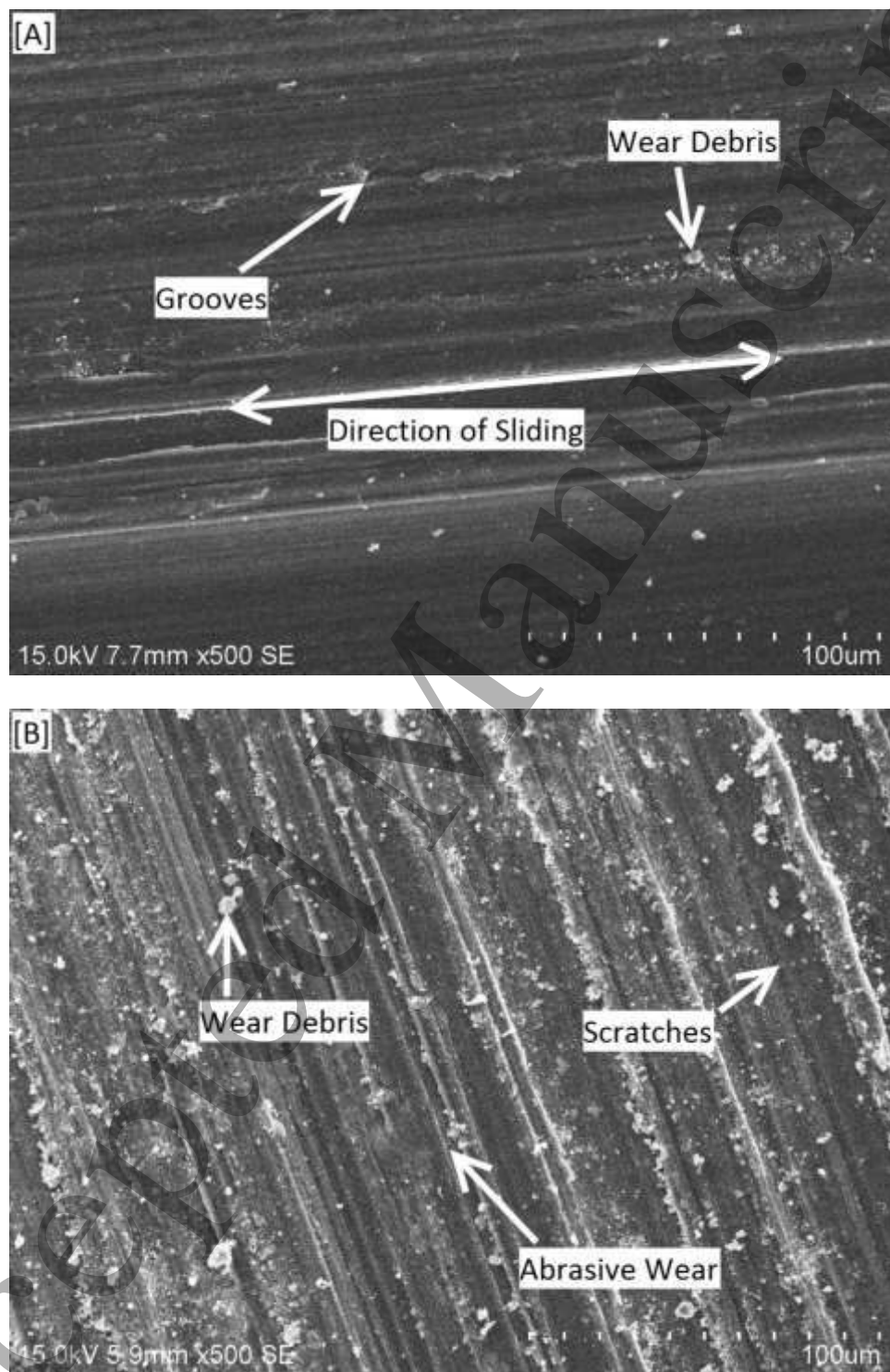
### 3.6 Worn out surface Analysis:

Fig 6 shows the surface morphology of Mg- 25Co nanocomposite pellet before the test, which shows the homogeneous diffusion of Cobalt in Mg matrix. Fig 7 A & B unveil the worn out surfaces of the Pure Mg and Mg-25Co nanocomposite pellets after sliding wear test. The scratches and grooves were formed in the direction of sliding which confirms the mechanism of wear due to abrasive wear involving the composite pellet and rotating disc. The SEM micrograph shows the formation of grooves in the subsurface microstructure of the pure Mg pellets which attributes to the abrasive wear as compared to Mg-Co pellets.



27 *Fig. 6 SEM Micrograph of Mg- 25 Co nanocomposite pellet before Wear Test*

28  
29  
30  
31  
32  
33  
34  
35  
36  
37  
38  
39  
40  
41  
42  
43  
44  
45  
46  
47  
48  
49  
50  
51  
52  
53  
54  
55  
56  
57  
58  
59  
60



53 *Fig.7 SEM Micrograph of Pure Mg (A) and Mg-25Co (B) nanocomposite pellet after the wear*  
54 *test*  
55  
56  
57  
58  
59  
60

### 3.7 Potentiometric Polarization Analysis:

The potentiometric polarization investigation of the pure Mg and various compositions of Mg-Co composites in a 5 wt % NaCl solution is plotted in Fig.8; the graphs scheme against potential voltage and current density. The composite materials show unpassivated anodic and cathodic curves. The current density declines with increased potential voltage. This observable fact is due to the formation of Magnesium oxide layers at the facade of the specimen. The corrosion characteristics such as corrosion potential ( $E_{\text{corr}}$ ), Current density ( $I_{\text{corr}}$ ) and polarization resistance ( $R_p$ ) are determined by Tafel extrapolation method. From the Table: 1 it can be comprehended that corrosion potential ( $E_{\text{corr}}$ ) of Mg-25Co nanocomposites (-0.813 V vs Ag/AgCl) is decreased than that of pure Mg (-0.940 V vs Ag/AgCl) which confirms the increase in corrosion resistance of the composites. The Current density of the Mg-25Co nanocomposites ( $0.397 \times 10^{-3} \mu\text{A}/\text{cm}^2$ ) has reduced considerably when compared to pure Mg ( $0.544 \times 10^{-3} \mu\text{A}/\text{cm}^2$ ). The drop in current density reduces the intensity of the corrosion in composite specimens which in turn diminishes the rate of the corrosion. The polarization resistance ( $R_p$ ) rises with accumulation in Co content in Mg matrix composites which also substantiate the reduction in corrosion rate of the Mg-Co nanocomposites [17,24–27]. The one way ANOVA statistical analysis for the corrosion potential ( $E_{\text{corr}}$ ) of pure Mg and composite pellets confirm that there is a considerable increase in corrosion potential ( $E_{\text{corr}}$ ) of the Mg-25Co nanocomposites when compared to pure Mg ( $p < 0.05$ ) is shown in Fig.9. Further, the statistical analysis of the composite specimens has shown significant variation in corrosion current ( $I_{\text{corr}}$ ). Fig.10 depicts the comparative variations in the corrosion current for each composite.



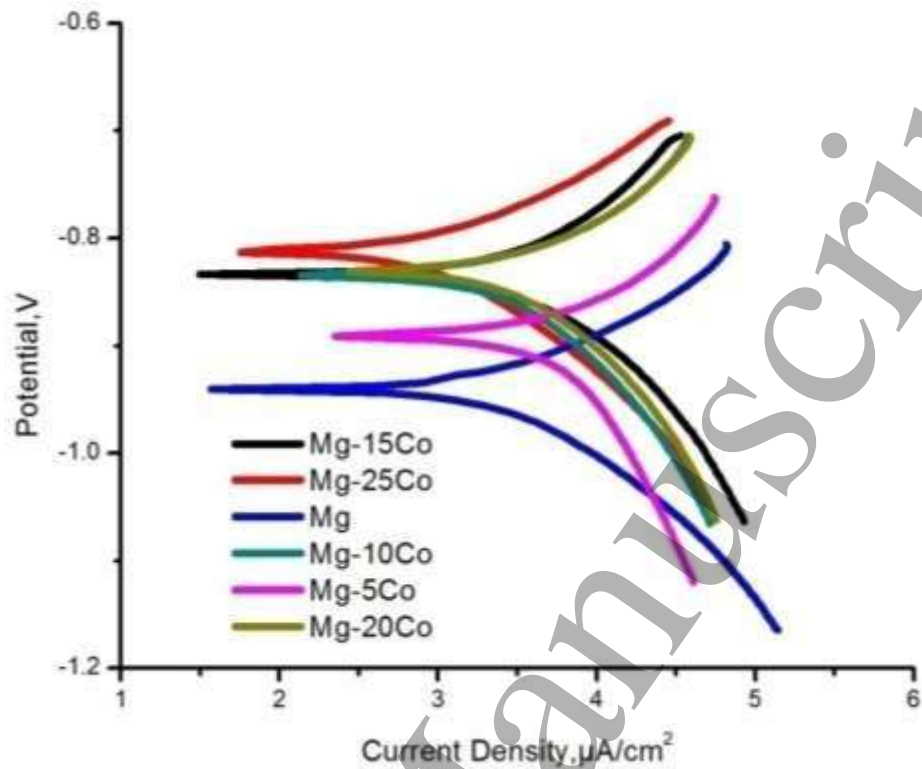


Fig.8 Potentiometric Polarization Curves of Mg and Mg-Co nanocomposites

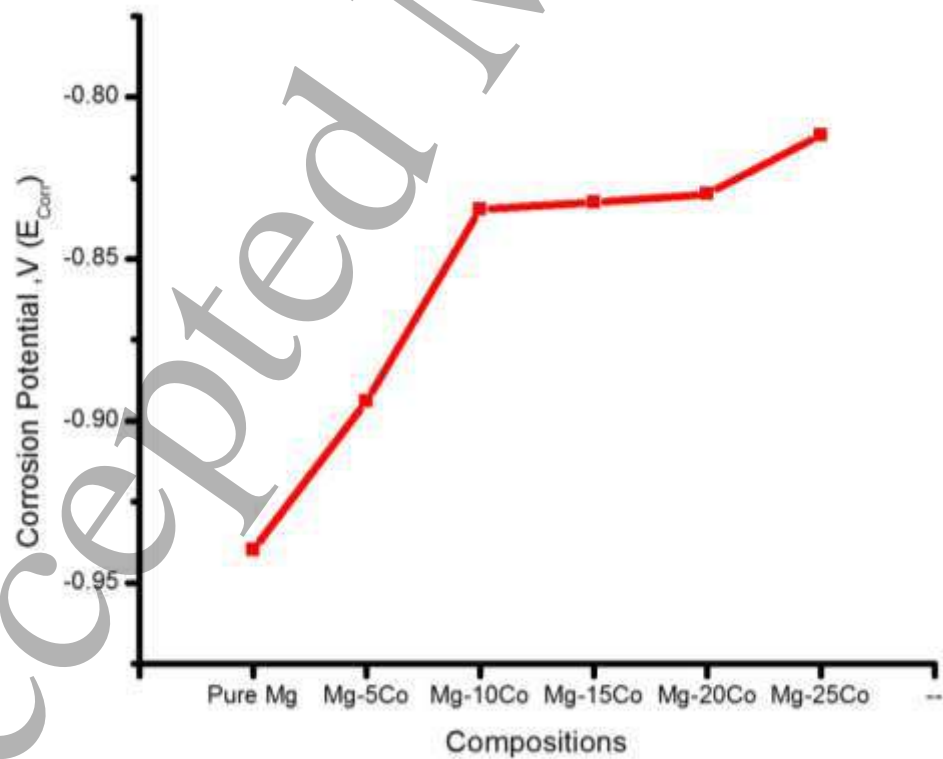


Fig.9 Statistical analysis of the corrosion potential ( $E_{\text{corr}}$ ) of Mg and Mg-Co nanocomposites

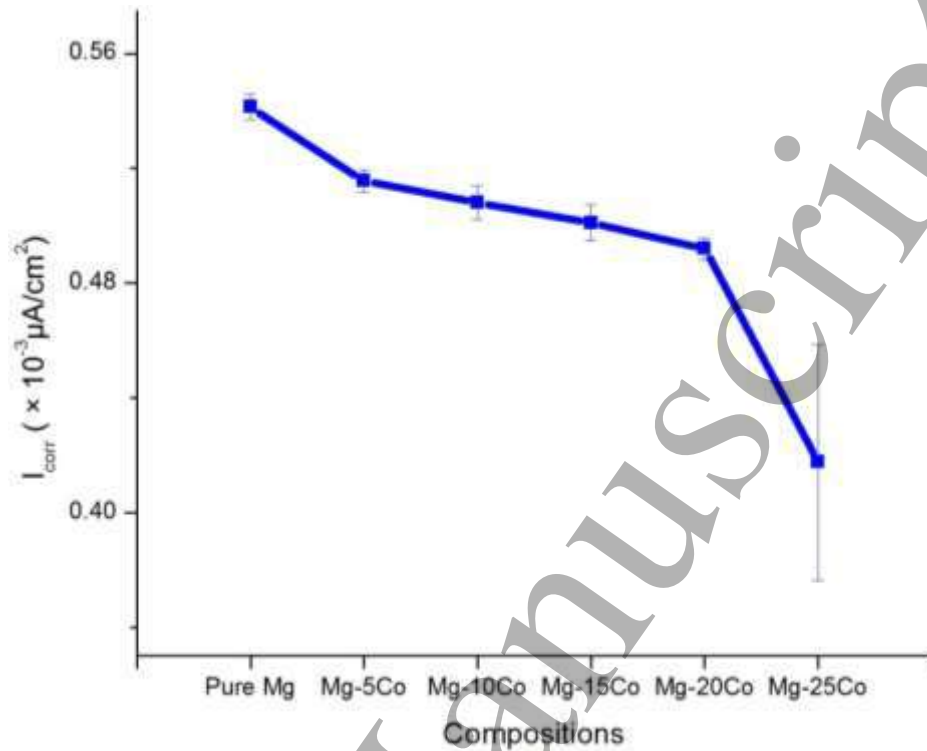


Fig.10 Statistical analysis of the corrosion current ( $I_{corr}$ ) of Mg and Mg-Co nanocomposites

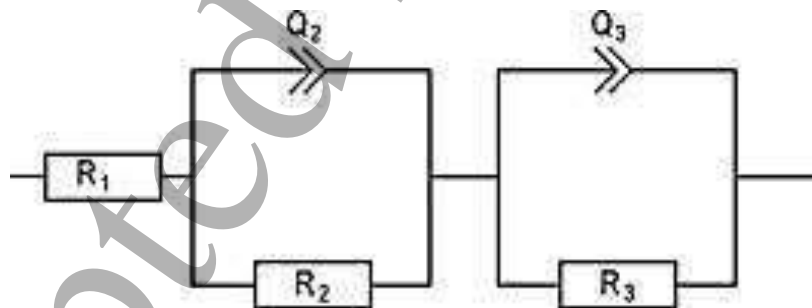
Table 1: Electrochemical corrosion Characteristics of the Pure Mg and Mg-Conanocomposites

S.No	Specimen	$E_{corr}$ (V)	$I_{corr} (\times 10^{-3} \mu A/cm^2)$	Polarization resistance, $R_P$ ( $\times 10^{-4} \Omega cm^2$ )
1	Pure Mg	-0.940 ± 0.001	0.544 ± 0.004	2.79 ± 0.04
2	Mg-5Co	-0.894 ± 0.153	0.511 ± 0.004	2.80 ± 0.02
3	Mg-10Co	-0.834 ± 0.153	0.510 ± 0.006	2.87 ± 0.04
4	Mg-15Co	-0.833 ± 0.100	0.505 ± 0.006	2.90 ± 0.02
5	Mg-20Co	-0.830 ± 0.129	0.491 ± 0.004	2.93 ± 0.02
6	Mg-25Co	-0.813 ± 0.001	0.397 ± 0.041	3.61 ± 0.5

### 3.8 Electrochemical Impedance Spectroscopy Analysis:

EIS spectroscopy was employed to study the corrosion resistance properties of Mg-Co nanocomposites. Fig.11 shows the equivalent circuit used for fitting the Nyquist impedance for the Mg-Co nanocomposites.  $R_1$  corresponds to the resistance of the electrolytic solution (NaCl)

1  
2  
3 at room temperature. The  $R_2$  can be judged as charge transfer resistance which is inversely  
4 proportional to the corrosion rate [28,29]. The  $Q_2$  and  $Q_3$  are interpreted as constant phase  
5 elements which are used to calculate the true capacitance of the nanocomposite specimens. The  
6  
7 resistance  $R_3$  is related to the effect of Co nanoparticle reinforcement. The Fig.12 shows two  
8  
9 characteristic arcs at higher and lower frequency region. The larger arc is due to the electron  
10  
11 transfer within the Mg-Co nanocomposite working electrode and the smaller arc at the lower  
12  
13 frequency region is due to the diffusion at the interface of Mg-Co nanocomposite electrode and  
14  
15 the electrolyte [30]. The perfect capacitance behaviour is not seen in this study and for this  
16  
17 reason, a constant phase element (CPE) is introduced in the equivalent circuit[23,31].The  
18  
19 measured resistance and CPE values of the Mg-Co nanocomposites are shown in Table.2. From  
20  
21 the table, it is evident that the charge transfer resistance ( $R_{ct1}$ ) of the Mg-25Co nanocomposites  
22  
23 ( $R_{ct1}= 42.50 \Omega \text{ cm}^2$ ) has improved than the pure Mg ( $R_{ct1}= 14.44 \Omega \text{ cm}^2$ ) which confirms the  
24  
25 improvement in corrosion resistance of Mg-25Co nanocomposites. The charge transfer  
26  
27 capacitance of the Mg-Co nanocomposites decreases with increase in Co content which may be  
28  
29 attributed due to the double layer capacitance. The true capacitance calculated from the constant  
30  
31 phase elements and resistance values also confirm that the Mg-25Co nanocomposite ( $C= 0.0198$   
32  
33  $\text{Fcm}^{-2}$ ) have lesser Capacitance value compared to pure Mg ( $C = 0.4729 \text{ Fcm}^{-2}$ ).



45  
46  
47  
48  
49  
50  
51  
52  
53  
54  
55  
56  
57  
58  
59  
60

Fig.11 The Equivalent circuit for fitting EIS

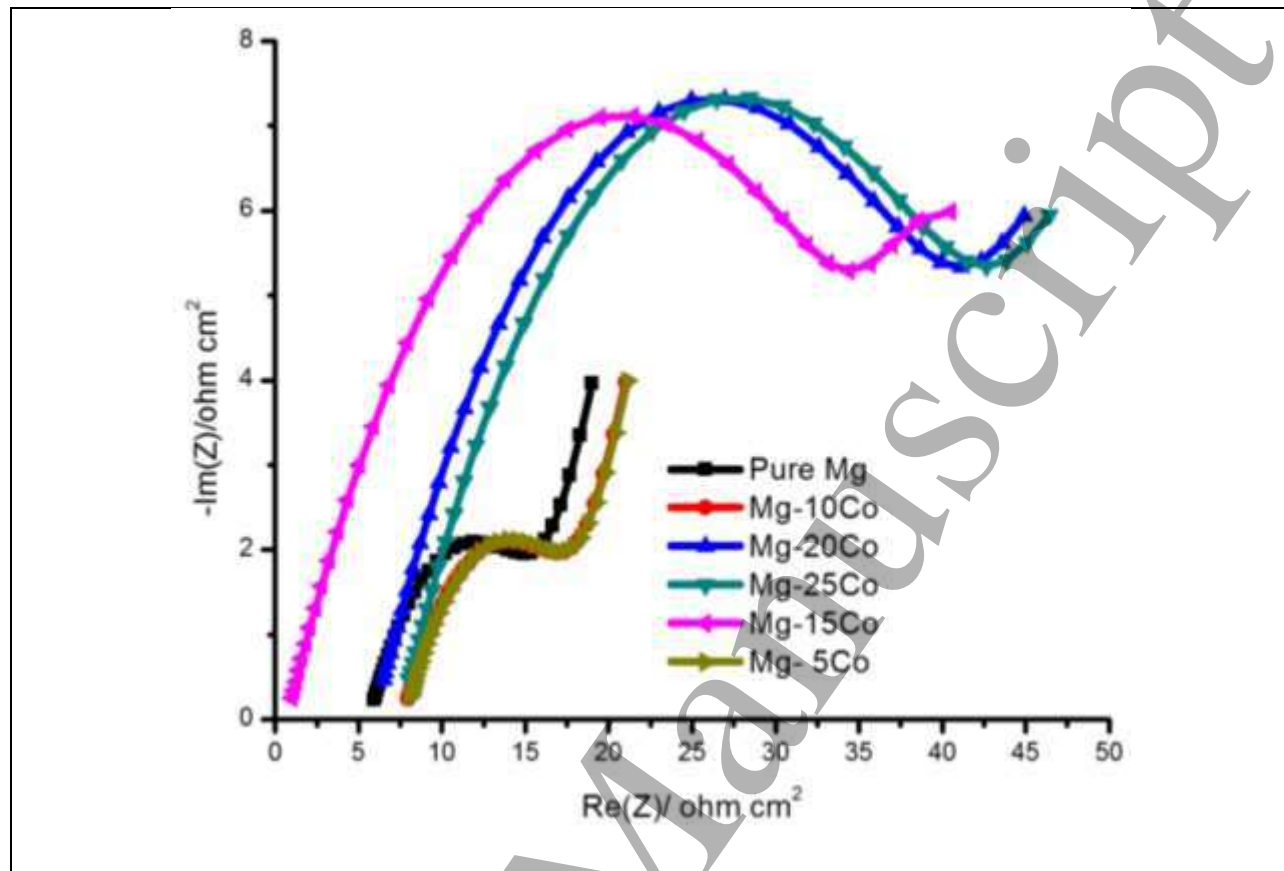


Fig.12 EIS Spectra of Mg-Co nano composites

Table 2: Charge transfer resistance obtained from EIS data fitting by equivalent circuit model (Standard deviation  $\sigma$ )

S.No	Specimen	$R_s$ ( $\Omega \text{ cm}^2$ )	$Q_2$ ( $\text{F.s}^{\wedge} \text{ cm}^{-2}$ )	$C_{dl1}$ ( $\text{F cm}^{-2}$ )	$R_{ct1}$ ( $\Omega \text{ cm}^2$ )	$Q_3$ ( $\text{F.s}^{\wedge} \text{ cm}^{-2}$ )	$C_{dl2}$ ( $\text{F cm}^{-2}$ )	$R_{ct2}$ ( $\Omega \text{ cm}^2$ )
1	Mg	$5.647 \pm 1.65$	0.4565	0.4729	$14.44 \pm 7.02$	0.2952	4.619	$10.13 \pm 5.10$
2	Mg-5Co	$7.650 \pm 2.50$	0.4550	0.4521	$17.45 \pm 8.12$	0.2842	4.213	$12.76 \pm 1.23$
3	Mg-10Co	$7.659 \pm 1.60$	0.4540	0.4489	$17.48 \pm 5.50$	0.2750	3.890	$13.21 \pm 3.25$
4	Mg-15Co	$1.240 \pm 0.50$	0.1732	0.2409	$35.16 \pm 6.00$	0.2598	0.014	$11.73 \pm 0.50$
5	Mg-20Co	$5.980 \pm 1.80$	0.1722	0.0205	$40.10 \pm 5.45$	0.2540	0.013	$08.01 \pm 5.60$
6	Mg-25Co	$7.462 \pm 1.45$	0.1697	0.0198	$42.50 \pm 2.15$	0.2359	0.013	$10.00 \pm 3.45$

#### 4. Conclusions:

The Mg-Co nanocomposites were synthesized by utilizing high energy ball mill and hydraulic compacting process. The wear and corrosion resistance of the composites are considered in different conditions.

- The wear analysis on a pin on disc apparatus shows Mg-25Co nanocomposite has healthier wear resistance and coefficient of friction.
- The potentiometric polarization analysis shows that the Mg-25Co nanocomposite has enhanced corrosion resistance due to the existence of Co nanoparticles.
- The electrochemical impedance spectroscopy (EIS) also authenticates that the Mg-25Co nanocomposite has higher charge transfer resistance value compared to that of pure Mg.
- The Microhardness of the Mg-25Co nanocomposite is superior to that of Pure Mg.
- From the findings of this study, it can be concluded that the Mg-25Co nanocomposite has better wear and corrosion resistance.

**References:**

- [1] J. Zhang, X. Zhang, Q. Liu, S. Yang, Z. Wang, Effects of Load on Dry Sliding Wear Behavior of Mg–Gd–Zn–Zr Alloys, *J. Mater. Sci. Technol.* 33 (2017) 645–651. doi:10.1016/j.jmst.2016.11.014.
- [2] H. Sharifi, K. Ostovan, M. Tayebi, A. Rajaei, Dry sliding wear behavior of open-cell Al-Mg/Al<sub>2</sub>O<sub>3</sub> and Al-Mg/SiC-Al<sub>2</sub>O<sub>3</sub> composite preforms produced by a pressureless infiltration technique, *Tribol. Int.* 116 (2017) 244–255. doi:10.1016/j.triboint.2017.07.023.
- [3] K.K. Ajith Kumar, U.T.S. Pillai, B.C. Pai, M. Chakraborty, Dry sliding wear behaviour of Mg-Si alloys, *Wear.* 303 (2013) 56–64. doi:10.1016/j.wear.2013.02.020.
- [4] J. Dai, X. Zhang, Q. Yin, S. Ni, Z. Ba, Z. Wang, Friction and wear behaviors of biodegradable Mg-6Gd-0.5Zn-0.4Zr alloy under simulated body fluid condition, *J. Magnes. Alloy.* 5 (2017) 448–453. doi:10.1016/j.jma.2017.11.002.
- [5] K. Soorya Prakash, P. Balasundar, S. Nagaraja, P.M. Gopal, V. Kavimani, Mechanical and wear behaviour of Mg–SiC–Gr hybrid composites, *J. Magnes. Alloy.* 4 (2016) 197–206. doi:10.1016/j.jma.2016.08.001.
- [6] F. Toptan, A.C. Alves, I. Kerti, E. Ariza, L.A. Rocha, Corrosion and tribocorrosion behaviour of Al-Si-Cu-Mg alloy and its composites reinforced with B<sub>4</sub>C particles in 0.05M NaCl solution, *Wear.* 306 (2013) 27–35. doi:10.1016/j.wear.2013.06.026.
- [7] M.E. Turan, Y. Sun, Y. Akgul, Mechanical, tribological and corrosion properties of fullerene reinforced magnesium matrix composites fabricated by semi powder metallurgy, *J. Alloys Compd.* 740 (2018) 1149–1158. doi:10.1016/j.jallcom.2018.01.103.
- [8] M.S. Kabir, T.I. Minhaj, M.D. Hossain, A. Kurny, Effect of Mg on the Wear Behaviour of as-cast Al-4.5Cu-3.4Fe in-situ Composite, *Am. J. Mater. Eng. Technol.* 3 (2015) 7–12.

- 1  
2  
3 doi:10.12691/MATERIALS-3-1-2.  
4  
5  
6 [9] F. Ren, W. Zhu, K. Chu, Fabrication and evaluation of bulk nanostructured cobalt  
7 intended for dental and orthopaedic implants, *J. Mech. Behav. Biomed. Mater.* 68 (2017)  
8 115–123. doi:10.1016/j.jmbbm.2017.01.039.  
9  
10  
11  
12 [10] R. Ma, S. Ju, H. Chen, C. Shu, Effect of Cobalt Content on Microstructures and Wear  
13 Resistance of Tungsten Carbide-Cobalt-Cemented Carbides Fabricated by Spark Plasma  
14 Sintering, *IOP Conf. Ser. Mater. Sci. Eng.* 207 (2017). doi:10.1088/1757-  
15 899X/207/1/012019.  
16  
17  
18  
19  
20  
21 [11] G. Manivasagam, D. Dhinasekaran, A. Rajamanickam, Biomedical Implants: Corrosion  
22 and its Prevention - A Review, *Recent Patents Corros. Sci.* 2 (2010) 40–54.  
23 doi:10.2174/1877610801002010040.  
24  
25  
26  
27  
28 [12] L.M. Vilhena, C.M. Fernandes, E. Soares, J. Sacramento, A.M.R. Senos, A. Ramalho,  
29 Abrasive wear resistance of WC-Co and WC-AISI 304 composites by ball-cratering  
30 method, *Wear.* 346–347 (2016) 99–107. doi:10.1016/j.wear.2015.11.005.  
31  
32  
33  
34  
35 [13] Y. Liu, J. Cheng, B. Yin, S. Zhu, Z. Qiao, J. Yang, Study of the tribological behaviors and  
36 wear mechanisms of WC-Co and WC-Fe<sub>3</sub>Al hard materials under dry sliding condition,  
37 *Tribol. Int.* 109 (2017) 19–25. doi:10.1016/j.triboint.2016.12.023.  
38  
39  
40  
41  
42 [14] N. Elkhoshkhany, A. Hafnway, A. Khaled, Electrodeposition and corrosion behavior of  
43 nano-structured Ni-WC and Ni-Co-WC composite coating, *J. Alloys Compd.* 695 (2017)  
44 1505–1514. doi:10.1016/j.jallcom.2016.10.290.  
45  
46  
47  
48  
49 [15] H.W. Liu, X.J. Xu, M.H. Zhu, P.D. Ren, Z.R. Zhou, High temperature fretting wear  
50 behavior of WC<sub>25</sub>Co coatings prepared by D-gun spraying on TiAlZr titanium alloy,  
51 *Tribol. Int.* 44 (2011) 1461–1470. doi:10.1016/j.triboint.2011.01.002.  
52  
53  
54  
55  
56  
57  
58  
59  
60

- 1  
2  
3 [16] X. Zhang, J. Ma, J. Yang, Q. Bi, W. Liu, Dry-sliding tribological behaviour of Fe–28Al–  
4 5Cr/TiC composites, *Wear*. 271 (2011) 881–888. doi:10.1016/j.wear.2011.03.020.  
5  
6  
7  
8 [17] C. Jiang, Y. Xing, F. Zhang, J. Hao, Microstructure and corrosion resistance of Fe/Mo  
9 composite amorphous coatings prepared by air plasma spraying, *Int. J. Miner. Metall.*  
10 *Mater.* 19 (2012) 657–662. doi:10.1007/s12613-012-0609-z.  
11  
12  
13  
14 [18] R. Mousavi, M.E. Bahrololoom, F. Deflorian, Preparation, corrosion, and wear resistance  
15 of Ni-Mo/Al composite coating reinforced with Al particles, *Mater. Des.* 110 (2016) 456–  
16 465. doi:10.1016/j.matdes.2016.08.019.  
17  
18  
19  
20 [19] L. Zhang, X. Qu, B. Duan, X. He, M. Qin, Effect of porosity on wear resistance of SiC p /  
21 Cu composites prepared by pressureless infiltration, *Trans. Nonferrous Met. Soc. China.*  
22 18 (2008) 1076–1082. doi:10.1016/S1003-6326(08)60184-3.  
23  
24  
25  
26 [20] M.G. Verón, F.C. Gennari, G.O. Meyer, Role of MgCo compound on the sorption  
27 properties of the Mg-Co milled mixtures, *J. Power Sources.* 195 (2010) 546–552.  
28 doi:10.1016/j.jpowsour.2009.07.047.  
29  
30  
31  
32 [21] E.M. Kirkpatrick, D.L. Leslie-Pelecky, S.H. Kim, R.D. Rieke, Magnetic and structural  
33 properties of Mg–Co nanostructures fabricated by chemical synthesis, *J. Appl. Phys.* 85  
34 (1999) 5375–5377. doi:10.1063/1.369982.  
35  
36  
37  
38 [22] W.R. Osório, L.C. Peixoto, P.R. Goulart, A. Garcia, Electrochemical corrosion parameters  
39 of as-cast Al-Fe alloys in a NaCl solution, *Corros. Sci.* 52 (2010) 2979–2993.  
40 doi:10.1016/j.corsci.2010.05.011.  
41  
42  
43  
44 [23] M. Hosseini, L. Fotouhi, A. Ehsani, M. Naseri, Enhancement of corrosion resistance of  
45 polypyrrole using metal oxide nanoparticles: Potentiodynamic and electrochemical  
46 impedance spectroscopy study, *J. Colloid Interface Sci.* 505 (2017) 213–219.  
47  
48  
49  
50  
51  
52  
53  
54  
55  
56  
57  
58  
59  
60



- doi:10.1016/j.jcis.2017.05.097.
- [24] W.X. Zhang, Z.H. Jiang, G.Y. Li, Q. Jiang, J.S. Lian, Electroless Ni-Sn-P coating on AZ91D magnesium alloy and its corrosion resistance, *Surf. Coatings Technol.* 202 (2008) 2570–2576. doi:10.1016/j.surfcoat.2007.09.023.
- [25] J.F. Marco, a C. Agudelo, J.R. Gancedo, D. Hanzel, Corrosion resistance of single TiN layers, Ti/TiN bilayers and Ti/TiN/Ti/TiN multilayers on iron under a salt fog spray (phohesion) test: an evaluation of XPS, *Surf. Interface Anal.* 27 (1999) 71–75. doi:10.1002/(SICI)1096-9918(199902)27:2<71::AID-SIA469>3.3.CO;2-G.
- [26] J. Yuan, X. Luan, R. Riedel, E. Ionescu, Preparation and hydrothermal corrosion behavior of C<sub>f</sub>/SiCN and C<sub>f</sub>/SiHfBCN ceramic matrix composites, *J. Eur. Ceram. Soc.* 35 (2015) 3329–3337. doi:10.1016/j.jeurceramsoc.2014.12.009.
- [27] R. Liu, J. Yao, Q. Zhang, M.X. Yao, R. Collier, Effects of molybdenum content on the wear/erosion and corrosion performance of low-carbon Stellite alloys, *Mater. Des.* 78 (2015) 95–106. doi:10.1016/j.matdes.2015.04.030.
- [28] S.A. Umoren, Y. Li, F.H. Wang, Influence of iron microstructure on the performance of polyacrylic acid as corrosion inhibitor in sulfuric acid solution, *Corros. Sci.* 53 (2011) 1778–1785. doi:10.1016/j.corsci.2011.01.052.
- [29] A. Ehsani, M.G. Mahjani, M. Hosseini, R. Safari, R. Moshrefi, H. Mohammad Shiri, Evaluation of *Thymus vulgaris* plant extract as an eco-friendly corrosion inhibitor for stainless steel 304 in acidic solution by means of electrochemical impedance spectroscopy, electrochemical noise analysis and density functional theory, *J. Colloid Interface Sci.* 490 (2017) 444–451. doi:10.1016/j.jcis.2016.11.048.
- [30] E. Angelini, S. Grassini, F. Rosalbino, F. Fracassi, R. D'Agostino, Electrochemical

1  
2  
3 impedance spectroscopy evaluation of the corrosion behaviour of Mg alloy coated with  
4 PECVD organosilicon thin film, *Prog. Org. Coatings*. 46 (2003) 107–111.  
5  
6 doi:10.1016/S0300-9440(02)00217-5.  
7  
8

- 9  
10 [31] E. Kowsari, S.Y. Arman, M.H. Shahini, H. Zandi, A. Ehsani, R. Naderi, A.  
11 PourghasemiHanza, M. Mehdipour, In situ synthesis, electrochemical and quantum  
12 chemical analysis of an amino acid-derived ionic liquid inhibitor for corrosion protection  
13 of mild steel in 1M HCl solution, *Corros. Sci.* 112 (2016) 73–85.  
14  
15  
16  
17  
18  
19  
20  
21  
22  
23  
24  
25  
26  
27  
28  
29  
30  
31  
32  
33  
34  
35  
36  
37  
38  
39  
40  
41  
42  
43  
44  
45  
46  
47  
48  
49  
50  
51  
52  
53  
54  
55  
56  
57  
58  
59  
60



## World Journal of Engineering

Simulation of Mushy State Solidification in Stir Casting  
SIJO M T, Jayadevan K R, Sheeja janardhanan,

### Article information:

To cite this document:

SIJO M T, Jayadevan K R, Sheeja janardhanan, "Simulation of Mushy State Solidification in Stir Casting", World Journal of Engineering, <https://doi.org/10.1108/WJE-04-2017-0079>

Permanent link to this document:

<https://doi.org/10.1108/WJE-04-2017-0079>

Downloaded on: 18 January 2018, At: 22:30 (PT)

References: this document contains references to 0 other documents.

To copy this document: [permissions@emeraldinsight.com](mailto:permissions@emeraldinsight.com)

The fulltext of this document has been downloaded 3 times since 2018\*

Access to this document was granted through an Emerald subscription provided by emerald-srm:333301 []

### For Authors

If you would like to write for this, or any other Emerald publication, then please use our Emerald for Authors service information about how to choose which publication to write for and submission guidelines are available for all. Please visit [www.emeraldinsight.com/authors](http://www.emeraldinsight.com/authors) for more information.

### About Emerald [www.emeraldinsight.com](http://www.emeraldinsight.com)

Emerald is a global publisher linking research and practice to the benefit of society. The company manages a portfolio of more than 290 journals and over 2,350 books and book series volumes, as well as providing an extensive range of online products and additional customer resources and services.

Emerald is both COUNTER 4 and TRANSFER compliant. The organization is a partner of the Committee on Publication Ethics (COPE) and also works with Portico and the LOCKSS initiative for digital archive preservation.

\*Related content and download information correct at time of download.

# Simulation of Mushy State Solidification in Stir Casting

Sijo M T<sup>a</sup>, K R Jayadevan<sup>a</sup> and Sheeja Janardhanan<sup>b</sup>

<sup>a</sup> Faculty of Engineering, Department of Mechanical, Government Engineering College Thrissur, Affiliated to Calicut University, Kerala, India,

<sup>b</sup> Faculty of Engineering, Department of Mechanical, SSET, Karukutty, Kerala, India

## Abstract

**Purpose** – Stir casting is a promising technique for the manufacture of aluminium silicon carbide metal matrix composites. The clustering of reinforcement particles is a serious concern in this production method. In this work, mushy state solidification characteristics in stir casting are numerically simulated using computational fluid dynamics (CFD) techniques to study the clustering of reinforcement particles.

**Design/methodology/approach** – Among Effect of process parameters on the distribution of particles are examined by varying stirrer speed, volume fraction of reinforcement, number of blades on stirrer, and diameter ratio (ratio of crucible diameter to stirrer diameter). Further, investigation on characteristics of cooling curves during solidification process is also carried out. Volume of fluid (VOF) method in conjunction with a solidification model is employed to simulate the multi-phase fluid flow during the mushy state of solidification. Solidification patterns thus obtained clearly indicate a strong influence of process parameters on the distribution of reinforcement particles and solidification time.

**Findings** – From the simulation study it is observed that increase in stirrer speed from 50rad/sec to 150rad/sec promotes faster solidification rate. But beyond 100rad/sec stirrer speed limit clustering of reinforcement particles is observed. The clustering of reinforcement particles are seen when volume fraction of reinforcement is increased beyond 10%. When number of blades on stirrer are increased from 3 blade to 5 blade geometry an increase in solidification rate is observed, also an uneven distribution of reinforcement particles are observed for 5 blade geometry. It is also seen from the simulation study that four blade stirrer gives a better distribution of reinforcement in the molten metal. Decrease in diameter ratio from 2.5 to 1.5 promotes faster solidification rate.

**Originality/value** – There is 90% closeness in results for simulation study and the published experimental results.

**Keywords** Aluminium silicon carbide metal matrix composites, Stir casting, Numerical Simulation, CFD, VOF

**Paper type** Research paper

## 1. Introduction

Enhancement in properties of engineering materials has always been the target of scientists over many years. This led to the discovery of new category of materials called composite materials; composed of a combination of distinctly different two or more constituents that differ in the form of composition and they are insoluble in each other. Such types of material are developed to enhance mechanical properties which cannot be otherwise expected from conventional materials. Aluminium silicon carbide metal matrix composites (Al-SiC MMC) possess a wide range of physical and mechanical properties such as high strength, stiffness, low density, corrosion resistance, wear resistance, good thermal and damping properties, which allow them to be used in challenging as well as demanding applications like aerospace, aircrafts, automobile, marine applications, turbines blades, brake pads etc (Surappa, 2003).

Among various manufacturing methods stir casting is generally accepted as a promising route because of its low cost and little damage to reinforcement (Hashim *et al.*, 1999). Moreover, stir-cast components are not restricted by its size and shape. It also possesses advantages of simplicity, flexibility and applicability to large quantity production. However, a major concern associated with the stir casting process is the segregation of reinforcing particles resulting from surfacing or settling of reinforcement particles during melting and casting process (Naher *et al.*, 2005). Moreover, stir casting process involves complex physical phenomena like particle incorporation into the liquid melt, chemical reactions and clustering of particles (Hashim *et al.*, 1999). Devi *et al.*, 2012 observed that distribution of the reinforcement particles is dependent on the solidification rate and at low solidification rates, the reinforcing particles are clustered. Before the occurrence of complete solidification of Al melt, it will pass through a semisolid state called mushy state (Feller and Beckermann, 1997). Once the mushy state is reached the reinforcement particles remain in their positions during solidification (Feller and Beckermann, 1997). Once inside the mush, macroscopic particle motion is largely prevented by the presence of microscopically complex solid liquid interfaces called dendrites, which entrap the particles (Feller and Beckermann, 1997). Hashim, 1999 experimentally found that the microstructure of rapidly solidified composite has finer dendrite size and this permits fewer reinforcement particles to be segregated giving a more homogeneous particle distribution. Lie *et al.*, 2010 conducted

experiments to study the microstructure of MMCs and it is found that at higher speed of rotation, particles are homogeneously distributed. It is also observed that shear rate is directly dependent on stirrer speed, diameter of stirrer and gap between crucible and stirrer. [Singla et al., 2009](#) experimentally verified that particle distributions in the matrix strongly depend on the stirring speed, viscosity of slurry, minimizing of gas entrapment etc. [Gore and Crowe, 1989](#) observed that when reinforcement particles are small compared with turbulent length scale, it tends to follow the turbulent fluid motion. On the other hand, large particles do not follow the turbulent motions and particles tend to be accumulating in the shear zones. Another problem associated with stir casting process is the improper wettability of reinforcement in matrix. Wettability can be defined as the ability of a liquid to spread on a solid surface. It also indicates the extent of contact between a liquid and a solid. [Reddy and Zitoun, 2010](#) showed that addition of magnesium (Mg) improves the wettability between Al and SiC particles by reducing the SiO<sub>2</sub> layer on the surface of the SiC. However, increase in Magnesium (Mg) content above 1% weight increases viscosity of slurry, and hence, uniform particle distribution becomes difficult. So in order to obtain metal matrix composite with good quality characteristics, manufacturing methods used for production of MMCs should ensure uniform distribution of reinforcement in matrix. Since stir casting process involves a number of parameters, their effective strategy of experimentation is difficult and expensive.

From the survey of a wide range of allied literature, it is clear that uniform distribution of particles depends upon on material properties such as strength, hardness and process parameters such as the wetting of the particles with the melt, strength of mixing, relative density, and rate of solidification. The distribution of the particles in the molten matrix also depends on the geometry of the mechanical stirrer, stirring parameters, position of the mechanical stirrer in the melt, melting temperature and the characteristics of the particles added. The real time measurement of the flow characteristics during stir casting is very expensive, time-consuming and potentially hazardous to the foundry personnel. These factors make the flow studies quite complex and impossible. A large scale crucible is often used for stir casting in the industrial production. But the effect of scale-up to the industrial sized unit is not well-established. Further achieving uniform distribution of reinforcement in such a large scale crucible is yet a matter of concern. The stir casting process is generally conducted in a closed crucible, in which the flow pattern is imperceptible. Also the experimental work to find out cooling curve for the composite is very difficult and costly. The analysis of cooling curves provides valuable information on the effect of the particles on solidification events. Cooling curve analysis has been effectively used to determine the occurrence of various phases during the solidification of nonferrous alloys ([Wu et al., 2002](#)). The cooling curve shows the eutectic solidification time (i.e. the time interval between the start of primary aluminum phase nucleation and the end of the eutectic phase solidification), which is a measure of solidification rate. Temperature changes occur in alloys cooling curve by the latent heat of transformation released during solidification. Analysis of these characteristics parameter permits the foundry man to monitor, regulate and optimize the melt chemistry even before an actual casting is made. Researchers have used K type thermocouples, which is connected to mould material to study the cooling curves for MMC and found that the addition of ceramic reinforcement to alloy enhances the eutectic solidification time ([Behra et al., 2011](#)). But these experimental results do not provide any temperature information inside the crucible containing molten matrix. Moreover, experimental methods do not provide a clear understanding of the solidification process as it is highly dangerous to handle high temperature molten metal manually. Therefore, numerical simulation is a powerful tool to guide the experimental research.

[Naher et al., 2003](#) conducted a simulation study, in which they used a water-glycerol mixture to model MMC production by stir casting. The viscosity of the water glycerol mixture was made equivalent to that of molten aluminum. Uniform dispersion time was measured for different values of stirring speed, blade geometry and stirrer height. They found that higher blade angle and stirring speed, and lower viscosity of the fluid decrease the time for uniform dispersion. The major shortcoming of the simulation work was that it did not address solidification of the melt. [Su et al., 2010](#) studied the effects of some important stirring process parameters, such as the blade angle, rotating speed, the diameter of the impeller, and the stirrer geometry, on the flow characteristics of the molten matrix. The simulation results show that the process parameters have significant effects on the flow behavior of the fluid in the stirred crucible. [Zagorski and Golak, 2013](#) carried out computer simulation of gravity casting of the metal matrix composites reinforced with ceramics using ANSYS FLUENT. Their numerical model describes the process taking into account solidification and its influence on the distribution of reinforcement particles.

Recently, [George et al., 2015](#) modeled mushy state of solidification process of Al-SiC MMC's by treating Al- SiC as a single phase material. However, in stir casting, the centrifugal force acting on the fluids will tend to separate the fluids. Accurate modeling of these phenomena requires a multi phase model approach.

Five of the most popular multi phase models are Dispersed or Discrete Phase Model (DPM), Volume of fluid (VOF) model, Eulerian Multiphase Model (EMM), Eulerian Granular Multiphase Model (EGMM), and Algebraic Slip Mixture (ASM) Model. Among these methods, VOF Model is designed for two or more immiscible fluids. [Hirt and Nicholas, 1981](#) used VOF method to study the dynamics of free boundaries. It is also found that VOF method uses a minimum of stored information and can be readily extended to three dimensional calculations. [Tang et al., 2004](#) used VOF method to investigate the hydrodynamic behavior of immiscible metallic alloys in rheomixing, based on the use of a twin screw extruder. The numerical results show good qualitative agreement with experimental results. They also compared different Eulerian multi phase models available and found that among various models VOF model is the most successful approach to capture the

analysis of two fluid systems under an imposed force. [Andras et al., 2009](#) used CFD simulations of bubble columns using the VOF model. They observed that VOF method is capable of describing the phase distribution of completely immiscible gas and liquid phases using a finite volume method. Further, it was shown that with less computational cost VOF method leads to accurate results. [Johansson, 2011](#) carried out interface tracking of multiphase flow using volume of fluid method which uses a color function. The interface was reconstructed by implicit as well as explicit methods. A Realizable k- $\epsilon$  with standard wall function for modeling turbulence was employed. The research showed that the important parameters in simulation are the mesh size and time step size ([Johansson, 2011](#)). Also implicit volume of fluid (VOF) discretization method is much more stable than explicit VOF. [Nguyen and Huang, 2012](#) studied mixing of lead in air for which VOF integrated with a solidification model in FLUENT was used. Since stir casting process involves multi phase flow (molten matrix and reinforcement particles) together with solidification of molten matrix, VOF model in conjunction with a solidification model can be effectively implemented.

A comparison of experimental work in this field shows an optimum stirrer speed range of 60 rad/sec to 90 rad/sec to obtain uniform particle distribution and to have optimum mechanical properties ([Naher et al., 2007](#); [Bhusan and Kumar, 2011](#); [Arulraj et al., 2017](#); [Prabhu et al., 2006](#); [Dhanalakshmi et al., 2005](#)). Various experimental work to study the effect of volume fraction on particle distribution reveals that for 10% volume fraction of reinforcement better distribution of particles are obtained. Addition of volume fractions more than 10% reinforcement, promotes clustering of particles, which in turn degrade the mechanical properties ([Naher et al., 2007](#); [Bhusan and Kumar, 2011](#); [Saravanakumar et al., 2016](#); [Zhang et al., 2008](#)). To study the effect of number of blades on stirrer shows that effective number of blades on stirrer should be equal to four. Number of blades more than four on stirrer produces a decrease in solidification rate ([Almadhoni and Khan, 2015](#)). Moreover, an increase in diameter ratio also produces a decrease in solidification rate ([Lie et al., 2010](#)).

The experimental methods to study mushy solidification pattern and cooling curve analysis of stir casting process are difficult and sparse and the research towards the same is at its infancy. The present work aims towards developing a simulation method which will consider all relevant process parameters. The novelty of this research work lies in simultaneous variation of all relevant process parameter which is the main limitation of the previous research work in this field is being explored in this work so that interaction between process parameters can be studied. In this paper, numerical simulation of mushy state characteristics and cooling curve analysis of stir casting process have been done using CFD solver FLUENT by varying relevant process parameters such as stirrer speed, volume fraction of reinforcement, diameter ratio, and number of blades. Contour plots of mushy state solidification pattern and cooling curve characteristics obtained from simulation study are examined to find the effect of process parameters. The results show a strong influence of process parameters on clustering of reinforcement particles. Further, this work demonstrates the capability of CFD in the field of manufacturing and paves path for immense future research.

## 2. Modeling and simulation

Stir casting process is considered as a case of mixing of fluids with external stirring ([Gore and Crowe, 1989](#)). The fundamental physics involved in stir casting process are multiphase fluid flow, heat transfer, turbulence and solidification.

### 2.1. Theory

Fluid flow in stir casting obeys fundamental conservation equations of mass and momentum. Any fluid flow based on the value of the Reynolds number, can be classified into laminar flow having small Reynolds numbers and turbulent flow having high Reynolds numbers. Since mixing of fluids in stir casting involves turbulence flow, which gives rise to fluctuation in mean velocity (let be the fluctuating  $i^{\text{th}}$  component of fluid velocity) and other variables. This effect can be effectively incorporated into the CFD model by introducing a turbulence term into Navier Stokes equation. This is achieved by a process called time averaging of conservative equations. After time averaging over many cycles of fluctuation, terms containing factors of the fluctuating component average to zero. The final equation after time averaging, called Reynolds Averaged Navier Stokes (RANS) equation is given by

$$\frac{\partial(\rho u)}{\partial t} + \frac{\partial(\rho u u)}{\partial x_j} = -\frac{\partial p}{\partial x_i} + \frac{\partial}{\partial x_j} \left[ \mu \frac{\partial u}{\partial x_j} + \rho \overline{u' u'} \right] + \rho g_i + F_i \quad (1)$$

The new term containing  $\rho \overline{u' u'}$  is called Reynolds stress. There are several turbulence models available to compute the Reynolds stress. The popular turbulence models in use today are the k- $\epsilon$  Model, RNG k- $\epsilon$ , Realizable k- $\epsilon$ , RSM, and LES. Among these, the k- $\epsilon$  model is highly robust, meaning that it is computationally stable even in the presence of other more complex physics. Its main advantages are rapid and stable calculation, and reasonable results for many flows, especially those with high Reynolds number. This model adds two additional terms turbulence kinetic energy (k) and rate of dissipation of turbulence ( $\epsilon$ ). The solution of k and  $\epsilon$  is used to find Reynolds stress and it is substituted in to the momentum equation, to solve for velocity components.

Solidification and melting in stir casting involves heat transfer phenomena, which is often expressed as an equation for the conservation of energy, represented by

$$\frac{\partial(\rho H)}{\partial t} + \nabla \cdot (\rho \bar{u} H) = \nabla \cdot (K \nabla T) + S \quad (2)$$

In the above equation, H is the enthalpy,  $\bar{u}$  is the fluid velocity, K is the thermal conductivity and S is a source or a sink term. Enthalpy (H) of the material is the sum of sensible enthalpy (h) and latent heat ( $\Delta H$ ). The sensible enthalpy is given by

$$h = h_{ref} + \int_{T_{ref}}^T C_p dT \quad (3)$$

Here,  $h_{ref}$  is the reference enthalpy,  $T_{ref}$  is the reference temperature and  $C_p$  is the specific heat at constant pressure. Latent heat during solidification is computed as:

$$\Delta H = \beta L \quad (4)$$

Here,  $\beta$  is the liquid fraction, which indicates the fraction of the cell volume that is in liquid form and L is the latent heat of the material. The liquid fraction ( $\beta$ ) value is used for modeling the solidification and melting process. The liquid fraction during solidification is computed as:

$$\left. \begin{aligned} \beta &= 0 && \text{if } T < T_{solidus} \\ \beta &= 1 && \text{if } T > T_{liquidus} \\ \beta &= \frac{T - T_{solidus}}{T_{liquidus} - T_{solidus}} && \text{if } T_{solidus} < T < T_{liquidus} \end{aligned} \right\} \quad (5)$$

In the mushy zone the liquid fraction lies between 0 and 1. The temperature is solved by iterating between the energy Equation (2), Equation (4) and Equation set (5).

Two sink terms are to be considered while modeling solidification process. First one is called momentum sink term, which is due to reduction in porosity when material inside the crucible reaches mushy zone (semi solid state). This is given by

$$S = \left( \frac{1 - \beta^2}{\beta^2 + \varepsilon} \right) A_{mush} (v - v_p) \quad (6)$$

where  $v$  is the pull velocity,  $v_p$  is the mushy zone constant and  $\varepsilon$  is a constant.

The second sink term is added to the turbulence equation in the mushy and solidified zones to account for the presence of solid matter, which is given by

$$S = \left( \frac{1 - \beta^2}{\beta^2 + \varepsilon} \right) A_{mush} \phi \quad (7)$$

where  $\phi$  is the turbulence quantity being solved for.

The differential equations presented in this section describe the continuous movement of a fluid in space and time. To be able to numerically solve these equations, all aspects of the process need to be discretized. Several numerical methods have been employed over the years to solve Navier-Stokes equations, namely finite difference, finite element, spectral element method etc. The result of the discretization process is a finite set of coupled algebraic equations that need to be solved simultaneously in every cell in the solution domain. Because of the non-linearity of the equations that govern the fluid flow and related processes, an iterative solution procedure is required. Out of available methods a segregated solution approach solves one variable at a time throughout the entire domain. This approach is popular for incompressible flows with complex physics, typical of those found in mixing applications. Iteration of the solution will be completed only after each variable has been solved. Generally, a guessed pressure field is used in the solution of the momentum equation to get new velocities which may not satisfy the continuity equation and energy equation. So corrections to the velocities are determined. Based on the velocity corrections a pressure correction is computed which, when added to the original guessed pressure results in an updated pressure, and the entire process is repeated until convergence criteria are met (Marshall and Bakker, 2003).

## 2.2 Simulation

In the present work, flow field developed due to stirring action is simulated. For each simulation trail, process parameters varied are diameter ratio (DR = 1.5, 2, and 2.5), stirrer speed ( $\omega = 50\text{rad/sec}$ ,  $100\text{rad/sec}$  and  $150\text{rad/sec}$ ), volume fraction of reinforcement (VF = 10%, 20%, and 30%), and number of blades (NB = 3, 4, and 5).

### 2.2.1 Geometric modeling and meshing

Since a three dimensional work demands higher computational facilities and time, a two dimensional model of the crucible and the blade is considered. Geometric modeling and meshing is carried out using ANSYS ICEM CFD. The crucible diameter is chosen as 60 mm, and the wall thickness as 5 mm. The stirrer blade lengths are chosen as 30 mm, 20 mm and 14 mm so as to get diameter ratios of 1.5, 2, and 2.5 respectively. The width of the blade is taken as 2 mm. These blades are connected to an inner circular rotor (stirrer) of 20 mm diameter. The space between crucible and stirrer blade, which is filled by molten aluminium and silicon carbide particles is the domain for analysis. For the discretization of the domain, an unstructured mesh with triangular elements is used. After conducting mesh sensitivity study (Figure 1), a mesh having 26200 triangular elements has been chosen for the present study. It was seen that the parameters attain a constant value even if the mesh size exceeds 26200 elements. A schematic representation of stir casting setup is depicted in Figure 2. The mesh imported to the FLUENT software is shown in Figure 3.

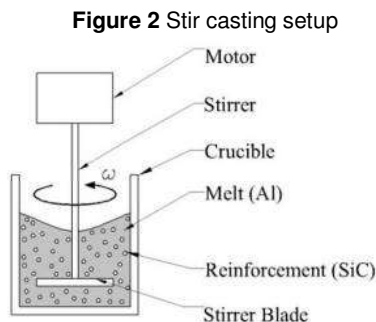
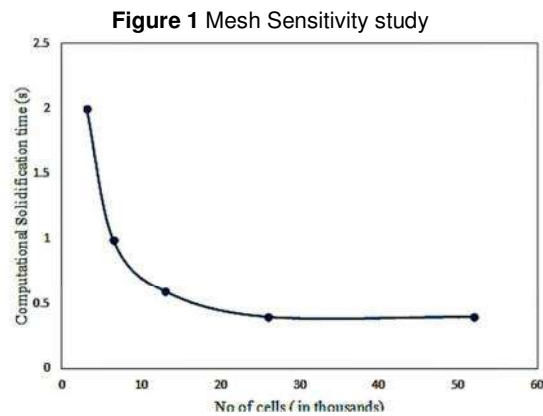
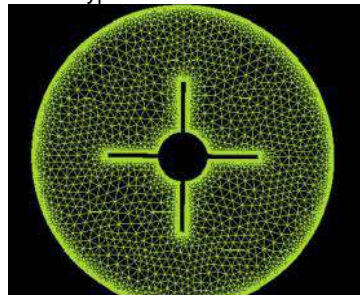


**Figure 3 A typical two dimensional mesh**



### 2.2.2 Assumptions

The assumptions used to create the simulation model are stated below.

- Size of the Silicon carbide particles are assumed to be small so that it flows like a fluid (Gore and Crowe, 1989).
- Reinforcement particles are initially assumed to be concentrated in a region surrounded by stirrer.
- Stirrer and crucible are made of cast steel to act as a solid wall.
- Fluids are treated as Newtonian fluids.
- Interfaces have vanishing thickness.
- Initial temperature of the system is assumed to be  $930^{\circ}\text{C}$ .

### 2.2.3 Boundary conditions

Thermal boundary conditions are incorporated via system coupling. No slip occurs inside the crucible. The contact resistance is taken as  $0.001\text{m}^2\text{-K/W}$  for crucible wall and blade. The properties of the materials selected for simulation study are shown in Table I (George *et al.*, 2015). The properties in any given cell are either purely representative of one of the phases, or representation of a mixture of the phases, depending upon the volume fraction values.



Table I Material Properties

Properties	Aluminium	Silicon carbide	Cast steel
Density(kg/m <sup>3</sup> )	2720	3210	7200
Specific Heat(J/kg-K)	963	750	500
Thermal Conductivity(W/m-K)	170	120	23.2
Viscosity(kg/m-s)	$1.4 \times 10^{-3}$	$1 \times 10^{-3}$	N/A
Molecular weight(kg/kgmol)	26.891	40.11	N/A
Standard state enthalpy(J/kgmol)	$3.29 \times 10^8$	$7.19 \times 10^8$	N/A
Reference Temperature(K)	900	900	N/A
Pure solvent Melting heat(J/kg)	$4 \times 10^5$	$3.6 \times 10^5$	N/A
Solidus temperature(K)	865	1700	N/A
Liquidus temperature(K)	925	2500	N/A

### 2.2.4 Solution method

The discretization of the equations explained in section 2 is done using finite volume method. Since all problem variables are stored at the cell center, the face values need to be expressed in terms of cell center values. Among different schemes available for this, a second order upwind differencing scheme is used because it will reduce the numerical error in the final solution. Also during stirring action, convection dominates diffusion as a result of which the Peclet number is high. Peclet number is the ratio of the thermal energy convected to the fluid to the thermal energy conducted within the fluid. The second order upwind scheme holds good for full range of Peclet number. The multiphase VOF model, enthalpy model, and solidification & melting model are enabled in the FLUENT with a mushy zone constant of 100000. The phases are selected in such a way that primary phase is aluminum and secondary phase is silicon carbide. To account for turbulence flow, a wall function in the near wall region is selected. This will avoid singularity at the wall for eddy dissipation. Calculations are carried out in a rotational frame of reference, rotating at a constant angular velocity. The solution is carried out in FLUENT using a two-dimensional, pressure-based, segregated and unsteady flow solver. The solution techniques include pressure velocity coupling scheme using SIMPLE, momentum and turbulent kinetic energy discretization using second order upwind scheme, and volume fraction discretization using Geo-reconstruct. All solution variables are initialized before the iteration. The solution process involves iterations wherein the entire set of governing equations is solved repeatedly until the solution converges. Finally, the results of mushy state solidification pattern and cooling curve characteristics are plotted using post processor.

## 3. Results and discussions

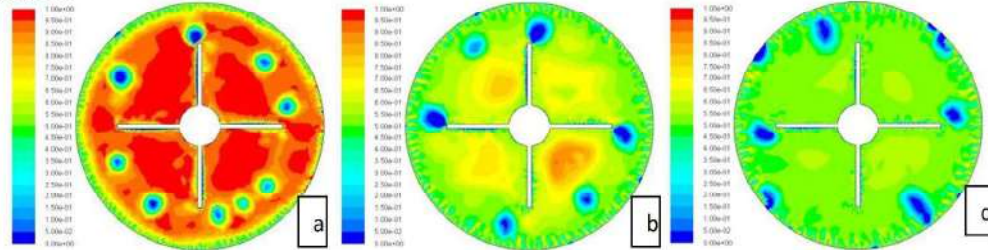
In this section, results obtained from simulation study are presented and discussed in detail. Mainly mushy state solidification pattern for various combinations of process parameters are shown. These solidification patterns for all the cases are generated at the same computational time of 0.4 sec. Further, cooling curve characteristics for various cases are also summarized.

### 3.1 Effect of stirrer speed

Mushy state solidification patterns corresponding to different stirrer speeds,  $\omega = 50, 100, \text{ and } 150 \text{ rad/sec}$  are shown in Figures 4(a) – 4(c), respectively. These results correspond to the case of diameter ratio 1.5, volume fraction 10%, and number of blades 4. In these figures, liquid fraction scale is shown on the left side of the solidification pattern. The continuous monitoring of solidification pattern of all simulation trials from the initial iteration, it was observed that there is directional solidification. Directional solidification indicates that solidification is beginning from boundary of the crucible and then it is propagating inwards to the center of the crucible. From Figures 4(a) - (c) it is clear that when speed increases from 50rad/sec to 150rad/sec the time taken to reach mushy state is not the same. From Figure 4(b) and 4(c) it is clear that molten metal has reached the mushy state but in Figure 4(a), there is concentration of molten metal at the center, which indicates that corresponding to stirrer speed 50rad/sec mushy state is not reached. It can also be seen from Figure 4a that molten metal is unevenly distributed which shows the degree of non uniformity in solidification process. Further, in Figure 4(c) reinforcement is concentrated at the circumference of the crucible, which is a measure of clustering tendency of reinforcement. But in Figures 4(a) and 4(b) uniform distribution of reinforcement particle is observed. From the simulation study it is inferred that stirrer speed has significant effect on solidification rate and clustering tendency. When stirring speed increases, turbulence and shear rate will increase which in turn accelerates the solidification rate because of stirring speed

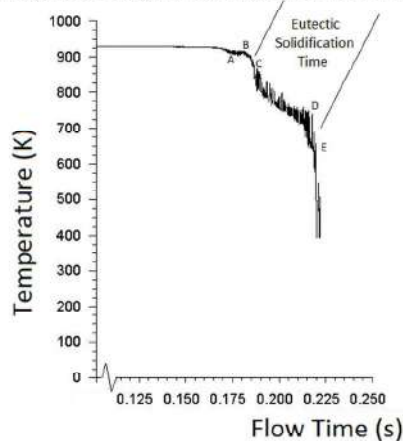
promotes binding between matrix and reinforcement. It also promotes formation of vortex which is responsible for dispersion of particulates in liquid metal. At the same time when it increases beyond certain limit solidification and distribution of reinforcement are affected adversely.

**Figure 4** Solidification pattern for 4blade, 10%SiC, DR = 1.5, and stirrer speeds (a) 50rad/sec (b) 100rad/sec (c) 150rad/sec



To study the effect of process parameters on cooling curve characteristic a typical cooling curve, corresponding to 4 blade stirrer, 10% volume fraction of SiC, stirrer speed of 100rad/sec and diameter ratio 1.5 is shown in Figure 5. Cooling curve's vertical axis show minimum temperature inside the crucible in degree Kelvin and horizontal axis show the computational flow time in seconds. In all simulation curves obtained there is an initial dip in the curve (point 'A' in Figure 5), which represents nucleation temperature of primary  $\alpha$  phase. Then it rises to a particular point 'B' called liquidus arrest temperature (Wu *et al.*, 2002). The difference between these two points shows the degree of liquidus under cooling. After liquidus arrest temperature the curve falls down to eutectic nucleation temperature followed by eutectic growth temperature (from point 'C' to point 'D') and finally to the end of eutectic reaction temperature (point 'E'). The information that can be gathered from the study is the extent of under cooling, which provides energy for creation new solid- liquid interface. Larger the extent of under cooling greater will be the number of nucleous formed. Also the area under cooling curve provides information about latent heat released during solidification process. The comparison of cooling curves of the composite for different process parameter combinations provides interesting information that may be useful to control composite's behavior during thermal treatment and final microstructure.

**Figure 5** A typical cooling curve for Al-SiC MMC



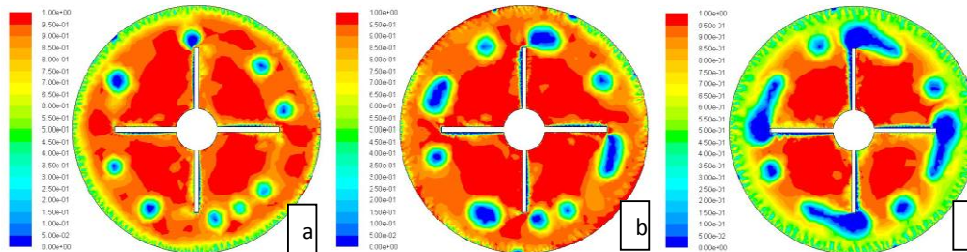
Cooling curve data for the same case with varying stirrer speed as in previous case are tabulated in Table II. It can be seen from these results that for 50rad/sec stirrer speed, the solidification starts very slowly but when speed is increased to 100rad/sec solidification starts early and when stirrer speed is increased to 150rad/sec, solidification starts much early. Hence, from Table II it is clear that with increase in stirrer speed the start of eutectic solidification time is reduced. Eutectic solidification time is low for 100rad/sec. There is a slight increase in eutectic solidification time for 150rad/sec which may be due to the over swirl produced by increase in speed beyond certain limit. These simulation results are well in accordance with the experimental results published. Dhanalakshmi *et al.*, 2016 conducted experimental study on particle incorporation revealed that highest amount of particles are entrapped and distributed uniformly at stirring speed range of 500 rpm to 550 rpm. At stirring speeds above 550 rpm, their microstructural study revealed the presence of pores and reinforcement particles surrounding these pores together with uneven distribution of reinforcement particles.

**Table II** Cooling Curve Characteristics for 4blade, 10%SiC, DR= 1.5 and different stirrer speeds

Stirrer speed, $\omega$ (rad/sec)	Solidification Starting time(sec)	Eutectic Solidification Starting time(sec)	Eutectic Solidification End time(sec)	Eutectic Solidification time(sec)
50	0.425	0.475	0.675	0.200
100	0.165	0.180	0.220	0.040
150	0.090	0.100	0.160	0.060

### 3.2 Effect of volume fraction

Mushy state solidification patterns corresponding to different volume fraction, VF =10%, 20%, and 30% are shown in Figures 6(a) – 6(c), respectively. These results correspond to the case of diameter ratio 1.5, stirrer speed,  $\omega=50$ rad/sec, and number of blades 4. In Figure 6(b) and 6(c) reinforcement particles are joined together and it is seen like a tree structure, which is a measure of reinforcement clustering. Figures 6(a) - (c) contains concentration of molten metal at the center, which show the mushy state is not reached. From Figures 6(a) – (c) it is evident that when volume fraction is increased from 10% to 30% there is a tendency for segregation or clustering of reinforcement particle. These simulation results clearly show a strong influence of volume fraction on clustering tendency but volume fraction has a less impact on solidification rate. These simulation results are in line with various literatures reviewed. Zhang *et al.*, 2008 found that when second phase particles added to matrix material then its solidification rate is affected. Also the clustering tendency of the delaminated particles increases with increase in volume fraction of SiC particles. Behra *et al.*, 2011 observed that during solidification if the local temperature is less than liquidus temperature a tree like structure is formed called dendrite structure. This dendrite structure formation is due to super cooling effect, which produce spikes into the super cooled regions and grow more rapidly than neighboring regions and these spikes reject the secondary particles, thus delaying freezing of the neighboring regions. Also these dendrite structure entraps the secondary particles thus promotes clustering tendency, which is seen in Figure 6(c). They also found that increasing the SiC particulate content tends to form  $Al_4C_3$  in the interface as a result the viscosity is increased and the fluidity of the melt composites reduced, which will produce uneven solidification. Reddy and Zitoun, 2010 found that at higher volume fractions and small size particles, the particle-particle interaction may develop clustering in the composite.

**Figure 6** Solidification Pattern for 4blade, 50rad/sec, diameter ratio 1.5 and volume fraction (a) 10% (b) 20% (c) 30%

Cooling curve data for these cases is presented in Table III. From Table III it is evident that the start of eutectic solidification time is delayed when volume fraction percentage is increased from 10% to 30%. Also duration of eutectic solidification time is observed low for 20% reinforcement. The delay in starting time of solidification is happened due to the presence of insulating particles. These results agree with experimental results. Hong *et al.*, 2003 observed that addition of ceramic reinforcement to alloy enhances the eutectic solidification time, due to the presence of insulating reinforcements. Also when volume fraction increases clustering tendency will increase.

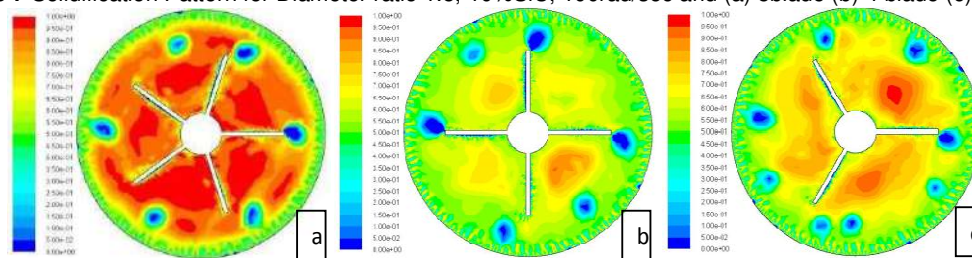
**Table III** Cooling Curve Characteristics for 4blade, 50rad/sec, DR= 1.5 and different volume fractions

Volume fraction VF (%)	Solidification Starting time(sec)	Eutectic Solidification Starting time(sec)	Eutectic Solidification End time(sec)	Eutectic Solidification time(sec)
10	0.425	0.475	0.675	0.200
20	0.550	0.600	0.700	0.100
30	0.700	0.800	0.975	0.175

### 3.3 Effect of number of blades

Mushy state solidification patterns corresponding to different number of blades NB =5, 4, and 3 are shown in Figures 7(a) – 7(c), respectively. These results correspond to the case of diameter ratio 1.5, stirrer speed,  $\omega = 100 \text{ rad/sec}$ , and volume fraction 10%. From Figures 7(a) - (c) it is seen that solidification patterns are not uniform, and there is a slight variation in solidification pattern. This shows that increase in number of blades has no considerable effect on solidification pattern and clustering phenomena. The presence of uneven molten metal in Figure 7(a) and 7(c) show that there is uneven solidification in 5 blade and 3 blade stirrer geometries. It is also inferred from Figure 7b that 4 blade stirrer will provide better solidification pattern compared with other two types of blade geometries. For 3 blade stirrer the turbulence produced is low and for 5 blade stirrer the turbulence produced is very high. Therefore, to have optimum turbulence the effective number of blades on stirrer should be 4. These simulation results are in line with various experimental works. The experimental results of various research studies to reduce the formation of vortex at the surface of the melt and to have uniform dispersion of material indicated that the blade angle should be  $30^\circ$  to  $90^\circ$ , and number of blade should be four (Almadhoni and Khan, 2015).

**Figure 7** Solidification Pattern for Diameter ratio 1.5, 10%SiC, 100rad/sec and (a) 5blade (b) 4 blade (c) 3 blade



Cooling curve data for these cases is presented in Table IV. From cooling curve analysis study, it is clear that when number of blades increases there is a decrease in starting time of solidification. From Table IV it is observed that the start of eutectic solidification time and eutectic solidification time are low for four blade geometry compared with other two types of blade geometry. It is also seen from the simulation study that 5 blade stirrer gives a low eutectic solidification duration compared with other two types of blade arrangements.

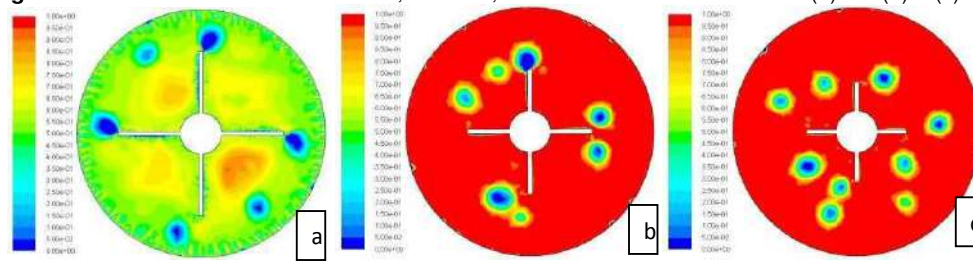
**Table IV** Cooling Curve Characteristics for DR= 1.5, 10%SiC, 100rad/sec and different number of blades

Stirrer speed, $\omega$ (rad/sec)	Solidification Starting time(sec)	Eutectic Solidification Starting time(sec)	Eutectic Solidification End time(sec)	Eutectic Solidification time(sec)
5	0.210	0.230	0.250	0.020
4	0.165	0.180	0.220	0.040
3	0.320	0.350	0.430	0.080

### 3.4 Effect of diameter ratio

Mushy state solidification patterns corresponding to different diameter ratio 1.5, 2, and 2.5 are shown in Figures 8(a) – 8(c), respectively. These results correspond to the case of number of blades 4, stirrer speed,  $\omega = 100 \text{ rad/sec}$ , and volume fraction 10%. From Figures 8(a) – (c) it is seen that when diameter ratio increases from 1.5 to 2.5 the concentration of molten metal is increased. The increase in diameter ratio retards the formation of mushy state. When diameter ratio is increased the turbulence decreases, which in turn reduces heat dissipation. It finally retards the solidification of the molten metal. These simulation results are in good agreement with the experimental results for the same crucible diameter. When diameter ratio increases turbulence and shear zone region inside the crucible will increase which in turn increases the solidification rate. The solidification rate is theoretically calculated using the formula  $r = \pi n(D/\delta - 2)$ , where  $n$  and  $D$  are the rotation speed and the outer diameter of the blade, respectively, and  $\delta$  is the gap between the blade and the inner surface of the crucible (Lei *et al.*, 2010). The above equation clearly shows the relationship between the gap ( $\delta$ ) and solidification rate ( $r$ ).

**Figure 8** Solidification Pattern for 4blade, 10%SiC, 100rad/sec and diameter ratio (a) 1.5 (b) 2 (c) 2.5



From Table V, which shows the cooling curve data for this case, it is clear that the start of eutectic solidification time increases with increase in diameter ratio. Duration of eutectic solidification time is high for diameter ratio 2 and a slight decrease in eutectic solidification time is observed for diameter ratio 2.5 and a faster solidification rate and faster eutectic solidification time are observed for diameter ratio 1.5.

**Table V** Cooling Curve Characteristics for 4blade, 10%SiC, 100rad/sec and for different diameter ratio

Diameter ratio (DR)	Solidification Starting time(sec)	Eutectic Solidification Starting time(sec)	Eutectic Solidification End time(sec)	Eutectic Solidification time(sec)
1.5	0.165	0.180	0.220	0.040
2	0.400	0.450	0.750	0.300
2.5	0.550	0.600	0.750	0.150

Comparing mushy state solidification patterns for all the cases it can be inferred that stirrer speed is the predominant factor compared with other parameters which directly influence the solidification rate. Further, volume fraction of reinforcement is the main factor which will directly depend upon clustering tendency compared with other process parameters. Also volume fraction has less effect on solidification rate and eutectic solidification time. Number of blades on stirrer and diameter ratio have significant effect on solidification rate but have less significant effect on clustering of secondary particles. It can also be inferred from the simulation result that stirrer speed, number of blades, and diameter ratio are having interaction effects. But volume fraction is an independent parameter which has less interaction with other process parameters. By comparing all simulation trial results, it is seen that 4 blade stirrer with diameter ratio 1.5, 10% SiC reinforcement and 100rad/sec stirrer speed shows faster solidification time and less clustering tendency (Figure 8a). The variation in the characteristics of the cooling curve always has a significant effect on the microstructure and mechanical behavior of the material (Behra *et al.*, 2011; Dehnavi *et al.*, 2015) From Table II through V it is clear that eutectic solidification time depends upon process parameters stirrer speed, volume fraction, diameter ratio and number of blades. Among these process parameters stirrer speed, volume fraction and diameter ratio are more predominant than the number of blades on stirrer.

#### 4. Scope for future work

In recent years, the metal matrix composites are reinforced with carbon nanotubes (CNTs) due to their strengths in excess of 100GPa and stiffness of 1000 GPa which makes them superior to carbon fibers. These composites are called Hybrid composites which have wide range of applications in various fields (Laha *et al.*, 2007). Due to very high experimental cost such work are to be numerically simulated and optimum conditions are to be found out, to improve the composites properties. The available package ANSYS FLUENT has a limitation in three fluid systems modeling. Therefore, codes are to be developed to model three fluid systems which will pave the way to model hybrid composites. Recent experimental research work are concentrated on increasing solidification rate by providing external cooling methods; this type of work involves very high cost so that CFD analysis should be extended to these fields which will provide reliable information. The two dimensional simulation study executed can be extended to all multiphase fluid flow problems where one or two fluids are solidifying. Moreover, two dimensional work carried can be extended to three dimensional work. A sound three dimensional work demands higher computational facilities. And also it is time consuming. Finally, a comparison is to be made between two dimensional work and three dimensional work.

#### 5. Conclusions

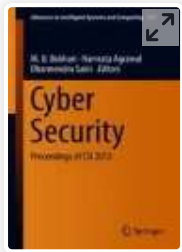
From the numerical simulation carried out it is clear that the process parameters such as stirrer speed, volume fraction of reinforcement, number blades and diameter ratio are significant factors affecting solidification pattern. Contour plots of

mushy state solidification pattern obtained for different simulation cases clearly show the influence of process parameters on solidification time and distribution of reinforcement particles. Moreover, simulation of cooling curves clearly shows the dependence of process parameters on solidification rate. Increase in stirrer speed from 50rad/sec to 150rad/sec promotes faster solidification rate. But beyond 100rad/sec stirrer speed limit there is a chance for clustering of reinforcement particles. Clustering of reinforcement particles is seen when volume fraction of reinforcement is increased beyond 10%. For 20% and 30% addition of reinforcement produce tree like structure of particles which in turn reduce solidification rate. When number of blades is increased from 3 blade geometry to 5 blade geometry an increase in solidification rate is observed at the same time uneven distribution of reinforcement particles are observed for 5 blade geometry. It is also seen from the simulation study that four blade stirrer gives a better distribution of reinforcement compared with other types of blade geometry. Increase in diameter ratio from 1.5 to 2.5 decreases the solidification rate. On the whole the present study establishes the capability of CFD to predict solidification patterns in stir casting process.

## References

- Almadhoni, K. and Khan, S. (2015), "Review of Effective Parameters of Stir Casting Process on Metallurgical Properties of Ceramics Particulate Al Composites", *IOSR Journal of Mechanical and Civil Engineering*, Vol. 12, No. 6, pp. 22-40.
- Andras, H., Christian, J., Michael, L., Christia, K., Aleksander, M. and Michael, H. (2009), "CFD Simulations of Bubble Columns using the VOF model: Comparison of Commercial and Open source solvers with an experiment", *Chemical engineering Transactions*, Vol. 18, pp. 605-610.
- Arulraj, M., Palani, P.K. and Venkatesh, L. (2017), "Optimization of Process Parameters in Stir Casting of Hybrid Meta Matrix (LM25/SiC/B4C) Composite Using Taguchi Method", *Journal of Advances in chemistry*, Vol. 13, No.11, pp. 6038-6042.
- Balasisvanandha, P.S., Karunamoorthy, L., Kathiresan, S. and Mohan, B. (2006), "Influence of stirring speed and stirring time on distribution of particles in cast metal matrix composite", *Journal of Materials Processing Technology*, Vol. 171, pp 268–273.
- Behera, R., Kayal, S., Chatterjee D. and Sutradhar, G. (2011), "Solidification Behavior and Forgeability of Stir-Cast Aluminum Alloy Metal Matrix Composites", *Canadian journal of pure and applied sciences*, Vol 5, No. 2, pp. 1541-1546.
- Bhushan, R. K. and Kumar, S. (2011), "Influence of SiC Particles Distribution and Their Weight Percentage on 7075 Al Alloy", *Journal of Materials Engineering and Performance*, Vol. 20, pp. 317-323.
- Dehnavi, M., Kuhestani, F. and Haddad S. M. (2015), "Cooling curve analysis in binary al-cu alloys: part 1- effect of cooling rate and copper content on the eutectic formation", *Metall. Mater. Eng.*, Vol. 21, No. 3, pp. 195-205.
- Devi, C.N., Selvaraj, N. and Mahesh V. (2012), "Micro structural aspects of Aluminium Silicon Carbide Metal Matrix Composite", *Int. Journal of Applied Sciences and Engineering Research*, Vol. 1, No. 2, pp. 250-254.
- Dhanalakshmi, S., Sivakumar, P. and Balasubramanian M. (2005), "Influence of Processing Parameters in SiC Aluminium Alloy Composite Produced by Stir Casting Method", *Proceedings of International Conference on Emerging Trends in Mineral Processing and Extractive Metallurgy*, pp. 490-495.
- Feller, R. J. and Beckermann, C. (1997), "Modeling of Solidification of Metal-Matrix Particulate Composites with Convection", *metallurgical and materials transactions B*, Vol. 28B, pp. 1165-1183.
- George, J., Janardhanan, S. and Sijo, M.T. (2015), "A Numerical Study on Stir Casting Process in a Metal Matrix Composite Using CFD Approach", *Advanced Materials Research*, Vol. 1119, pp. 533-541.
- Gore, R.A. and Crowe, C.T. (1989), "The effect of particle size on modulating turbulent intensity", *Int. J. Multiphase Flow*, Vol. 15, pp. 279-285.
- Hashim, J. (1999), "The Production of Metal Matrix Composites Using the Stir Casting Technique", Thesis, Dublin City University, Ireland.
- Hashim, J., Looney, L. and Hashmi, M. S. J. (1999), "Metal Matrix Composites: Production by the Stir Casting Method", *Journal of Material Processing and Technology*, Vol. 92, pp. 1-7.
- Hirt, C.W. and Nichols, B. D. (1981), "Volume of fluid VOF for the dynamics of free boundaries", *Journal of Computing Physics*, Vol. 39, pp. 201-225.
- Hong, S.J., Kim, H. M., Huh, D., Suryanarayana, C. and Chun, B. S. (2003), "Effect of clustering on the mechanical properties of SiC particulate reinforced aluminum alloy 2024 metal matrix composites", *Materials Science and Engineering*, Vol. A347, pp. 198-204.
- Johansson, K. (2011), "Numerical Simulation of Fuel Filling with Volume of Fluid." Master's Thesis, Chalmers University of Technology Gothenburg Sweden.
- Laha, T., Liu, Y. and Agarwal, A. (2007), "Carbon Nanotube Reinforced Aluminum Nanocomposite via Plasma and High

- Velocity Oxy -Fuel Spray Forming”, *Journal of Nanoscience and Nanotechnology*, Vol. 7, pp. 1-10.
- Lei, Z.G., Jun, X., Feng, Z. Z., Jun, L. G. and Fan, Z. (2010), “Effect of high shear rate on solidification microstructure of semisolid AZ91D alloy”, *Transactions Nonferrous Metals Society of China*, Vol. 20, pp. 868-872.
- Marshall, E. M. and Bakker, A. (2003), “Computational Fluid Mixing, in Handbook of Industrial Mixing: Science and Practice” *John Wiley & Sons, Inc, Hoboken, NJ, USA*.
- Naher, S., Brabazon, D. and Looney, L. (2003), “Simulation of the stir casting process”, *J Mater Process Technology*, Vol. 143-144, pp. 567-571.
- Naher, S., Brabazon, D. and Looney, L. (2005), “Development and assessment of a new quick quench stir caster design for the production of metal matrix composites”, *Journal of Material Processing Technology*, Vol. 166(3), pp. 430-439.
- Naher, S., Brabazon, D. and Looney, L. (2007), “Computational and Experimental Analysis of Particulate Distribution during Al-SiC MMC Fabrication, Composites”, Vol. 38A, pp. 719-729.
- Nguyen, D. K. and Huang, S. C. (2012), “Analysis the Effects of Turbulence Flow, the Heat, and Phases Transfer on Thermal Arrest Time in Casting Process by Computational Fluid Dynamic Method”, *Journal of Engineering Technology and Education*, Vol. 9, No.4, pp. 436-450.
- Reddy, A. C. and Zitoun, E. (2010), “Matrix Al-alloys for silicon carbide particle reinforced metal matrix composites”, *Indian Journal of Science and Technology*, Vol. 3, No. 12, pp. 1184-1187.
- Saravanakumar, P., Soundararajan, R., Deepavasanth, P. S. and Parthasarathi, N. (2016), “A Review on Effect of Reinforcement and Squeeze Casting Process Parameters on Mechanical Properties of Aluminium Matrix Composites”, *International Journal of Innovative Research in Science, Engineering and Technology*, Vol. 5, Special Issue 7, pp. 58-68.
- Singla, D.M., Dwivedi, D., Singh, L. and Chawla, V. (2009) Development of Aluminium Based Silicon Carbide Particulate Metal Matrix Composite. *Journal of Minerals & Materials Characterization & Engineering*, 8, No.6:455-467.
- Su, H., Lu, J., Lu., Z, Gao, W., Zhang, H. and Liu, H. (2010), “Optimization of Stirring Parameters Through Numerical Simulation for the Preparation of Aluminum Matrix Composite by Stir Casting Process”, *Journal of Manufacturing Science and Engineering*, Vol. 132(6), pp. 1-7.
- Surappa, M. K. (2003). “Aluminium matrix composites: Challenges and Opportunities”, *Sadhana*, Vol. 28, pp. 319-334.
- Tang, H., Wrobel, L. C. and Fan. Z. (2004), “Tracking of immiscible interfaces in multiple-material mixing processes”, *Computational Materials Science*, Vol 29, pp. 103-118.
- Wu, S., You, Y., An, P., Kanno, T. and Nakae, H. (2002), “Effect of modification and ceramic particles on solidification behavior of aluminum-matrix composites”, *Journal of Materials Science*, Vol. 37, Issue 9, pp. 1855-1860.
- Zagorski, R. and Golak, S. (2013), “Modeling of Solidification of MMC Composites during Gravity Casting Process”, *Metallurgia*, Vol. 52, No. 2, pp. 165-168.
- Zhang, D., Sugio, K., Sakai, K., Fukushima, H. and Yanagisawa, O. (2008), “Effect of Volume Fraction on the Flow Behavior of Al-SiC Composites Considering the Spatial Distribution of Delaminated Particles”, *Materials Transactions*, Vol. 49, No.3, pp. 661-670.



**Cyber Security** pp 281–289

[Home](#) > [Cyber Security](#) > Conference paper

## Composite Email Features for Spam Identification

[Princy George](#)  & [P. Vinod](#)

Conference paper | [First Online: 28 April 2018](#)

**1480** Accesses | **1** Citations

Part of the [Advances in Intelligent Systems and Computing](#) book series (AISC, volume 729)

### Abstract

An approach is proposed in this work to search for composite email features by applying a language-specific technique known as NLP (Natural Language Processing) in email spam domain. Different style markers are employed on Enron-spam dataset to capture the nature of emails written by spam and ham email authors. Mainly, features from five categories, consisting of character-based features, word-based features, tag-based, structural features, and Bag-of-Words, are extracted. Dimensionality



reduction is applied subsequently using TF–IDF–CF (Term Frequency–Inverse Document Frequency–Class Frequency) feature selection method in order to choose the prominent features from the huge feature space. The experiments are carried out on individual feature as well as composite feature models. A promising performance is produced by composite model with an  $F$ -measure of 0.9935 and minimum  $FPR$  of 0.0004.

## Keywords

**Email**   **Ham**   **Spam**   **Style markers**

**Dimensionality reduction**   **Composite model**

---

This is a preview of subscription content, [log in via an institution](#).

---

▼ Chapter	EUR 29.95
	Price includes VAT (India)
<ul style="list-style-type: none"><li>• Available as PDF</li><li>• Read on any device</li><li>• Instant download</li><li>• Own it forever</li></ul>	
<div style="border: 1px solid #ccc; padding: 10px; text-align: center;">Buy Chapter</div>	
> eBook	EUR 85.59
> Softcover Book	EUR 99.99

Tax calculation will be finalised at checkout

**Purchases are for personal use only**

[Learn about institutional subscriptions](#)

## References

---

1. Zhu Y, Tan Y (2011) A local-concentration-based feature extraction approach for spam filtering. *IEEE Trans Inf Forensics Secur* 6(2):486–497

---

2. Wang D, Irani D, Pu C (2013) A study on evolution of email spam over fifteen years. In: Bertino E, Georgakopoulos D, Srivatsa M, Nepal S, Vinciarelli A (eds) *CollaborateCom*, pp 1–10. ICST/IEEE

---

3. Cheng N, Chandramouli R, Subbalakshmi KP (2011) Author gender identification from text. *Digital Invest* 8.1:78–88

---

4. Manning CD (1999) *Foundations of statistical natural language processing*. In: Schutze H (ed). MIT Press, Cambridge

---

5. Bird S, Klein E, Loper E (2009) *Natural language processing with Python*. O'Reilly Media, Inc.

---

6. Menahem E, Rokach L, Elovici Y (2013) Combining one-class classifiers via meta learning. In: Proceedings of the 22nd ACM international conference on information and knowledge management, ACM

---

7. Blanzieri E, Bryl A (2008) A survey of learning-based techniques of email spam filtering. *Artif Intell Rev* 29.1:63–92

---

8. Menahem E, Pusiz R, Elovici Y (2012) Detecting spammers via aggregated historical data set. *Network and system security*. Springer, Berlin, pp 248–262

---

9. Xu C, Su B, Cheng Y, Pan W, Chen L (2014) An adaptive fusion algorithm for spam detection. *IEEE Intell Syst* 29(4):2–8

---

10. Guzella TS, Caminhas WM (2009) A review of machine learning approaches to spam filtering. *Expert Syst Appl* 36(7):10206–10222

---

11. Drucker H, Wu S, Vapnik VN (1999) Support vector machines for spam categorization. *IEEE Trans Neural Netw* 10.5:1048–1054

---

12. Ruan G, Tan Y (2010) A three-layer back-propagation neural network for spam

detection using artificial immune concentration. *Soft Comput* 14(2):139–150

---

13. Zhou B, Yao Y, Luo J (2010) A three-way decision approach to email spam filtering. In: Farzindar A, Keselj V (eds) *Canadian conference on AI. LNCS*, vol 6085. Springer, pp 28–39

---

14. Wu C-H (2009) Behavior-based spam detection using a hybrid method of rule-based techniques and neural networks. *Expert Syst Appl* 36(3):4321–4330

---

15. Bekkerman R (2004) Automatic categorization of email into folders: benchmark experiments on Enron and SRI corpora

---

16. The Enron-Spam Datasets.  
<http://www.aueb.gr/users/ion/data/enron-spam/>

---

17. Natural Language Tool Kit (NLTK).  
<http://www.nltk.org/>

---

18. POS tagging.  
<http://textminingonline.com/dive-into-nltk-part-iii-part-of-speech-tagging-and-pos-tagger>

---

19. Liu M, Yang J (2012) An improvement of TFIDF weighting in text categorization. In: International proceedings of computer science and information technology, pp 44–47 (2012)

---

20. WEKA-Data Mining Software in Java.  
<http://www.cs.waikato.ac.nz/ml/weka>

---

21. Han J, Kamber M (2005) Data mining: concepts and techniques. Kaufmann, San Francisco [u.a.]

---

22. Kibriya AM, Frank E, Pfahringer B, Holmes G (2004) Multinomial Naïve Bayes for text categorization revisited. In: Webb GI, Yu X (eds) Australian conference on artificial intelligence. LNCS, vol 3339. Springer, Berlin, pp 488–499

---

23. Metsis V, Androutsopoulos I, Paliouras G (2006) Spam filtering with Naïve Bayes-which Naïve Bayes? In: CEAS, pp 27–28

---

24. Bird S (2006) NLTK: the natural language toolkit. In: Proceedings of the COLING/ACL on interactive presentation sessions, association for computational linguistics

---

## Author information

---

### Authors and Affiliations

**Department of Computer Science &  
Engineering, SCMS School of Engineering &  
Technology, Ernakulam, Kerala, India**

Princy George & P. Vinod

Corresponding author

Correspondence to [Princy George](#).

Editor information

---

Editors and Affiliations

**Department of Computer Science, Aligarh  
Muslim University, Aligarh, Uttar Pradesh, India**

M. U. Bokhari

**National Institute of Financial Management,  
Faridabad, Haryana, India**

Namrata Agrawal

**Bharati Vidyapeeth's College of Engineering  
(BVCOE), New Delhi, India**

Dharmendra Saini

Rights and permissions

---

[Reprints and permissions](#)

Copyright information

---

© 2018 Springer Nature Singapore Pte Ltd.

About this paper

---

Cite this paper

George, P., Vinod, P. (2018). Composite Email Features for Spam Identification. In: Bokhari, M., Agrawal, N., Saini, D.

(eds) Cyber Security. Advances in Intelligent Systems and Computing, vol 729. Springer, Singapore.

[https://doi.org/10.1007/978-981-10-8536-9\\_28](https://doi.org/10.1007/978-981-10-8536-9_28)

[.RIS](#)  [.ENW](#)  [.BIB](#) 

DOI	Published	Publisher Name
<a href="https://doi.org/10.1007/978-981-10-8536-9_28">https://doi.org/10.1007/978-981-10-8536-9_28</a>	28 April 2018	Springer, Singapore

Print ISBN	Online ISBN	eBook Packages
978-981-10-8535-2	978-981-10-8536-9	<a href="#">Engineering</a> <a href="#">Engineering (R0)</a>

## Publish with us

---

[Policies and ethics](#)

# Comparison of Classifier Strength for Detection of Retinal Hemorrhages

Sreeja K.A., S.S. Kumar

*Abstract: Diabetes Mellitus(DM) which is the root cause of diabetic retinopathy(DR) diseases such as occlusion, microaneurysms, retinal hemorrhage, etc. Hemorrhage is considered the most dangerous among these, as it can accelerate the occurrence of vision loss. Hence, the severity of hemorrhages is analyzed in most of the recent studies of diabetic retinopathy detection. This paper focusses on the best classification approach by comparing different machine learning approach using supervised classifiers. Fundus image collected from publically available database are preprocessed and enhanced. Using splat based method, ground truth is established with the help of a retinal expert. Supervised classifiers are trained from the GLCM features extracted from the segmented images and validated on clinical images. The experimental results were verified by the Area Under Curve(AUC) for the three classifiers that were trained and results are verified and tabulated.*

## I. INTRODUCTION

DR detection is usually done from the analysis of fundus images. The fundus image of a person with the retinal hemorrhage compared with a normal retina is shown in Fig. 1. Image segmentation is the technique used to extract the features and analyze retinal images. This method is non-invasive and cost effective and that is the reason we chose Image based method for our analysis.

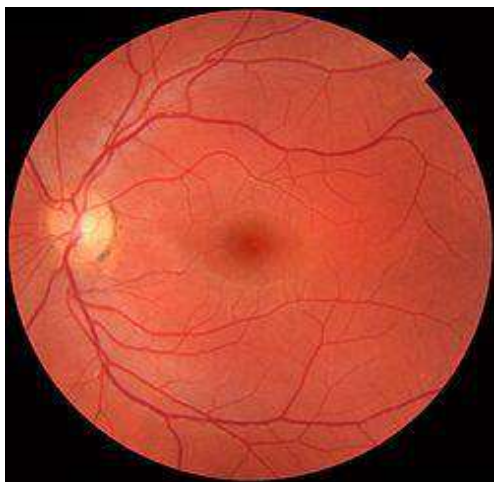


Figure 1 a

Figure 1 a. Fundus Image of a Normal Retina.



Figure 1 b

Figure 1 b. DR Fundus image with Hemorrhages.

## II. LITERATURE REVIEW

Recent developments in DR studies suggest an increase in the number of diabetic patients as well as new methods to detect the retinopathy symptoms like retinal hemorrhage. A systematic review has been described using PRISMA guidelines in [1] based on meta-analysis. IN order to discern between DR and glaucoma Rommel et. al [2] proposed a work using statistical texture analysis for retinal disease screening. The implementation of a digital tool that facilitates ophthalmologist to what extent the DR has affected is proposed in [3]. The implementation is based on Gabor transform and uses digital filters for a quality retinography tool. Detection of all the DR symptoms such as Microaneurysms, exudates, hemorrhages, etc. has been reviewed in [4]. Alongside several blood vessel detection technique for retinal fundus images have been described in [4].Recent studies on Diabetic Neuropathy is presented by R. B. Kakkeri. et. al. [5] where the phenomenon called neovascularization is explained. Machine learning algorithm based retinopathy diagnosis in [6] predicts the presence of diabetic retinopathy using alternating decision tree, adaBoost, Naive Bayes, Random Forest and SVM classifiers. Exudate detection using artificial neural network algorithm was presented in [7].

## III. FUNDUS IMAGE SEGMENTATION

Image segmentation techniques, as already said is the effective method to extract features from a retinal fundus image. There are several image segmentation techniques

Revised Manuscript Received on April 12, 2019.

Sreeja K.A., Asst. Professor, Dept. Of Electronics and Communication Engg., SCMS School of Engineering & Technology, Karukutty, Ernakulam, Kerala, India. (ka.sreeja@gmail.com)

S.S. Kumar, Associate Professor, Dept. of Electronics and Instrumentation Engg., Noorul Islam University, Kanyakumari, Tamil Nadu, India.

available over literature which

Published By:  
Blue Eyes Intelligence Engineering  
& Sciences Publication





can be utilized to segment the required region in an image. All segmentation methods share some of the common stages, such as pre-processing, processing and post-processing stages. Retinal segmentation techniques are broadly classified into two [8] as rule based methods and machine based methods. In this paper, machine based methods are preferred that utilizes ground truth and has a labelled dataset to train the classifiers. An irregular segmentation technique employing a high level entity called splat is the method[9] utilized here. Pixels that share the same structural and spatial properties are partitioned into a non-overlapping entity known as splat. Since, Hemorrhages contain blood, those hemorrhage pixels have similar properties such as color, intensity, spatial locations etc. These pixels are delineated from the whole image to form hemorrhage splats. Before segmentation of the fundus image to generate splats, the blood vessels are to be removed so that the they should not be misinterpreted as hemorrhages since both have similar structural properties.

III a. Blood vessels removal

Inorder to make the splat based method more effective, the blood vessels are removed using a **Kirsch compass kernel**. [10]The Kirsch’s operator takes a single kernel mask and turns it in 45° increments over all 8 compass courses such as: N, NW, W, SW, S, SE, E, and NE. The maximum magnitude across all directions is the value of edge magnitude of the Kirsch operator. It is calculated as

$$h_{n,m} = \max_{z=1,\dots,8} \sum_{i=-1}^1 \sum_{j=-1}^1 g_{i,j}^{(z)} \cdot f_{n+i,m+j} \quad (1)$$

Where  $g^z$  is the 8 different compass direction kernels.

III b. Splat Generation

Using edge detection, the vessels are delineated and the image is segmented to generate splats. Meaningful splats, are created by a scale specific over segmentation which is done in two steps. Initially, gradient scale of contrast enhanced bright-dark opponent image is taken using diverse gradations(scales), as the appearance of hemorrhages varies in different locations. The values of the scales are grouped and the highest of the gradient value with its scale of interest(SOI) is taken to accomplish watershed segmentation. [11]

The gradient magnitude is computed using the equation

$$|\nabla I(x, y; s)| = \sqrt{I_x(x, y; s)^2 + I_y(x, y; s)^2} \quad (2)$$

where  $I(x, y; s)$  is the image. Now creating a scale-space depiction of the image using Gaussian kernels  $G_s$ , the gradient magnitude is computed from its derivatives –the horizontal and vertical ones as:

$$|\nabla I(x, y; s)| = \sqrt{\left[ \frac{\partial}{\partial x} (G_s * I(x, y)) \right]^2 + \left[ \frac{\partial}{\partial y} (G_s * I(x, y)) \right]^2} \quad (3)$$

$$|\nabla I(x, y; s)| = \sqrt{\left[ \frac{\partial G_s}{\partial x} * I(x, y) \right]^2 + \left[ \frac{\partial G_s}{\partial y} * I(x, y) \right]^2} \quad (4)$$

where the symbol \* signify convolution and  $\frac{\partial G_s}{\partial x}$  and  $\frac{\partial G_s}{\partial y}$  are the 1° derivatives of Gaussian in the x axis and y axis direction using the scale s

The highest of the gradient magnitude is

$$|\nabla I(x, y)| = \max_i |\nabla I(x, y; s_i)| \quad (5)$$

While the field surface in watershed algorithm is essential [11] to attain meaningful splats, the greatest of the gradient magnitude is taken for a definite scale of Interest (SOI). The splats are generated based on Algorithm 1.

Algorithm 1. Splat Generation

```

1: function SPLAT_GEN(gradientoutputimage)
2:   nSeg ← Number of segments required
3:   thresGrad ← Gradient threshold
4:   top:
5:   finSeg ← Number of segments generated after
6:   watershed segmentation
7:   if nSeg > finSeg then
8:     thresGrad ← thresGrad+1
9:     loop:
10:    if imageGrad(a)(b) > thresGrad then
11:      newimageGrad(a)(b) ← imageGrad(a)(b)
12:      p=a+1
13:      q=b+1
14:      goto loop.
15:    imageGrad = newimageGrad
16:    goto top.
return finalimage ← watershed(imageGrad)

```

Thus the image can be portioned as non-overlapping splats having similar intensity over the entire image[9]. Some of the Splats formed by means of diverse scales exploiting the same watershed algorithm is shown in the figure 2.

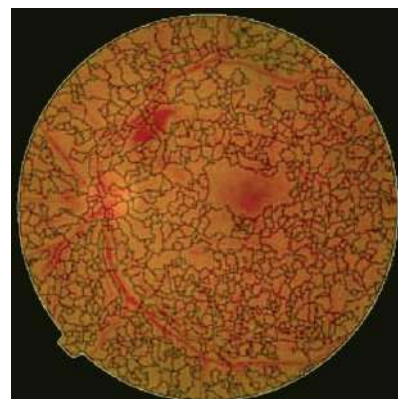


Figure 2a



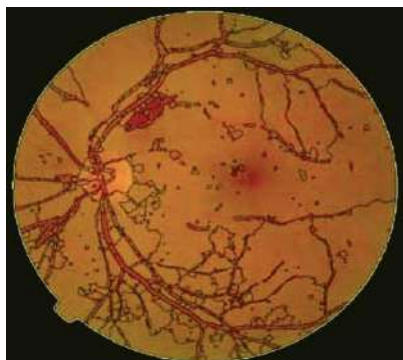


Figure 2b

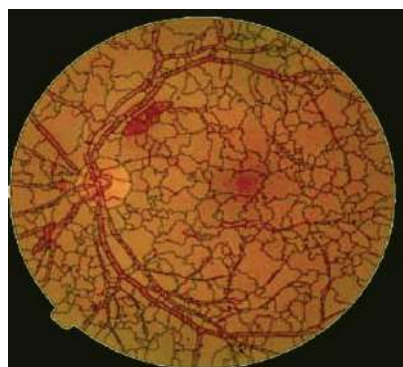


Figure 2c

Fig. 2a has smaller splats which are generated with scales outside the desired SOI for hemorrhage splats. The range of scales used in Fig. 2a can be used for optic disc removal and blood vessel detection. Fig. 2b uses a fine scale and also less than the desired SOI. These range of scales can be used in the detection of Microaneurysms and exudates. Figure 2c is the required scale for hemorrhages detection as the retinal background is represented by larger splats and blood regions are represented as smaller splats.

The total number of splats generated is kept under a threshold without compromising the accuracy and speed of computation.

#### IV. GOLD STANDARD LABELLING BY OPHTHALMOLOGIST

The splats obtained by segmentation are labelled with the help of an ophthalmologist in order to train the supervised classifiers for the clinical images. For the DIARETDB1 database, ground truth's confidence level is kept as 0.75 based on the evaluation done in [12]. This level is the certainty of the decision that a splat is accurate.

Feature Extraction and Feature Subset Selection:

The classifiers can be trained to detect the target objects after assigning reference labels for splats. An overall 352 possibly relevant features are taken from each splats to train the classifiers.

They are:

1) Color: Colors of each splat is obtained in RGB color space and dark-bright (db), red-green (rg), and blue-yellow (by) opponency images [13], which derives to six colour components.

2) Difference Of Gaussian (DoG Filter ): Difference of Gaussian (DoG) kernels are employed at five distinct

smoothing scales with one baseline scale to take advantage of Gaussian scale space. [14][15]

3) Responses from Gaussian Filter Bank[13]: A Gaussian filter bank which include a first order derivative and a second order derivative with at two orientations and three orientations respectively are applied to the green channel.

4) Responses from Schmid Filter Bank: 13 kernels of Schmid filter banks which are rotationally invariant is applied to the dark bright opponency image.

5) Responses from Local Texture Filter Banks: Local texture filter bank contains local entropy filter, local range filter and local standard deviation filter which calculate the entropy, standard deviation and intensity range of a single pixel in a given region [16].

The above features are combined to obtain a meaningful response image that has small inter splat similarity and large intra splat similarity[13] [15] [16] [17]. These features mentioned above are called pixel- based responses. Alongside these features, we take splat wise features according to Gray-Level Co-occurrence Matrix (GLCM)[16] [18] [19] [20] statistics. These are splat area, extent, texture, solidity and orientations. After sequential forward feature selection subset(SFS) insignificant and redundant ones were removed from the feature set and only the relevant features were considered. The 19 features considered for training the classifiers are shown in Table I

TABLE I

Features	Number	Description
DoG filter bank	s2 - s0.5	from Green channel
DoG filter bank	s4 - s0.5	from db and rg
DoG filter bank	s8 - s 0.5	opponency from db opponency
Gaussian Filter Bank	s=8 orientation:2,3	Mean of second order Gaussian derivative from green channel
Gaussian Filter Bank	s=1,2,4 orientation:1,2,3	Mean of second order Gaussian derivative from green channel
Schmid filter bank	response=11 s=8,16	Mean of second order Gaussian derivative from green channel
Mean of Gaussian		from db opponency from Green channel

#### V. CLASSIFICATION USING DIFFERENT CLASSIFIERS

In order to do the classification, several machine learning algorithms are available over literature. Among them, three classifiers are used to train our experiment and evaluate the result. They are: Neural Network Classifier, Naïve Bayes Classifier and kNN Classifier.

A. Neural Network classifier:

Artificial neurons or nodes which are biliogically inspired from the functionality of



human brain forms the key part of a neural network. Individually nodes have their own scope of intelligence concerning rules and functionalities to improve it-self through knowledges learned from previous methods which is called backpropagation. Neural networks are suitable to identify non-linear patterns, where there isn't a one-to-one relationship between the input and output[21]. The neural network consists of input layers, hidden layers and a threshold function. All the nodes are interconnected to form a network.

Neural networks are characterized by holding adaptive weights along paths between neurons that can be adjusted by a backpropagation algorithm that learns from perceived data in order to improve the learning model. The inputs to the neural network classifier are the relevant feature set and they are transformed using the desired weights from the hidden layer. Finally, using a sigmoid transfer function the output class is determined.

**B. Naïve Bayes Classifier:**

The naive Bayes classifier [22] uses the principle of Bayesian maximum a posteriori (MAP) classification: measure a finite set of features  $x = (x_1, \dots, x_n)$  then select the class

$$\hat{y} = \underset{y}{\operatorname{arg\,max}} P(y|x) \tag{6}$$

where

$$P(y|x) \propto P(x|y)P(y)$$

$P(y|x)$  is the likelihood of feature vector  $x$  given class  $y$ , and  $P(y)$  is the priori probability of class  $y$ . Naive Bayes classifier assumes that the features are independent of the condition. For the class:

$$P(y|x) = \prod_i P(x_i|y) \tag{7}$$

The parameters  $P(x_i|y)$  and  $P(y)$  are obtained from the training data.

**C. kNN Classification**

The kNN algorithm allocates soft class labels. The two output classes defined are hemorrhage splat or non-hemorrhage splat. Euclidean distance is the measure by which the classifier decides whether a particular splat belongs to hemorrhage or normal class in an optimized feature space. As the value of  $k$  is increased the computation time increases and the splats are more accurately identified. But since all the  $k$  nearest neighbors are not near, an optimum value of  $k$  is chosen instead of an arbitrary value.

**VI. EXPERIMENT AND RESULTS**

**A. Data acquisition and Pre-processing**

The fundus images were acquired from two sources. Clinical images were obtained from Dr. Bhejan Singh's eye hospital. The clinical image was captured using a "Remidio Non-Mydriatic Fundus On Phone (FOP-NM10)"

[23] Camera with FOV 40°, working distance of 33mm and an ISO range from ISO 100 to 400. The images used for training was acquired from the publically available database DIARETDB1

(<http://www.it.lut.fi/project/imageret/diaretdb1/index.html>).

An overall 1500 images were taken among which 1050 images were taken for training, 225 images for testing and 225 for validation. The gold standard reference observations were accomplished by an ophthalmologist expert using the splat-based interpretation. Overall 1200 (950 from training set 150 from testing) images were marked by the expert from a total of 1500. Preprocessing is done in order to adapt the color variation throughout the dataset and also to equalize the intensity of the image. Histogram equalization is done using Contrast limited Adaptive Histogram Equalization(CLAHE)[24]. Also Each image is normalized according to its prevailing pixel value at the three colour channels. The pixel values that occur frequently are shifted to the beginning of RGB colour space.

**B. Classification and result**

From the 1050 training images. 10100 splats were formed. In this there were approximately 300 hemorrhage splats. This amounts to a very low hemorrhage splat density. So images having at least 6 splats are taken for training, where the value 6 is arbitrarily chosen. After sequential forward feature selection subset(SFS) 19 unique features were considered and the insignificant and redundant features were omitted from the feature set. The set of features are already shown in Table I.

For the neural network classifier, the network protocols used for detection are as shown in table II.

**TABLE II**

Features	Hemorrhage splats
Learning rule base	Delta rule
Transfer function	Sigmoid
Hidden Layer Elements	30
Preprocessing filter	Feature set
Number of training iterations	1000
Training algorithm	Bayesian
Neural network	Fitting network
Training time- Core i5, 4.10 GHz	10 min
Number of training splats	7350
Number of testing splats	3150

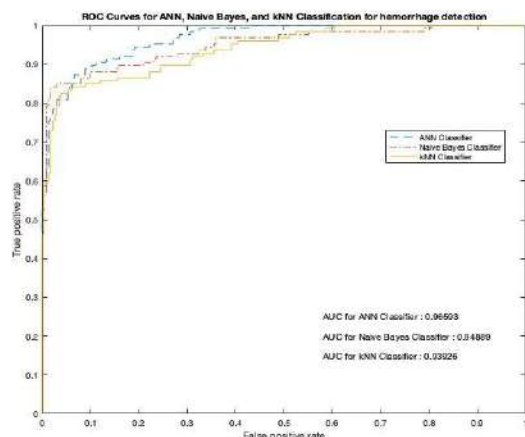
For the kNN Classifier, the value of  $k$  was chosen between 15 to 160 that involves both feature selection as well classification. After repeated calculations, the value of  $k$  was fixed at 105 without compromising and prediction accuracy and computation period. For the Naïve Bayes classification in addition to the above features, six Difference of Gaussian (DoG) filter responses were taken. The DoG filter deducts one distorted version of an original image from another distorted version of the image [25]. The convolution was done with seven different Gaussian kernels with SD of 0.75, 1.5, 3, 6, 12, 24, and 48. We used DoG1,



DoG2, DoG3, DoG4, DoG5 and DoG6 to state the features attained by subtracting the image at scale  $\sigma = 0.75$  from  $\sigma = 1.5$ , scale  $\sigma = 1.5$  from  $\sigma = 3$ , scale  $\sigma = 3$  from  $\sigma = 6$ , scale  $\sigma = 6$  from  $\sigma = 12$ , scale  $\sigma = 12$  from  $\sigma = 24$ , and scale  $\sigma = 24$  from  $\sigma = 48$ , respectively.

The results were obtained for the fundus image shown in Fig 2. The Area Under Curve(AUC) for the Receiver Operator Characteristics (ROC) curve is shown in Fig. III

Figure III



The Obtained accuracy, sensitivity and specificity for the three different classifiers are tabulated in Table III. From this the maximum AUC is attained for the Neural Network Classifier of AUC= 0.96 followed by the Naïve Bayes classifier of AUC = 0.94 and finally the kNN Classifier with AUC= 0.93.

TABLE III

Classifier	Sensitivity	Specificity	AUC for test data
ANN	87.651	87.145	0.96
Naïve Bayes	84.476	83.791	0.94
kNN	80.872	82.137	0.93

## VII. CONCLUSION

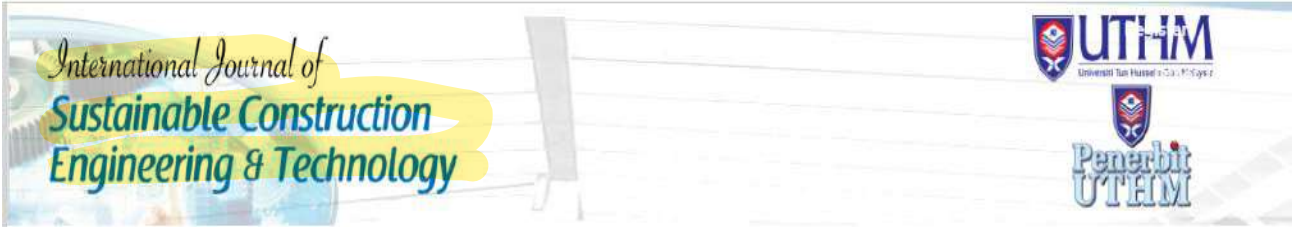
From the above test results, it is clear that a promising sensitivity and specificity is provided by the neural network classifier. From literature it is understood that, a more sensitive result can be acquired using an advanced Convolutional neural network classifier(CNN). A new algorithm using CNN network is the future scope of this work.

## REFERENCES

1. R. Cheloni, S. A. Gandolfi, C. Signorelli, and A. Odone, "Global prevalence of diabetic retinopathy: protocol for a systematic review and meta-analysis.," *BMJ Open*, vol. 9, no. 3, p. e022188, Mar. 2019.
2. R. M. Anacan *et al.*, "Retinal Disease Screening through Statistical Texture Analysis and Local Binary Patterns using Machine Vision," in *2018 IEEE 10th International Conference on Humanoid, Nanotechnology, Information*

3. Y. Morales, R. Nuñez, J. Suarez, and C. Torres, "Digital tool for detecting diabetic retinopathy in retinography image using gabor transform," in *Journal of Physics: Conference Series*, 2017.
4. J. Amin, M. Sharif, and M. Yasmin, "A Review on Recent Developments for Detection of Diabetic Retinopathy," *Scientifica (Cairo)*, vol. 2016, pp. 1–20, Sep. 2016.
5. V. D. R. B. Kakkeri, Sayali Surve, Shahrulkh Shaikh, "Detection of Diabetic Retinopathy," *Int. J. Innov. Technol. Explor. Eng(IJITEE)*, vol. 5, no. 12, 2016.
6. K. Bhatia, S. Arora, and R. Tomar, "Diagnosis of diabetic retinopathy using machine learning classification algorithm," in *2016 2nd International Conference on Next Generation Computing Technologies (NGCT)*, 2016, pp. 347–351.
7. S. W. Franklin and S. E. Rajan, "Diagnosis of diabetic retinopathy by employing image processing technique to detect exudates in retinal images," *IET Image Process.*, vol. 8, no. 10, pp. 601–609, Oct. 2014.
8. J. Almotiri, K. Elleithy, and A. Elleithy, "Retinal Vessels Segmentation Techniques and Algorithms: A Survey," *Appl. Sci.*, 2018.
9. L. Tang, M. Niemeijer, J. M. Reinhardt, S. Member, M. K. Garvin, and M. D. Abramoff, "Splat Feature Classification With Application to Retinal Hemorrhage Detection in Fundus Images," vol. 32, no. 2, pp. 364–375, 2013.
10. R. A. Kirsch, "Computer determination of the constituent structure of biological images," *Comput. Biomed. Res.*, 1971.
11. Yung-Chieh Lin, Yu-Pao Tsai, Yi-Ping Hung, and Zen-Chung Shih, "Comparison between immersion-based and toboggan-based watershed image segmentation," *IEEE Trans. Image Process.*, vol. 15, no. 3, pp. 632–640, Mar. 2006.
12. T. Kauppi *et al.*, "the DIARETDB1 diabetic retinopathy database and evaluation protocol," in *Proceedings of the British Machine Vision Conference 2007*, 2007.
13. M. D. Abramoff *et al.*, "Automated Segmentation of the Optic Disc from Stereo Color Photographs Using Physiologically Plausible Features," *Investig. Ophthalmology Vis. Sci.*, vol. 48, no. 4, p. 1665, Apr. 2007.
14. B. M. ter Haar Romeny, *Front-end vision and multi-scale image analysis: multi-scale computer vision theory and applications*, written in Mathematica. Kluwer Academic, 2003.
15. L. Tang, M. Niemeijer, and M. D. Abramoff, "Splat feature classification: Detection of the presence of large retinal hemorrhages," in *2011 IEEE International Symposium on Biomedical Imaging: From Nano to Macro*, 2011, pp. 681–684.
16. O. Engler, *Introduction to Texture Analysis: Macrotecture, Microtexture, and Orientation Mapping*, Second Edition. CRC Press LLC, 2017.
17. M. Varma and A. Zisserman, "A Statistical Approach to Texture Classification from Single Images," *Int. J. Comput. Vis.*, vol. 62, no. 1/2, pp. 61–81, Apr. 2005.
18. H. Tamura, S. Mori, and T. Yamawaki, "Textural Features Corresponding to Visual Perception," *IEEE Trans. Syst. Man. Cybern.*, vol. 8, no. 6, pp. 460–473, 1978.
19. M. Niemeijer, J. Staal, B. van Ginneken, M. Loog, and M. D. Abramoff, "Comparative study of retinal vessel segmentation methods on a new publicly available database," 2004, vol. 5370, p. 648.
20. M. Niemeijer, M. D. Abramoff, and B. van Ginneken, "Segmentation of the Optic Disc, Macula and Vascular Arch in Fundus Photographs," *IEEE Trans. Med. Imaging*, vol. 26, no. 1, pp. 116–127, Jan. 2007.
21. G. G. Gardner, D. Keating, T. H. Williamson, and A. T.

- Elliott, "Automatic detection of diabetic retinopathy using an artificial neural network: A screening tool," *Br. J. Ophthalmol.*, 1996.
22. J. J. Cochran, L. A. Cox, P. Keskinocak, J. P. Kharoufeh, J. C. Smith, and M. Goldszmidt, "Bayesian Network Classifiers," in *Wiley Encyclopedia of Operations Research and Management Science*, 2011.
  23. "Remidio Non-Mydriatic Fundus On Phone (FOP-NM10)."
  24. Kee Yong Pang, I. Lila Iznita, M. H. Ahmad Fadzil, A. N. Hanung, N. Hermawan, and S. A. Vijanth, "Segmentation of retinal vasculature in colour fundus images," in *2009 Innovative Technologies in Intelligent Systems and Industrial Applications*, 2009, pp. 398–401.
  25. M. W. D. Kenneth R. Spring, John C. Russ, Matthew J. Parry-Hill, Thomas J. Fellers, "Molecular Expressions Microscopy Primer: Digital Image Processing - Difference of Gaussians Edge Enhancement Algorithm - Interactive Tutorial." [Online]. Available: <https://micro.magnet.fsu.edu/primer/java/digitalimaging/processing/diffgaussians/index.html>. [Accessed: 06-May-2019].



HOME ARCHIVES VOL. 9 NO. 2 (2018) Articles

## Effect of Copper Slag and Granite Powder on the Mechanical Properties of Reclaimed Asphalt Pavement Aggregate Concrete

**Mahitha T**

SCMS School of Engineering & Technology

**Aswini J**

SCMS School of Engineering & Technology, Kerala

PDF 759

PUBLISHED

20-12-2018

HOW TO CITE

**Keywords:** Reclaimed asphalt pavement aggregate, Abrasion, Attrition, Copper slag, Granite powder, Compressive strength, Flexural strength, Split tensile strength, Sustainability

MAKE A SUBMISSION

Focus and Scope

Editorial Board

Guideline for Authors

Indexing and Abstracting

Publishing Ethics

Copyright and License

Open Access Policy

Charge

Activate Windows  
Go to Settings to activate

Indexed by:

## **Effect of Copper Slag and Granite Powder on the Mechanical Properties of Reclaimed Asphalt Pavement Aggregate Concrete**

T.Mahitha<sup>1</sup>, J. Aswini<sup>2</sup>

<sup>1,2</sup> Department of civil engineering, APJ Abdul Kalam Technological University, Calicut, India

\*Corresponding E-mail: mahi.thodiyil@gmail.com

Received 24 May 2018; Revised 20 November 2018; Accepted 5 December 2018

DOI: <https://10.30880/ijscet.2018.09.02.001>

---

### **Abstract**

The replacement of natural gravel aggregate with reclaimed asphalt as coarse aggregate would help in reduction of environmental and ecological effects. Researches were rarely performed by replacing fine aggregate in reclaimed asphalt pavement aggregate concrete. This project aims to investigate the feasibility of improving the strength of recycled asphalt aggregate concrete in which recycled asphalt aggregate is used as a partial replacement of coarse aggregate at 30%. Abrasion and attrition technique is used to modify or roughen the surface of RAP aggregates. Granite powder and copper slag are used as a partial replacement of sand at 5, 10, 15, 20 and 25% in Abrasion and attrition Treated Reclaimed Asphalt Pavement Aggregate Concrete (ABTRAPC). Thirty cubes, twenty cylinders and twenty beams of concrete with granite powder and thirty cubes, twenty cylinders and ten beams of concrete with copper slag were made and tested. The 7<sup>th</sup> and 28<sup>th</sup> day strengths were found out at these replacements. It was observed that the compressive strength, split tensile strength and flexural strength was found to be maximum at 15% replacement of sand by copper slag. The compressive strength was increased about 29.8% compared to ABTRAPC. Flexural strength similar to normal concrete and about 12.8% greater compared to ABTRAP concrete. The compressive strength and flexural strength was also increased to a maximum at 15% replacement of sand by granite powder and split tensile strength at 20% replacement of granite powder. The results showed that the potential of reclaimed asphalt aggregates as a partial replacement of coarse aggregates in concrete could be effectively enhanced with its a combination with granite powder or copper slag. The increase in compressive strength values and the increase in flexural strength values similar to normal concrete proved that this concrete has its potential to be used in pavement applications.

**Keywords:** *Reclaimed asphalt pavement aggregate, Abrasion, and attrition, Copper slag, Granite powder, Compressive strength, Flexural strength, Split tensile strength, Sustainability*

---

### **1.0 Introduction**

The current concrete construction practice is thought unsustainable due to the consumption of enormous quantities of stone, sand, drinking water and cement. To move towards ecological sustainability, we must move on to low cost and highly durable concrete mixtures containing largest possible amounts of industrial and urban byproducts that could be suitable as a partial replacement of Portland cement, aggregate and drinking water. Natural aggregate accounts for more than 70% of the volume of concrete. The increasing demand for quality natural aggregates and the subsequent effects on the environment led to the need to consider locally and cheaply available materials in concrete.

India has the second largest road network in the world. Reclaimed Asphalt Pavement (RAP) is the removed pavement materials composed of asphalt and aggregates. These materials are produced when asphalt pavements are removed during reconstruction and resurfacing. The replacement of gravel aggregate with reclaimed asphalt would also help in reducing the quantity of reclaimed asphalt which would otherwise be disposed of in landfill sites. The applications of concrete containing recycled asphalt have been very limited due to its low strength. Thus there is a need to find methods to improve the properties of concrete containing RAP as partial replacement of coarse aggregate. Partial replacement of fine aggregate of this concrete containing RAP with a suitable cheap and recyclable material is an interesting area of study. Granite powder is obtained as

a by-product from granite cutting or polishing industries. Granite powder is also generated from recycling marble tops, granite pavers and stone scraps. This powder is deposited in large amounts causing a threat to the environment. Inhalation of fine dust of granite powder causes lung diseases. The use of granite powder in concrete would minimize its effect on the environment. Copper slag is an industrial by-product material produced from the process of manufacturing copper. Approximately 24.6 million tons of slags are estimated to be generated from the copper industries in the world. Some amount of copper slag is mainly used in the sand blasting industry and in the manufacturing of abrasive tools and the remaining is disposed of in the ecosystem without any reuse.

## **2.0 Literature Review**

Reference [1] studied on fine fraction of Reclaimed Asphalt Pavement (RAP) aggregates as an alternative to natural fine aggregates. Cement mortar samples were prepared with 25%, 50%, 75% and 100% replacement of natural aggregates. The decrease in strength of cement mortar may be due to the increase in the porosity of Interfacial Transition Zone (ITZ) and the predominance of asphalt-cohesion failure in comparison to asphalt adhesion failure. It also opens up the scope to incorporate mineral admixtures in mortar mixes to improve the strength of the same with a higher percentage of RAP content. Reference [2] investigated the effect of using copper slag replacement by preparing eight concrete mixes with different proportions of copper slag (0-100%). The compressive, tensile and flexural strength of concrete was comparable to the control mix using up to 50% copper slag. Copper slag, in the range of 40–50%, could potentially replace sand in concrete mixtures. Al-Mufti et al. [3] investigated improving the strength properties of recycled asphalt aggregate concrete. Replacement of 20 mm gravel with recycled asphalt aggregate at 25%, 50%, 75% were compared with 100% recycled asphalt aggregate concrete and control concrete. A replacement of 25% reduces 28 days strength by 27%. Further increase in replacement results in further reduction in strength but at a more reduced rate. Roughening of aggregate prior to mixing for 3 hour increases the strength reaching similar strength to normal concrete. Roughening of recycled asphalt aggregate alone for 3 hours made a limited improvement in concrete strength. The treatment of recycled asphalt aggregate with solvent turpentine has no effect on strength development of concrete.

Reference [4] studied bonding properties in cementitious materials with asphalt-coated particles. Interfacial Transition Zone (ITZ) properties and phase distribution with age of reclaimed asphalt showed high porosity, larger ITZ size, low CH and CSH contents near the interface. This caused a reduction in concrete strength and bulk modulus. Hydrophobic nature of asphalt prevented hydration products from growing around aggregate in larger and porous ITZ. Mortars with RAP showed a decreasing trend in the CH content near the aggregate interface suggesting that somehow asphalt is preventing CH growth. Even though the silica fume decreased the porosity to some extent, the CH content is found to reduce with age due to the pozzolanic reaction of silica fume. Reference [5] studied the nature of the cement-asphalt bond. The interfacial cement-asphalt bond energy was found to improve by several chemical oxidative treatments of the asphalt without affecting the porosity and size factors in the ITZ. Asphalt cohesion is found out to be as the preferential failure mode than the cement-asphalt adhesion or ITZ cohesion. A lower bulk modulus is produced due to the higher porosity in ITZ which allows for easier crack initiation, and the preferential asphalt cohesion failure. An improvement in the concrete the mechanical properties in concrete with RAP aggregates would be improved by increasing the cohesive strength of the asphalt coating thus driving the failure mode to an asphalt-cement adhesive and decreasing the ITZ porosity. Reference [6] studied the use of fractionated reclaimed asphalt pavement (FRAP) as a partial replacement (0%, 20%, 35%, and 50%) of coarse aggregate in a ternary blend concrete containing cement, slag, and fly ash. The increase in the percentage of FRAP in concrete resulted in a decrease in the compressive, split tensile, and flexural strength. The elastic and dynamic moduli also decreased with increasing FRAP content. The results of the study indicated that up to 35% FRAP can be replaced as coarse aggregates while still meeting the sufficient fresh, strength, and durability



specifications of conventional concrete. Dirty FRAP without washing was found to meet the IDOT compressive strength requirements up to 50% replacement. Reference [7] studied on the potential of blasted copper slag as fine aggregate in Portland cement concrete. The greatest reductions of compressive strength were found when the replacement was over 40%.

Reference [8] conducted studies on soft and hard bitumen from unaged, aged recycled asphalt concrete mixtures for rheological, thermal, microstructural aspects. Bitumen with 50% weight of virgin bitumen and 50% from recycled asphalt pavements were studied. Aging and recycling changed rheological properties of soft bitumen by increasing complex modulus and decreasing phase angle. Recycled asphalt pavement bitumen has an adverse effect on adhesion properties. Reference [9] conducted an experimental study of concrete made with granite and iron powders as partial replacement of sand. The test resulted showed that for 10% ratio of granite powder in concrete, the increase in compressive strength was about 30% compared to normal concrete. Similar results were obtained for flexure. For replacement, up to 20% of sand by weight with iron powder in concrete resulted in an increase in compressive and flexural strength.

Reference [10] conducted studies on experiments with control concrete with natural sand and gravel, concrete with reclaimed coarse and reclaimed fine aggregate, concrete with reclaimed coarse and natural sand, and concrete mix with reclaimed coarse and natural sand where 30% OPC replaced with flash. Concrete made with reclaimed coarse asphalt aggregates and sand showed less reduction in strength compared to others. Reference [11] studied on RAP aggregate materials treated with different dosages of portland type I/II cement and with alkali-resistant glass fibers. Reference [12] investigated on portland cement concrete containing recycled asphalt aggregate. Soft asphalt binder induces stress concentration and microcracking in concrete matrix causing a reduction in strength. Concrete made with only coarse RAP showed the least reduction in strength and a significant increase in toughness. Compared with rubber, RAP had a better chance of replacement in concrete. Reference [13] studied the durability of copper slag contained concrete exposed to sulfate attack. Replacement of cement with copper slag up to 15% led to more than 50% decrease in sulfate expansion. Reference [14] experimentally investigated the feasibility of granite powder waste as a possible replacement in manufacturing concrete. At 0.5 water to cement ratio, experiments were done for 10, 25, 40, 55 and 70% sand replacement by granite powder. Compressive strength results for 7, 28, and 56 days were highest at 25% replacement and lowest at 70% replacement.

Reference [15] studied the effect of incorporating Dirty RAP (DRAP) Washed RAP (WRAP), and Abrasion and Attrition (AB&AT) treated RAP on the fresh, mechanical and durability properties of concrete and compared with each other as well as normal aggregate concrete. Beneficiation of RAP by AB&AT method increased the compressive strength of concrete by 9.74% and 12.21% and flexural strength by 6.05% and 8.55% as compared to WRAP and DRAP inclusive concrete. ABTRAP aggregates were found to possess both the desirable properties of RAP as well as natural aggregates. Aggregates processed with both washing and AB&AT method resulted in better workability than natural aggregate concrete. Reference [16] studied on improving the properties of ABTRAP (Beneficiated RAP aggregates by Abrasion & Attrition technique) inclusive concrete by incorporating mineral admixtures such as Silica Fume (SF), Fly ash (FA) and Sugarcane Bagasse Ash (SCBA). 6 mixes were prepared by partially replacing Ordinary Portland Cement (OPC) by SF (5% & 10%), FA (10% & 20%) and SCBA (5% & 10%). Maximum improvement in compressive, flexural and split tensile strength of ABTRAPC mix was found when 10% OPC was partially replaced by SF followed by 20% replacement by FA and 5% replacement by SCBA.

Reference [17] found out that replacement of 10% cement by BGA was found to increase the compressive strength by 15%, modulus of rupture by 12%, and splitting strength by 13% compared to concrete containing 100% RAP aggregates. Shi et al. [18] investigated the viability of partial replacement of virgin coarse aggregate by coarse RAP to formulate PCC paving mixtures. Replacing virgin coarse aggregate by RAP in a typical PCC pavement mix has caused a reduction in strength and modulus of elasticity. The coarse RAP with sufficient intermediate size particles can help to make dense graded RAP-PCC mixtures which can show better workability and

mechanical properties compared to other gap-graded RAP-PCC mixtures. Reference [19] studied the strength and durability properties of concrete made with granite industry waste. The obtained test results were indicated that the replacement of natural sand by GP waste up to 15% of any formulation is favorable for the concrete making without adversely affecting the strength and durability criteria.

Reference [21] investigated the effect of using alternatives for both fine and coarse aggregates with copper slag (30%, 40% and 50%), iron slag (30%, 40% and 50%) and recycled concrete aggregate (20%, 25% and 30%) with various proportions of mix by the partial replacement of sand and gravel respectively. From the study, it has been concluded that 40% of copper slag, 40% iron slag and 25% of recycled concrete aggregate possess more strength than a conventional concrete mix. Reference [22-23] studied the interactions between granites and asphalts based on theology. Different granite powders and asphalt showed significant differences in their interactions and this compatibility problem between asphalt and granite should be considered during the choice of materials.

### **3.0 Research Significance**

Granite powder and copper slag are industrial by-products obtained from the granite cutting and copper manufacturing industries. These can be used as partial replacement of sand in concrete. RAP aggregates are obtained during the reconstruction or resurfacing of pavements. These aggregates, when used as coarse aggregate in concrete, have shown to decrease the mechanical properties of concrete. The modification of RAP coarse aggregates by abrasion and attrition and the partial replacement of sand in the concrete by granite powder or copper slag is an interesting area of research. The use of RAP aggregates, granite powder and copper slag in concrete will reduce the consumption of natural resources in the construction process. The health hazards and the effects on the ecosystem will also be reduced by the recycling of these byproducts.

### **4.0 Experimental Investigation**

The experimental investigation comprised of preparing specimens of normal concrete, concrete with RAP aggregate replaced as coarse aggregate at 100%, concrete with RAP aggregate replaced as coarse aggregate at 30%, concrete with RAP aggregate replaced as coarse aggregate at 30% after abrasion, and abrasion treated RAP concrete with granite powder or copper slag replacement. The specimens comprised of concrete cubes, beams, and cylinders for testing the compressive strength, flexural strength and split tensile strength respectively. The concrete mix consists of Portland Pozzolana Cement, coarse aggregates, RAP aggregates, m-sand, granite powder or copper slag, superplasticizer and water.

#### **4.1. Materials**

The materials used for the study included Portland Pozzolana Cement coarse aggregates (gravel) RAP aggregates, fine aggregates (m-sand), granite powder, copper slag, superplasticizer, and water. Portland Pozzolana Cement (PPC) conforming to (IS 1489 part1) fly ash based is used for the experimental work. The specific gravity of cement is 2.89 found using le chatelier flask method as per IS 2720 part3. Reclaimed Asphalt Pavement aggregates and natural aggregates are used as coarse aggregates in this experiment. Reclaimed Asphalt Pavement Aggregates were collected from the highway works in Calicut. Dirty Reclaimed Asphalt Pavement Aggregates were used for the work without washing. Natural coarse aggregates of size passing through 20 mm sieve and retained on 12.5 mm sieve are taken. Reclaimed Asphalt Pavement aggregates of size passing through 20 mm sieve and retained on 12.5 mm sieve are taken. The specific gravity of coarse aggregates and RAP aggregates are 2.66 and 2.35 respectively. M-Sand, granite powder and copper slag are used as fine aggregates. Granite powder is collected from Cemal Gems & Minerals,

Bangalore. Copper slag is collected from Blastine private Limited, Koratty, Kerala. Chemical composition analysis results for granite powder and copper slag were obtained from their suppliers i.e. Cemal Gems & Minerals and Blastine private limited respectively. The chemical composition of granite powder and copper slag are given in Table 1 and Table 2 respectively. Specific gravities of m-sand, granite powder, and copper slag are 2.6, 2.5 and 3.2 respectively found out using a pycnometer test as per IS-2386 part-3. Fineness modulus of m-sand, granite powder, and copper slag are 3.44, 2.64 and 3.43 respectively. Sieve analysis test was conducted according to IS 2386 part-1. Gradation curves for fine aggregates are shown in Fig.1. High range water reducing super plasticizer Glenium B233 of specific gravity 1.09 is used for the experiment.

**Table 1:** Chemical composition of granite powder

Particulars	Values
SiO <sub>2</sub>	72.04%
Al <sub>2</sub> O <sub>3</sub>	14.42%
K <sub>2</sub> O	4.12%
Na <sub>2</sub> O	3.69%
CaO	1.82%
FeO	1.68%
Fe <sub>2</sub> O <sub>3</sub>	1.22%
MgO	0.71%
TiO <sub>2</sub>	0.3%
P <sub>2</sub> O <sub>5</sub>	0.12%
MnO	0.05%

Source: Batch Inspection Certificate, Cemal Gems, and Minerals, Bangalore

**Table 2:** Chemical composition of copper slag

Constituent	Percentage weight
Silica, SiO <sub>2</sub>	26- 30 %
Free Silica	< 5%
Alumina, Al <sub>2</sub> O <sub>3</sub>	2%
Iron Oxide, FeO	42-47%
Calcium Oxide, CaO	1-2 %
Magnesium Oxide, MgO	1.04 %
Copper Oxide, CuO	6.1 % max
Sulfates	0.13 %

Source: Batch Inspection Certificate, Blastline Pvt.Ltd

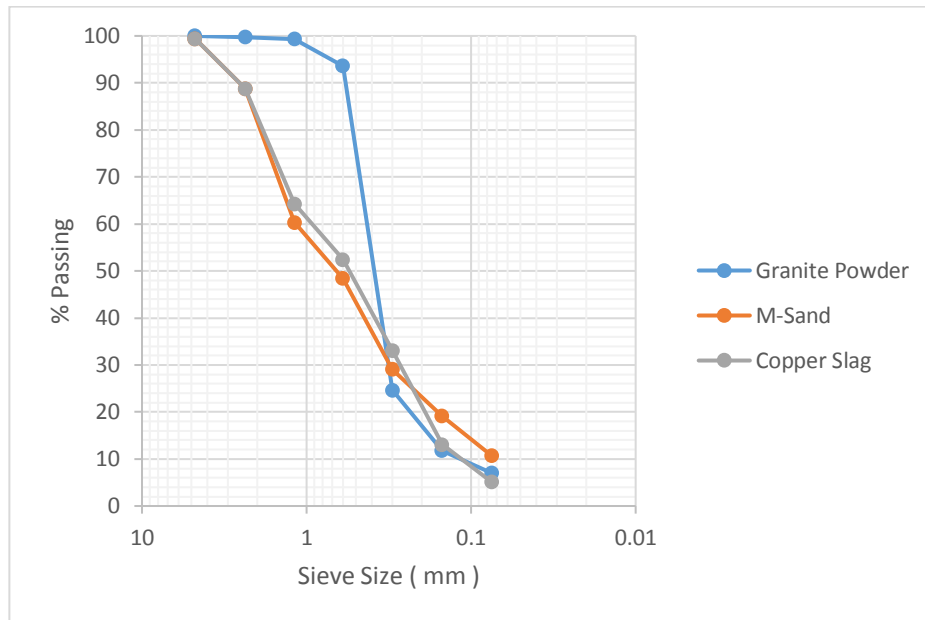


Figure 1: Particle size distribution curves of fine aggregates

#### 4.2 Mix Design of Concrete

Concrete mixtures were prepared with recycled asphalt pavement aggregates as coarse aggregates and granite powder or copper slag as partial replacement of fine aggregate at various percentages i.e. 0% (for the control mix), 5%, 10%, 15%, 20%, and 25%. The control mixture was designed to have a target 28 day compressive strength of 30 N/mm<sup>2</sup> (M-30). The mix design obtained is 1:0.43:2.13:2.89 as per IS 10262-2009. Slump test was conducted at admixture dosages of 0.4, 0.45 and 0.5% by mass of cementitious material. As better slump value and mix was obtained at 0.4% dosage, admixture dosage is fixed as 0.4% by mass of cementitious material for all mixes except for the abrasion treated RAP aggregate concrete mix with granite powder replaced as fine aggregate at 20 and 25% in which the dosage is increased to 0.42 and 0.43% by mass of cementitious material.

#### 4.3 Reference Specimens and Abrasion Process

Reference specimens like Normal Aggregate Concrete (NAC), concrete with RAP aggregate replaced as coarse aggregate at 100% (RAPC), concrete with RAP aggregate replaced as coarse aggregate at 30% (R-APC) and concrete with RAP aggregate replaced as coarse aggregate at 30% after abrasion (ABTRAPC) were cast. Los Angeles abrasion test was conducted according to IS 2386 part-4.

The principle of Los Angeles abrasion test is to produce abrasive action by use of standard steel balls which when mixed with aggregates and rotated in a drum for a specific number of revolutions also cause an impact on aggregates. In the modification process, Los Angeles Abrasion Testing Machine is used to do the abrasion process. The machine consists of a hollow cylinder, mounted on a steady frame on ball bearings. It has a detachable shelf which extends throughout the inside length of the drum. The drum is rotated at a speed of 30-33 rpm by an electric motor through a heavy reduction gear. Abrasive charge i.e., cast iron or steel balls, approximately 48mm in diameter and each weighing between 390 to 445 g of twelve numbers are used. Optimum duration time for the abrasion process is fixed at 10 minutes as longer duration resulted in fractured aggregates which might cause a loss in load transfer efficiency. As a number of abrasive charge increases, reduction in asphalt content also increases. Therefore 10 steel balls were selected for the abrasion process. Input quantity of Reclaimed Asphalt Pavement (RAP) Aggregates in the machine

was selected based on the materials passing 4.75 mm sieve after the abrasion process as per Table 3. When the number of aggregates was 30 kg, maximum attrition took place and hence the input quantities of aggregates were fixed as 30 kg. Bitumen content was found to reduce about 40.4% by centrifugal extraction method.

**Table 3:** Percentage passing through 4.75 mm sieve

RAP ( kg )	15	20	25	30	35
Passing 4.75 mm Sieve ( % )	4.02	5.15	6.2	6.63	6.38

#### **4.4. Preparation of Test Specimens with Granite Powder and copper slag**

Granite powder and m-sand were mixed thoroughly. Natural coarse aggregate and RAP aggregates modified by abrasion were mixed thoroughly and added to the mix. Once all materials were mixed thoroughly, superplasticizer was added to water and this water is added to the concrete mix. Hand mixing was done thoroughly. Specimens like 150X150X150 mm cubes, 100X100X500 mm beams, 150 mm X 300 mm cylinders were prepared using the concrete mix. After pouring into molds compaction of 25 blows was done using compaction rod in three layers. After finishing the surface, molds are dried for 24 hrs. After the removal from molds, the specimens are cured in an open water tank for a period of 28 days. The percentages of granite powder used were 5%, 10%, 15%, 20% and 25 of sand by weight designated by GP05, GP10, GP15, GP20, and GP25 respectively. Preparation of concrete specimens with copper slag was similar to those of granite powder specimens. The percentages of copper slag used were 5%, 10%, 15%, 20% and 25 of sand by weight designated by CS05, CS10, CS15, CS20 and CS25 respectively.

#### **5.0 Testing of Fresh and Hardened Properties in Concrete**

Slump test is done to check the workability of freshly made concrete. Concrete cubes, beams, and cylinders were used for testing the compression tests, flexural tests and split tensile strength tests into cubes, beams, and cylinders respectively. Compressive strength test, Flexural strength test and split tensile strength test were done according to IS 516-1959 at the 7<sup>th</sup> and 28<sup>th</sup> day. 24 cubes, 16 beams, and 16 cylinders were prepared as the reference specimens. Thirty cubes, twenty cylinders, and twenty beams were prepared each for granite powder and copper slag concrete mix in total. Slump variations for concrete mixes are given in Fig.2.

#### **6.0 Slump Test Results**

Reclaimed Asphalt Pavement Aggregate Concrete mixes were more workable compared to normal concrete mixes and are high due to its small particle size and larger fineness. These mixes were less workable at higher percentage replacements, especially above 15%. Concrete mixes with copper slag were highly workable and the problem of bleeding occurred at replacements above 15%.

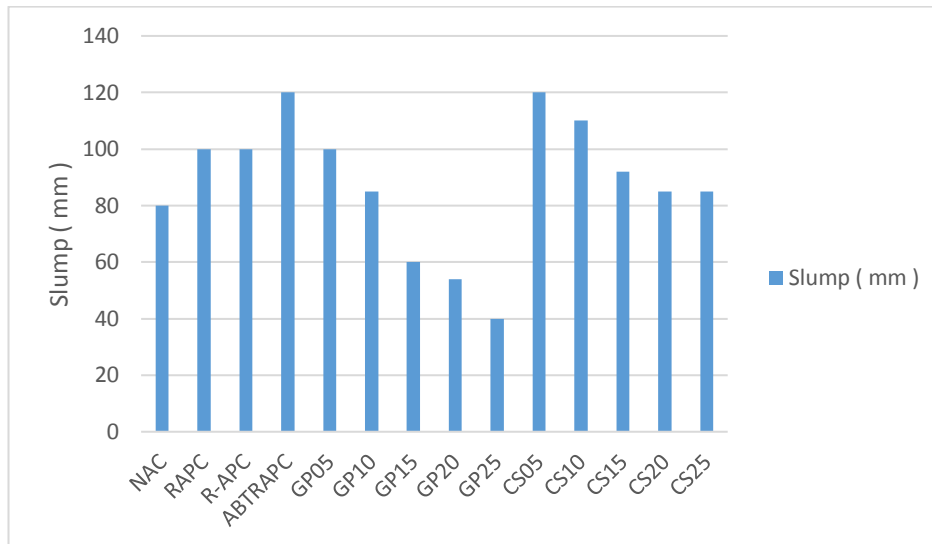


Figure 2: Slump variations for concrete mixes

## 7.0 Hardened Concrete Test Results

Strength tests were performed at the 7<sup>th</sup> and 28<sup>th</sup> day. Hardened concrete test results were obtained as an average of three specimens for each mix. A Compressive strength of 37.55 N/mm<sup>2</sup> is obtained for the NAC at 28 days. RAPC showed a reduction in strength of 62.13% (14.22 N/mm<sup>2</sup>) compared to NAC. R-APC showed a reduction in strength of 34.32% (24.66 N/mm<sup>2</sup>) compared to NAC. ABTRAPC showed a reduction in strength of 33.44% (24.99 N/mm<sup>2</sup>) compared to NAC and it exhibits the least reduction in strength. Fig.3 and Fig.4 show the compressive strength of cubes with different proportions of ( GP ) and ( CS ) respectively. A Flexural strength of 7.62 N/mm<sup>2</sup> is obtained for the NAC at 28 days. RAPC showed a reduction in strength of 40.94% (4.5 N/mm<sup>2</sup>) compared to NAC. R-APC showed a reduction in strength of 32.15% (5.17 N/mm<sup>2</sup>) compared to NAC. ABTRAPC showed a reduction in strength of 11.41% (6.75 N/mm<sup>2</sup>) compared to NAC and it exhibits the least reduction in strength. A split tensile strength of 2.63 N/mm<sup>2</sup> is obtained for the NAC at 28 days. RAPC showed a reduction in strength of 61.21% (1.02 N/mm<sup>2</sup>) compared to NAC. R-APC showed a reduction in strength of 28.89% (1.87 N/mm<sup>2</sup>) compared to NAC. ABTRAPC showed a reduction in strength of 24.33% (1.99 N/mm<sup>2</sup>) compared to NAC and it exhibits the least reduction in strength. Split tensile strength of ABTRAPC mixes (1.99 MPa) were 6.41% greater than R-APC mixes. Strength values of reference specimens are given in Table 4. Strength values of specimens with granite powder and copper slag are given in Table 5 and Table 6 respectively.

Table 4: Strength values of reference specimens

MIX	Average Compressive Strength (N/mm <sup>2</sup> )		Average Flexural Strength (N/mm <sup>2</sup> )		Average Tensile Strength (N/mm <sup>2</sup> )	
	7 days	28 days	7 days	28 days	7 days	28 days
NAC	24.22	37.55	5	7.62	2.13	2.63
RAPC	6.505	14.22	0.17	4.5	0.78	1.02
R-APC	18.75	24.66	5.12	5.17	1.52	1.87
ABTRAPC	20.10	24.99	6	6.75	1.71	1.99

**Table 5:** Strength values of specimens with granite powder

MIX	Average Compressive Strength (N/mm <sup>2</sup> )		Average Flexural Strength (N/mm <sup>2</sup> )		Average Tensile Strength (N/mm <sup>2</sup> )	
	7 days	28 days	7 days	28 days	7 days	28 days
<b>GP05</b>	14.99	18.55	3.87	4.75	1.83	1.96
<b>GP10</b>	17.22	19.66	4.55	4.92	1.93	1.98
<b>GP15</b>	23.12	30.99	5.87	6.12	1.96	1.99
<b>GP20</b>	19.56	25.37	4.55	6	1.8	2.08
<b>GP25</b>	14.48	17.82	3.77	4.25	1.2	1.37

**Table 6:** Strength values of specimens with copper slag

MIX	Average Compressive Strength (N/mm <sup>2</sup> )		Average Flexural Strength (N/mm <sup>2</sup> )		Average Tensile Strength (N/mm <sup>2</sup> )	
	7 days	28 days	7 days	28 days	7 days	28 days
CS05	16.37	30.77	4.62	6.37	1.95	2.41
CS10	22.21	31.84	5.00	6.67	1.94	2.46
CS15	23.19	32.46	5.05	7.62	1.99	2.67
CS20	20.26	24.31	5.00	6.87	1.95	2.59
CS25	17.45	22.71	4.87	6.8	1.92	2.38

A maximum strength of 30.99 MPa is achieved by granite powder mixes at 15 % replacements at 28<sup>th</sup> day and it is equal to an increase of 24% compared to ABTRAPC mix. At 20% replacement it showed an increase of 1.52 % compared to ABTRAPC and at 25% replacement, strength decreased to 17.82 MPa.

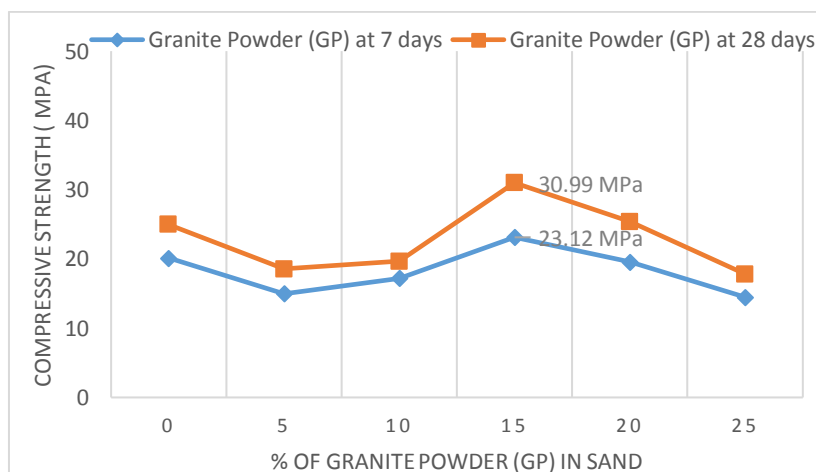


**Figure 3:** Compressive strength of cubes with different proportions of (GP)

Copper slag at 5% replacement itself shows an increase of 23.12% (30.77 MPa) compared to ABTRAPC mix. A maximum strength of 32.46 MPa is achieved by copper slag mixes at 15 % replacements at 28<sup>th</sup> day and it is equal to an increase of 29.89% compared to ABTRAPC mix. At 20% strength decreases to 24.31 MPa and decreases further.

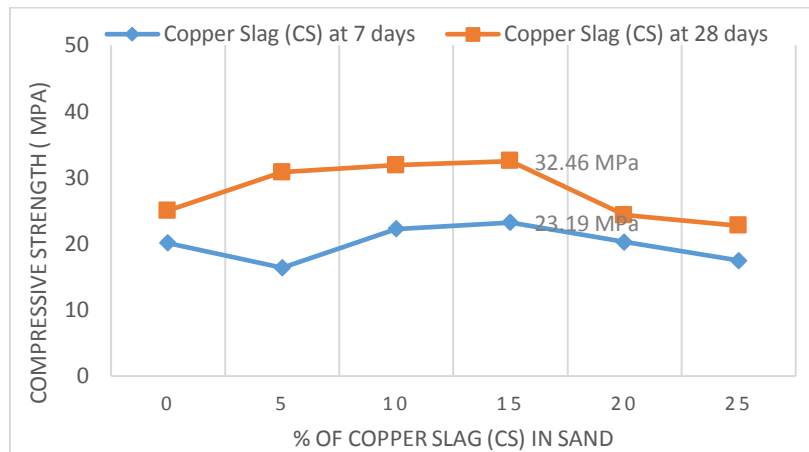


**Figure 4:** Compressive strength of cubes with different proportions of (CS)

Fig.5 and Fig.6 shows the flexural strength of beams with different proportions of (GP) and (CS) respectively.

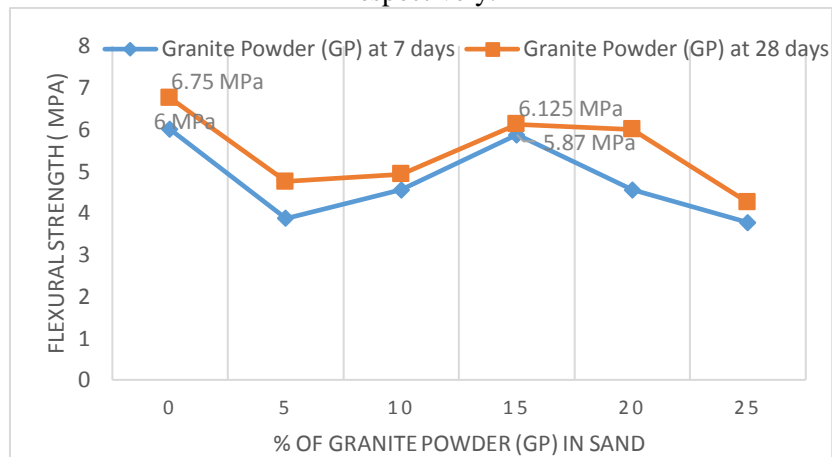


**Figure 5:** Flexural strength of a beam with different proportions of (GP)

Abrasion process increased the bending strength (5.17MPa) by 30.5% comparing to non-abrasion treated aggregates (6.75 MPa) at 28 days. At 15% replacement of fine aggregate with granite powder, a flexural strength of 6.12 MPa is obtained which shows a reduction of 9.3% compared to abrasion treated RAP aggregates (6.75 MPa) at 28 days. At 15% replacement of fine aggregate with copper slag, a flexural strength of 7.62 MPa is obtained which is similar to that of normal concrete and about 12.8% greater compared to ABTRAP concrete mix at 28 days. All mixes with copper slag exhibited greater flexural strength than granite powder mixes and all other reference mixes.



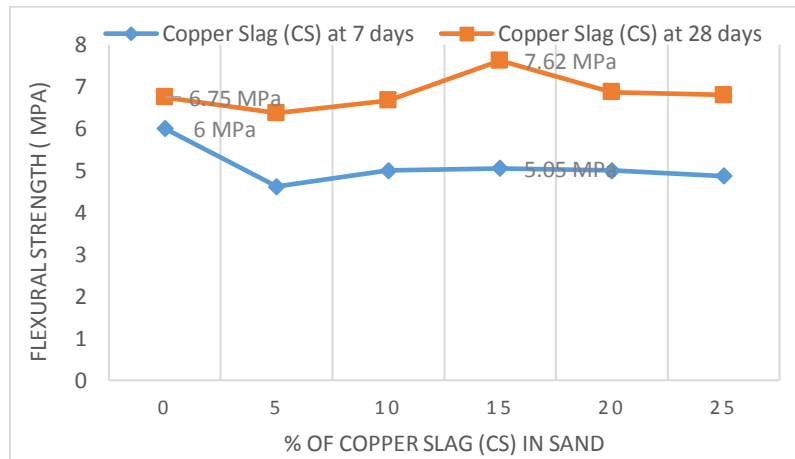


**Figure 6:** Flexural strength of a beam with different proportions of ( CS )

Split tensile strength increased with an increase in the percentage of granite powder replacements up to 20% with a maximum of 2.08 MPa at 20% replacement and decrease further. A maximum split tensile strength of 2.67 MPa is obtained at 15% replacement of fine aggregate with copper slag which shows an increase of 1.52% compared to normal concrete and 34.17% compared to ABTRAP mixes. Fig.7 and Fig.8 shows the split tensile strength of cylinders with different proportions of (GP) and (CS) respectively.

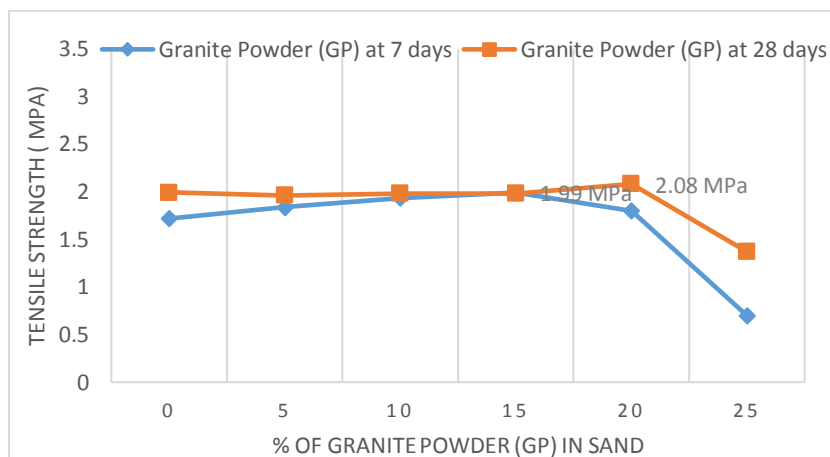


**Figure 7:** Split tensile strength of cylinders with different proportions of (GP)

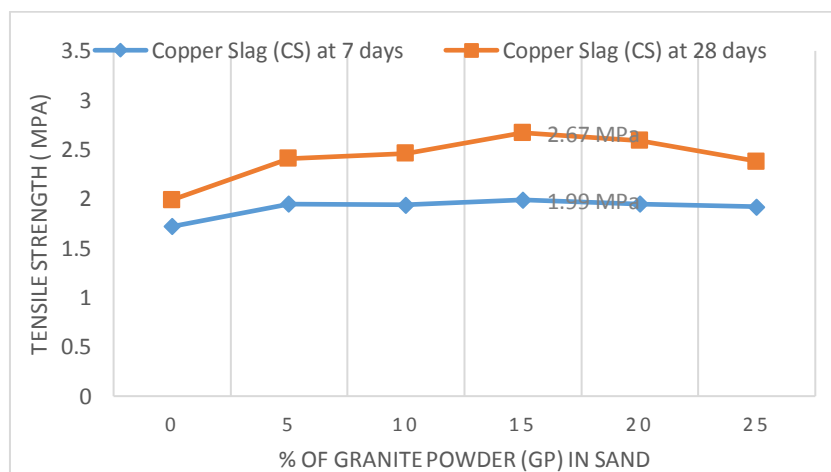
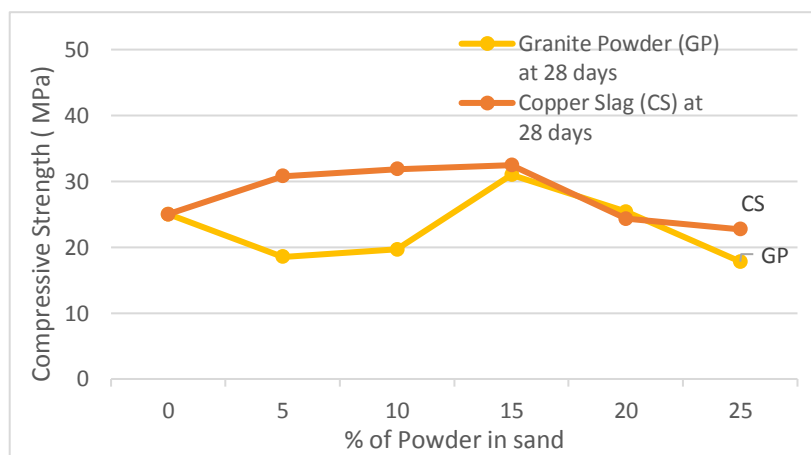


**Figure 8:** Split tensile strength of cylinders with different proportions of (CS)

## 8.0 Comparison of Test Results

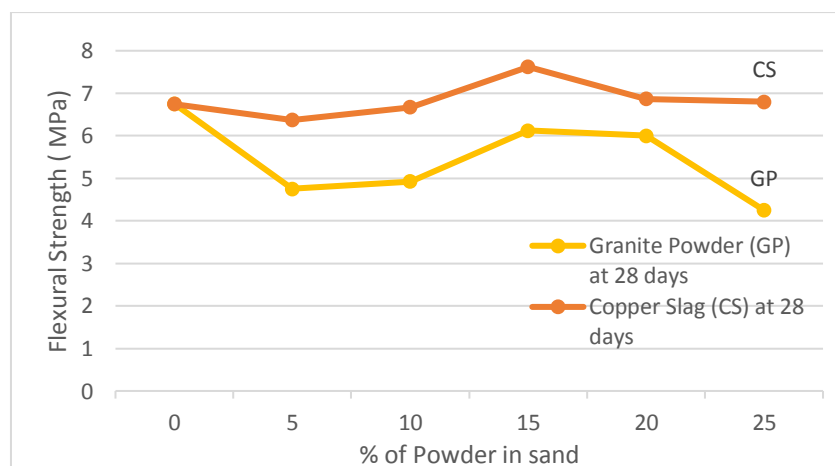
Compressive strength increased with an increase in the percentage of replacement of granite powder up to 15% compared to ABTRAPC and increase in this case was 24%. Maximum flexural strength was obtained at 15% replacement even though it exhibited a reduction of 9.3% compared to ABTRAPC. Maximum split tensile strength is obtained at 20% and the increase was 4.52% compared to ABTRAPC. Compressive strength increased with an increase in the percentage of replacement of copper slag up to 15% and there was an increase of 29.89% compared to ABTRAPC. Maximum flexural strength was obtained at 15% replacement similar to normal concrete and 12.8% compared to ABTRAPC. Maximum split tensile strength is obtained at 15% and the increase was 1.52% compared to normal aggregate concrete and 34.17% compared to ABTRAPC. Replacements at 25% showed the least water absorption and more resistance to acid attack.

Fig.9 shows a comparison of compressive strength of concrete with granite powder and copper slag. Comparing the results of GP and CS, it is observed that up to 15% replacements, CS exhibited a higher compressive strength. At 20%, the compressive strength of GP increases and at 25% maximum strength was exhibited by CS.



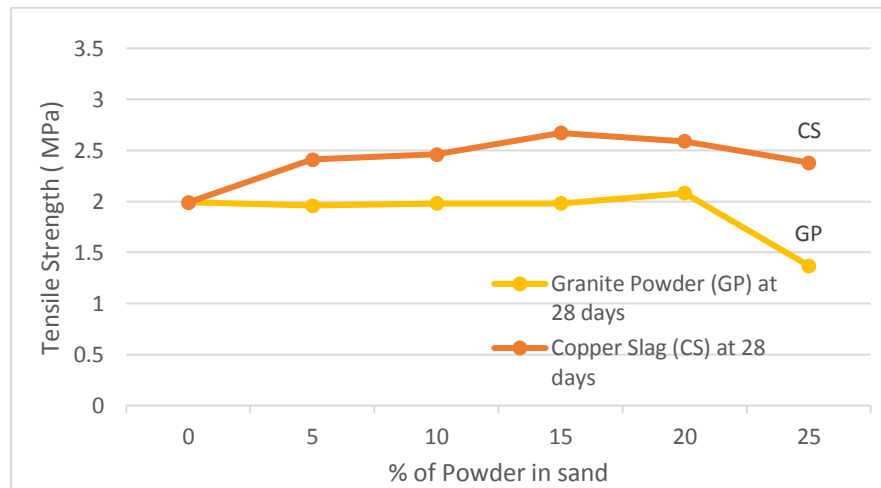
**Figure 9:** Effect of % of (GP) and (CS) on the Compressive Strength of Concrete

Fig.10 shows a comparison of flexural strength of concrete with granite powder and copper slag. Comparing the results of GP and CS, it is observed that at all replacements, CS exhibited a higher flexural strength comparing to GP.



**Figure 10:** Effect of % of (GP) and (CS) on the Flexural Strength of Concrete

Fig.11 shows a comparison of the split tensile strength of concrete with granite powder and copper slag. Comparing the results of GP and CS, it is observed that at all replacements, CS exhibited a higher split tensile strength comparing to GP.



**Figure 11:** Effect of % of (GP) and (CS) on the Tensile Strength of Concrete

## 9.0 Conclusions

Based on the test results, the following conclusions can be made.

1. Abrasion and attrition improved the workability, mechanical and durability properties in concrete than the concrete with reclaimed pavement aggregates without abrasion since now the aggregate surface is more available to bonding with mortar and aggregates.
2. Workability of concrete mixes with granite powder and copper slag were good up to 15% of replacement. High water absorption of granite powder caused poor compactness and porosity and low water absorption property of copper slag caused bleeding above the replacement rates.
3. M30 grade concrete mix was developed by using reclaimed asphalt pavement aggregates as a partial replacement of coarse aggregate and granite powder as a fine aggregate at 15% and copper slag as a fine aggregate at 5, 10 and 15%.
4. Granite powder replaced at 15% showed a compressive strength of 23.12 MPa at 7th day and a maximum strength of 30.99 MPa at 28th day. Compressive strength gain of 34.03% was attained in the 28th day. Strength at 15% replacement is about 24% greater than the ABTRAPC specimens and strength at 20% replacement is 1.52% greater than the ABTRAPC specimens. Granite powder specimens developed strength ranging from 18.55MPa, 19.66 MPa, 30.99 MPa, 25.37 MPa, and 17.82 MPa at 5, 10, 15, 20 and 25 % replacements respectively.
5. Copper slag replaced at 5% itself showed a compressive strength similar to that attained by granite powder at 15% and it is 23.12% greater than ABTRAPC. Copper slag replaced at 15% showed a maximum strength 29.89% greater than ABTRAPC of 23.12 MPa at 7th day and a maximum strength of 30.99 MPa at 28th day. Compressive strength gain of 34.03% was attained in the 28th day. Strength at 15% replacement is about 24% greater than the ABTRAPC specimens and strength at 20% replacement is 1.52% greater than the ABTRAPC specimens. Copper slag specimens developed strength ranging from 30.77MPa, 31.84 MPa, 32.46 MPa, 24.3 MPa, and 22.7 MPa at 5, 10, 15, 20 and 25 % replacements respectively.
6. At 15% replacement of fine aggregate with granite powder, a flexural strength of 6.12 MPa is obtained which shows a reduction of 9.3% compared to abrasion treated RAP aggregates (6.75 MPa) at 28 days.
7. At 15% replacement of fine aggregate with copper slag, a flexural strength of 7.62 MPa is obtained which is similar to that of normal concrete and about 12.8% greater compared to

ABTRAP concrete mix at 28 days. All mixes with copper slag exhibited greater flexural strength than granite powder mixes and all other reference mixes.

8. Split tensile strength increased with an increase in the percentage of granite powder replacements up to 20% with a maximum of 2.08 MPa at 20% replacement which is 4.52% greater than ABTRAPC and decrease further. A maximum split tensile strength of 2.67 MPa is obtained at 15% replacement of fine aggregate with copper slag which shows an increase of 1.52% compared to normal concrete and 34.17% compared to ABTRAP mixes.

### **Conflict of Interest Statement**

On behalf of all authors, the corresponding author states that there is no conflict of interest.

### **References**

- [1] S. Abraham and G. Ransinchung, "Strength and permeation characteristics of cement mortar with Reclaimed Asphalt Pavement Aggregates", *Construction and Building Materials*, vol. 167, pp. 700-706, 2018.
- [2] K. Al-Jabri, A. Al-Saidy, and R. Taha, "Effect of copper slag as a fine aggregate on the properties of cement mortars and concrete", *Construction and Building Materials*, vol. 25, no. 2, pp. 933-938, 2011.
- [3] R. Al-Mufti and A. Fried, "Improving the strength properties of recycled asphalt aggregate concrete", *Construction and Building Materials*, vol. 149, pp. 45-52, 2017.
- [4] Brand and J. Roesler, "Bonding in cementitious materials with asphalt-coated particles: Part I – The interfacial transition zone", *Construction and Building Materials*, vol. 130, pp. 171-181, 2017.
- [5] A. Brand and J. Roesler, "Bonding in cementitious materials with asphalt-coated particles: Part II – Cement-asphalt chemical interactions", *Construction and Building Materials*, vol. 130, pp. 182-192, 2017.
- [6] Brand, A, fractionated reclaimed asphalt pavement as a coarse aggregate replacement in a ternary blended concrete pavement, Report ICT-12-008, Illinois State Toll Highway Authority, Downers Grove, 2012.
- [7] Dos Anjos, M. A. G., Sales, A. T. C., and Andrade, N. "Blasted Copper Slag as Fine Aggregate in Portland Cement Concrete", *Journal of environmental management*, vol. 96, 607-613, 2017.
- [8] Dos Santos, S., Party, M. N., and Poulikakos, L. D. "From Virgin to Recycled Bitumen: A Microstructural View", *Composites Part B: Engineering*, vol. 80, pp. 177-185, 2015.
- [9] Ghannam, S., Najm, H., and Vasconez, R. "Experimental Study of Concrete made with Granite and Iron Powders as Partial Replacement of Sand", *Sustainable Materials and Technologies*, vol. 9, pp. 1-9, 2016.
- [10] Hassan, K. E., Brooks, J. J., and Erdman, M. "The Use of Reclaimed Asphalt Pavement (RAP) Aggregates in Concrete", *Waste management series*, (Vol. 1, pp. 121-128), 2000.
- [11] M. S. Shahbaz, R. Z. R. M. Rasi, M. F. Bin Ahmad, and F. Rehman, "What is supply chain risk management? A review," *Adv. Sci. Lett.*, vol. 23, no. 9, pp. 9233–9238, 2017.
- [12] Hoyos, L. R., Puppala, A. J., and Ordonez, C. A. "Characterization of Cement-Fiber-Treated Reclaimed Asphalt Pavement Aggregates: Preliminary Investigation", *Journal of Materials in Civil Engineering*, vol. 23, pp. 977-989, 2017.
- [13] Huang, B., Shu, X., and Li, G. "Laboratory Investigation of Portland Cement Concrete Containing Recycled Asphalt Pavements", *Cement and Concrete Research*, vol. 35, pp. 2008-2013, 2005.
- [14] Najimi, M., Sobhani, J., and Pourkhorshidi, A. R. "Durability of Copper Slag Contained Concrete Exposed to Sulfate Attack", *Construction and Building materials*, vol. 25, pp. 1895-1905, 2011.

- [15] M. S. Shahbaz, R. Z. RM Rasi, M. F. Bin Ahmad, and S. Sohu, "The impact of supply chain collaboration on operational performance: Empirical evidence from manufacturing of Malaysia," *Int. J. Adv. Appl. Sci.*, vol. 5, no. 8, pp. 64–71, 2018.
- [16] Singh, S., Nande, N., Bansal, P., and Nagar, R. "Experimental Investigation of Sustainable Concrete Made with Granite Industry By-Product, *Journal of Materials in Civil Engineering*", vol. 29, 2017.
- [17] Singh, S., Ransinchung, G. D., and Kumar, P. "An Economical Processing Technique to Improve RAP Inclusive Concrete Properties", *Construction and Building Materials*, vol. 148, pp. 734-747, 2017.
- [18] Singh, S., Ransinchung, G. D., and Kumar, P. "Effect of Mineral Admixtures on Fresh, Mechanical and Durability Properties of RAP Inclusive Concrete", *Construction and Building Materials*, vol. 156, pp. 19-27, 2017.
- [19] Singh, S., Debbarma, S., and Kumar, P. "Utilization of Reclaimed Asphalt Pavement Aggregates Containing Waste from Sugarcane Mill for Production of Concrete Mixes", *Journal of Cleaner Production*, vol. 74, pp. 42-52, 2018.
- [20] Shi, X., Mukhopadhyay, A., and Liu, K. W. "Mix Design Formulation and Evaluation of Portland Cement Concrete Paving Mixtures Containing Reclaimed Asphalt Pavement", *Construction and Building Materials*, vol. 152, pp. 756-768, 2018.
- [21] Vijayalakshmi, M., and Sekar, A. S. S. "Strength and Durability Properties of Concrete made with Granite Industry Waste, *Construction, and Building Materials*", vol. 46, pp. 1-7, 2013.
- [22] Vijayaraghavan, J., Jude, A. B., and Thivya, J. "Effect of Copper Slag, Iron Slag, and Recycled Concrete Aggregate on the Mechanical Properties of Concrete", *Resources Policy*, vol. 53, pp. 2019-225, 2017.
- [23] Yi-qiu, T., Li, X., and Zhou, X. "Interactions of Granite and Asphalt based on the Rheological Characteristics", *Journal of Materials in Civil Engineering*, vol. 22, pp. 820-825, 2013.